Non-Coherent Direction of Arrival Estimation and Localization Based on Sensor Arrays

The University Of Sheffield.

Zhengyu Wan

Department of Electronic and Electrical Engineering

University of Sheffield

This dissertation is submitted for the degree of

Doctor of Philosophy

January 2023

Acknowledgements

I would like to acknowledge my sincerest gratitude and appreciation to my supervisors Dr. Wei Liu and Dr. Xiaoli Chu. Thank you for your guidance and invaluable advice. To my parents, thank you for your unlimited support in all aspects.

Especially, I would like to thank my wife, Mrs Manli Le, for her encouragement and companion throughout the entire period.

To all colleagues in the C34, thank you for the advice these years.

Abstract

Direction of arrival (DOA) estimation is an important research area in array signal processing. Existing works normally assume the phase information obtained at sensors of the array are accurate and therefore their performance degrades when the phase information is not reliable. For such a scenario, a new class of non-coherent DOA estimation methods has been proposed, where only magnitude information at an array of sensors is required. However, the phase retrieval based methods always require one or more reference signals to resolve ambiguity issues and fail to exploit the multi-snapshot information effectively. In this thesis, to efficiently and effectively exploit multiple snapshots usually available at an array, a fasT grOup sparsitY Based phAse Retreival (ToyBar) algorithm is proposed to solve the non-coherent DOA estimation problem. To avoid the use of reference signals, an effective array structure based on two uniform linear sub-arrays is proposed first for non-coherent DOA estimation. Unambiguous DOA can be found either by exploiting the non-linear property of sinusoidal function with the aid of the extra measurements provided by the second array, or applying the ToyBar algorithm to the whole array directly. Instead of using ULAs, uniform circular arrays (UCAs) can also be employed to overcome the ambiguities arising in non-coherent measurements. In addition, an off-grid model involved with a bias vector is proposed and a two-step method based on this model is further developed. Moreover, a two-dimensional localization method with an off-grid signal model is proposed for the non-coherent source localization problem based on distributed sensor arrays, where each platform employs a UCA. Finally, the non-coherent method has been extended to wideband signals, where the signal model is formulated with convolutional sparse coding (CSC) in the time domain directly.

Table of contents

List of Publications viii

List of figures x

List of tables xiii

List of Abbreviations xiv

1 Introduction 1

1.1 Introduction 1

1.2 Original Contributions 3

1.3 Thesis Outline 4

2 Review of DOA Estimation 7

2.1 Introduction to Antenna Arrays 7

2.2 Narrowband DOA estimation 8

2.2.1 Signal Model 8

2.2.2 Beamforming based Methods 9

2.2.3 Subspace Based Methods 13

2.2.4 Compressive Sensing Based Methods 15

2.2.4.1 Grid refinement 18

2.2.5 Non-Coherent DOA Estimation 19

2.2.6 Inherent Ambiguities 22

2.3 Wideband DOA Estimation 23

2.3.1 Signal Model 23
2.3.2 Frequency based method 25
2.4 Simulations 27
2.5 Summary 30

3 A Fast Group Sparsity Based Phase Retrieval Algorithm for Non-Coherent DOA Estimation 31
3.1 Introduction 31
3.2 Non-Coherent Signal Model and Ambiguities 32
3.3 The Proposed Algorithm for Non-Coherent DOA Estimation 35
3.3.1 Convergence Analysis 38
3.3.2 Acceleration Scheme 39
3.3.3 Maximum Number of Resolvable Signals 40
3.4 Simulations 42
3.5 Conclusions 46

4 Non-Coherent DOA Estimation without Reference Signals by Different Array Structures 48
4.1 Introduction 48
4.2 The Dual-Array Structure 49
4.2.1 Signal Model 49
4.2.2 Non-coherent DOA Estimation with Dual Array 51
4.2.2.1 Separate Estimation Method 51
4.2.2.2 Joint Group Sparsity Based Method 54
4.2.3 Cramér-Rao Bound 56
4.2.4 Grid Refinement 59
4.2.5 Simulations 59
4.2.5.1 Separate Estimation method 60
4.2.5.2 Joint Group Sparsity Based Method 62
4.3 Non-Coherent DOA Estimation with UCA 68

4.3.1 Signal Model with UCA 68
4.3.2 Ambiguity 70
4.3.3 Simulations 71
4.4 Summary 73

5 Off-Grid Non-Coherent DOA Estimation and Source Localization of Narrowband Signals 74
5.1 Off-Grid DOA Estimation 75
5.1.1 The Developed Algorithm 75
5.1.2 Simulation Results 79
5.2 Localization with Distributed Sensor Arrays 82
5.2.1 Signal Model with Distributed Arrays 82
5.2.2 The Off-Grid Localisation Algorithm 84
5.2.3 Grid refinement 90
5.2.4 Cramér-Rao Bound 90
5.2.5 Simulation Results 93
5.3 Summary 98

6 Non-Coherent DOA Estimation of Wideband Signals 99
6.1 Wideband Signal Model in the Time Domain 100
6.2 Time Domain Based Wideband DOA Estimation 102
6.2.1 Coherent DOA Estimation of Wideband Signals 102
6.2.2 Cramér-Rao Bound 104
6.2.3 Non-Coherent DOA Estimation of Wideband Signal 106
6.3 Simulations 106
6.3.1 Coherent Wideband DOA Estimation 106
6.3.2 Non-Coherent Wideband DOA Estimation 111
6.4 Summary 115

7 Conclusion and Future Plan **117**

7.1 Conclusion 117

7.2 Future Work 119

References **120**

List of Publications

Journal papers

1. Z. Wan and W. Liu, "Time-domain wideband DOA estimation under the convolutional sparse coding framework," *IEEE Signal Processing Letters*, vol. 29, pp. 274-278, December 2022.

2. Z. Wan and W. Liu, "Non-coherent DOA estimation via proximal gradient based on a dual-array structure," *IEEE Access*, vol. 9, pp. 26792-26801, February 2021.

Conference papers

1. Z. Wan, W. Liu and P. Willett, “Non-coherent source localization with distributed sensor arrays,” in *Proc. IEEE Sensor Array and Multichannel Signal Processing Workshop (SAM)*, Trondheim, Norway, June 2022.

2. Z. Wan and W. Liu, “Non-coherent DOA estimation of off-grid signals with uniform circular arrays,” in *Proc. IEEE International Conference on Acoustics, Speech and Signal Processing (ICASSP)*, Toronto, ON, Canada, June 2021, pp. 4370-4374.

3. Z. Wan and W. Liu, “A fast group sparsity based phase retrieval algorithm for non-coherent DOA estimation,” in *Proc. Asilomar Conference on Signals, Systems, and Computers*, Pacific Grove, CA, USA, November 2020, pp. 220-224.

4. Z. Wan and W. Liu, "Non-coherent DOA estimation based on a dual-array structure without reference signals," in *Proc. International Workshop on Computational Advances in Multi-Sensor Adaptive Processing (CAMSAP)*, Le gosier, Guadeloupe, December 2019, pp. 46-50.

Under Review

1. Z. Wan, W. Liu and P. Willett, "Non-Coherent Source Localization of Off-Grid Signals with Distributed Sensor Array Networks," submited to *IEEE Transactions on Aerospace and Electronic Systems*.

List of figures

2.1 Structure of a linear array. 7
2.2 Summary of methods for narrowband DOA estimation. 10
2.3 Normalized spectrum of the Bartlett method, with 2 signals, 100 snapshots, 10 sensors, and SNR = 10 dB. 12
2.4 Normalized spectrum of the Capon method, with 2 signals, 100 snapshots, 10 sensors, and SNR = 10 dB. 12
2.5 Normalized spectrum of MUSIC, with 2 signals, 100 snapshots, 10 sensors, and SNR = 10 dB. 15
2.6 Normalized spectrum of the l_1-SVD method, with 2 signals, 100 snapshots, 10 sensors, and SNR = 10 dB. 19
2.7 Illustration of grid refinement. 20
2.8 Normalized spectrum of the GESPAR, with 1 signal, 5 snapshots, 20 sensors, and SNR = 15 dB. 24
2.9 Normalized spectrum of the GESPAR, with 2 signals, 5 snapshots, 20 sensors, and SNR = 15 dB. 24
2.10 Normalized spectrum of wideband signals, with 2 signals, 100 snapshots, 10 sensors, and SNR = 10 dB. 27
2.11 RMSE vs SNR. 28
2.12 RMSE vs phase error. 28
2.13 RMSE vs SNR of wideband sources. 29

3.1 Estimation results by the proposed ToyBar. 43

3.2 Estimation results by the modified GESPAR. 43
3.3 RMSE vs SNR. 45
3.4 RMSE vs number of snapshots. 45
3.5 RMSEvsK 46

4.1 The dual-array structure with a shared sensor. 50
4.2 RMSE result versus input SNR with different number of sensors. 61
4.3 RMSE result versus DOA separation with different number of sensors. . . . 61
4.4 Normalized spectrum of joint estimation method. 63
4.5 RMSE results versus SNR. 63
4.6 RMSE results versus sensor phase error. 64
4.7 Estimation results by the proposed ToyBar. 66
4.8 Estimation results by the modified GESPAR. 66
4.9 RMSEs versus different SNR. 67
4.10 RMSEs versus number of snapshots. 67
4.11 RMSE results versus $\check{\theta}$ for SNR=15dB. 68
4.12 A uniform circular array with M sensors and a inter-sensor spacing of d, where a signal impinges from θ. 69
4.13 Normalised spectrum. 72
4.14 Results by on-grid model. 72

5.1 Results by off-grid model. 80
5.2 Results by on-grid model. 80
5.3 RMSE versus SNR. 81
5.4 Source localization geometry. 83
5.5 Results by off-grid model. 95
5.6 Results by on-grid model. 95
5.7 RMSEs versus SNRs. 96
5.8 RMSEs versus sensor phase error. 97
5.9 RMSEs versus number of snapshots. 97

6.1 RMSE vs. SNR. 108
6.2 RMSE vs. snapshots. 108
6.3 The proposed method. 109
6.4 The traditional method. 109
6.5 RMSEs versus I. 111
6.6 Four incident signals with $M = 4$ sensors ULA. 112
6.7 Five incident signals with $M = 4$ sensors ULA. 112
6.8 Four incident signals with $M = 4$ sensors MRA. 113
6.9 Five incident signals with $M = 4$ sensors MRA. 113
6.10 Results with magnitude-only measurements. 114
6.11 Results with full measurements. 114
6.12 RMSEs versus SNR. 116
6.13 RMSE vs number of snapshots. 116

List of tables

3.1 Algorithm Summary (ToyBar) 40
3.2 Running times of different algorithms. 46

4.1 DOA estimation result by the separate estimation method 60
4.2 DOA estimation result by the separate estimation method 62
4.3 Running times versus number of snapshots. 65

5.1 Algorithm Summary (Two-Step Off-Grid) 79
5.2 Running times of off-grid and on-grid models. 81
5.3 Running time of different non-coherent methods. 96

6.1 Algorithm Summary (FISTA) 104
6.2 Running time of the proposed method and the traditional method. 110

List of Abbreviations

AOA	Angle of arrival
CSC	Convolutional sparse coding
DFT	Discrete Fourier transform
DGN	Damped Gaussian Newton
DOA	Direction of arrival
LASSO	Least absolute shrinkage and selection operator
MM	Majorizaion-minimization
MMV	Multiple measurement vector
ULA	Uniform circular array
ULA	Uniform linear array
Coherent	Array measurements contain both phase and magnitude.
Non-coherent	Array measurements contain magnitude-only measurements.
Off Grid	Source locations do not lie on the pre-defined grids
On Grid	Source locations lie on the pre-defined grids

Narrowband	The bandwidth of the impinging signals is narrow enough so that the delay between array sensors experienced by the signals can be approximated by simple phase shifts.
Wideband	The bandwidth of the impinging signals is wide enough so that the delay between array sensors experienced by the signals cannot be approximated by simple phase shifts.

Chapter 1

Introduction

1.1 Introduction

Antenna arrays have been studied extensively as it can be applied to various areas such as radar, sonar, radio astronomy, and communications [1–5]. Hydrophone arrays are applied underwater to localize deep-sea acoustic sources and track marine mammals [6, 7]; ultrasound arrays are employed in medical imaging, where the quality of images depends on the performance of the scanner beamformer [8, 9]; airgun arrays are applied for environmental studies such as marine seismic surveys and underwater acoustic propagation modeling [10]. Specifically, array signal processing involves manipulation of signals impinged on an array of sensors and it has three main research areas: beamforming, array signal detection, and direction of arrival (DOA) estimation. For beamforming it refers to steering nulls towards directions of interference signals and enhancing signal power from interested directions simultaneously, while array signal detection determines the presence and the number of impinging signals. DOA estimation, as the name implies, aims at finding arriving angles of impinging signals. Those obtained DOAs can be used to implement beamforming to enhance beams toward desired direction(s), or localize target(s) with distributed sensor array networks. In addition, while applied in wireless communications, DOA based beamforming technique evidently improves its performance as it is able to increase the channel capacity as well as

coverage range. Since the DOA information of impinging signals is essential to such areas, the DOA estimation problem has received considerable attentions in the community.

There are many existing high resolution DOA estimation methods, which can be categorized into beamforming based methods [11], subspace based methods [12, 13] and compressive sensing based methods [14, 15]. These methods have shown outstanding performances under the assumption that the phase information at the array of sensors is available and reliable, which requires to know phase response of each sensor precisely in advance. As a result, the phase difference of received signals between array sensors can be exploited effectively for DOA estimation. In practice, however, the phase information may not be reliable due to various reasons and in the extreme scenario, all phase information of received signals could be lost and only magnitude information is reserved. In this case, the coherence of received signals among array sensors is destroyed and the performance of these existing DOA estimation algorithms will degrade significantly.

Under such a scenario, a new class of non-coherent DOA estimation algorithms is developed in recent years [16–19], where only magnitude information at array sensors is considered in the formulation. Exploiting non-coherent measurements in the DOA estimation problem is able to free the system from phase error at sensors; however, those methods also face some challenges: 1) they cannot jointly use the information provided by multiple snapshots effectively; 2) the inherent ambiguity issue of non-coherent measurements obtained by the most popular uniform linear array (ULA) was resolved using a reference signal when only one unknown source impinges upon the array, and with more unknown signals, more reference signals are required. However, setting up reference signal(s) in practical operations is costly and difficult. In this thesis, based on the majorizaion-minimization (MM) technique and the proximal gradient method, an effective algorithm is developed for non-coherent DOA estimation with multiple snapshots. The ambiguities associated with non-coherent measurements of a ULA are resolved by different array structures instead of placing multiple reference signals. Furthermore, an off-grid signal model for sparsity based non-coherent DOA estimation is studied. Similar to the DOA estimation problem, a class of algorithms for target localisation based on distributed multiple sensor arrays is also developed. In addition

to the narrowband scenario, the wideband scenario is considered as an extension at a later stage.

1.2 Original Contributions

The main contributions of the thesis are listed as follows:

1. The non-coherent DOA estimation problem can be regarded as a sparse phase retrieval problem, and existing phase retrieval algorithms mainly consider a single snapshot. For multiple snapshots, a group sparsity based phase retrieval algorithm is developed in this thesis. Based on the idea of phase retrieval via majorizaion-minimization technique (PRIME), the problem is reformulated as a group Least Absolute Shrinkage and Selection Operator (LASSO) problem, which can be solved by the proximal gradient method. Nesterov acceleration is further implemented to increase its convergence speed. We refer to this algorithm as Fast jOint Group Sparse PhAse Retrieval (ToyBar). In addition, a new ambiguity called spatial order ambiguity is discussed in detail, which shows that a solution to avoid this ambiguity is to limit the inter-sensor spacing of the employed ULAs to be less than a quarter of the signal wavelength.

2. While employing the classic ULA structure for non-coherent DOA estimation of narrowband signals, at least one reference signal at one end of interested area with precisely known DOA is required, which is a challenge in practical array operations. Instead of placing reference signals, two array structures are suggested to tackle the ambiguities problem. By exploiting the non-linear property of the sinusoidal function, a dual-array structure is first proposed. On the other hand, it is also proved that the uniform circular array (UCA) structure is also capable of solving the ambiguities problem. With these two array structures, no reference signals are required when there are more than one incident signals; a reference signal is required in the scenario with only one incident signal, but the DOA of the reference signal can be arbitrary and unknown. Based on these two array structures, the proposed ToyBar algorithm can be applied directly without the need of reference signals.

3. One problem with the sparsity based method is that DOAs of incident signals are assumed to fall on the discrete grid points, while in practice this is usually not true. To deal with off-grid signals, a two step off-grid non-coherent DOA estimation methods with low complexity has been proposed, where the on-grid DOA of incident signals and its off-grid term are estimated separately. In addition to DOA estimation, the off-grid non-coherent source localization problem based on distributed sensor arrays is further studied. The source localization problem is formulated into a group sparsity based phase retrieval problem by dividing the area into two-dimensional (2-D) grids, and the non-coherent source localization problem is formulated into a sparsity based framework, where magnitude-only measurements at all observers can be exploited jointly. Under such a framework, a 2-D localization method is proposed and an off-grid source localization signal model is further investigated.

4. For traditional wideband DOA estimation problem, a common approach is applying discrete Fourier transform (DFT) to those measurements, and decomposing wideband signals into different frequency bins, where each bin provides a similar model as the narrowband one, when the number of DFT points is sufficiently large. However, for the non-coherent scenario, none of those methods can be applied since the magnitude operation destroys the coherency of signals. In order to estimate DOA of wideband signals with magnitude only measurements and limited snapshots, we first process the wideband signals in the time domain directly by employing the idea of convolutional sparse coding (CSC), based on which the non-coherent wideband DOA estimation problem can be formulated into a group sparsity based phase retrieval problem and solved by the proposed ToyBar algorithm.

1.3 Thesis Outline

The outline of the thesis is as follows:

Chapter 2 introduces basic ideas of DOA estimation of both narrowband and wideband signals. For narrowband signals, traditional DOA estimation methods including beamforming

based methods, subspaced based methods and compressive sensing based methods are reviewed. Especially, non-coherent DOA estimation and its ambiguities are discussed. For wideband signals, the DFT based signal model and existing sparsity based methods are presented. Some simulations are provided to show theirs performance for both narrowband and wideband signals.

In Chapter 3, an iterative algorithm based on proximal gradient is proposed for the multi-snapshot non-coherent DOA estimation problem to efficiently and effectively exploit multiple snapshots in a joint way. The spatial order ambiguity is discussed in detail. Simulations are provided to verify the effectiveness of the proposed method in comparison with the state of art.

In Chapter 4, non-coherent DOA estimation of narrowband signals without the need of reference signals is studied. A dual-array structure is first presented and two methods to solve unambiguous DOAs of impinging signals based on the structure are provided. The first method to solve inherent shift and mirroring ambiguities of non-coherent measurements is to separately estimate sinusoidal difference of both arrays and find their intersection. Then, a joint group sparsity based non-coherent DOA estimation method is further described with this specific array structure. Moreover, non-coherent DOA estimation based on a uniform circular array is also introduced to tackle the ambiguities issue.

In Chapter 5, a two-step off-grid non-coherent DOA estimation method is proposed: in the first step, DOAs are approximated with a coarser steering matrix. In the second step, their off-grid bias is estimated through an iterative process, which has a closed-form solution at each iteration. Based on the off-grid DOA estimation method, a two step off-grid source localization problem with magnitude-only measurements based on a distributed sensor array structure is presented at the end.

In Chapter 6, a wideband signal model under the CSC framework is described, based on which an $l_{2,1}$ norm based wideband DOA estimation method with coherent measurements is presented. It is shown that compared with traditional frequency-domain based method, the proposed time-domain CSC (TD-CSC) based method has a better performance but with a

higher computational complexity. Then, the TD-CSC model is extended to the non-coherent scenario and its effectiveness are demonstrated by computer simulations.

Finally, in Chapter 7, conclusion are drawn and an outlook on possible future work is provided.

Chapter 2

Review of DOA Estimation

2.1 Introduction to Antenna Arrays

In DOA estimation, we estimate the arriving angles of impinging signals in the presence of noise with the aid of an array of sensors. These sensors are placed at different spatial positions and the response of an array is related to its geometric structure. There are three types of array structures in general [20]: linear arrays, planar arrays and volumetric arrays. Fig. 2.1 provides a example of a uniform linear array (ULA) consisting of M isotropic sensors with an inter-sensor distance d and one signal is impinging from an angle θ measured from the broadside of the array.

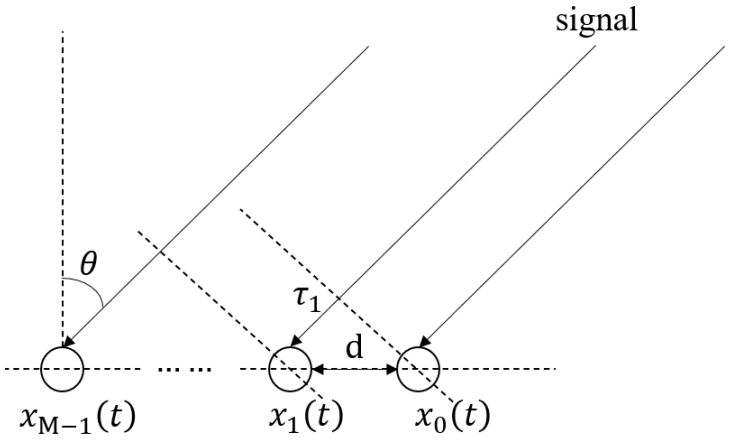

Fig. 2.1 Structure of a linear array.

Considering there are K signals emitted from the far field, the array response $x_m(t)$ of the m-th sensor at time t, $t \in \{1, ..., T\}$, can be expressed as:

$$x_m(t) = \sum_{k=1}^{K} s_k(t - \tau_{m,k}), \tag{2.1}$$

where $\tau_{m,k}$ represents the propagation delay between the 0-th and the m-th sensor of the k-th signal, being a function of incident angle θ, given by

$$\tau_{m,k} = m\frac{d\sin\theta_k}{c}, \tag{2.2}$$

with c being the signal propagation speed. Normally, signal $s_k(t)$ can be expressed in a complex form [3], as

$$s_k(t) = \alpha_k(t)e^{j\omega t}, \tag{2.3}$$

where ω is angular frequency of the signals, $\alpha(t)$ is the complex baseband modulating signal. Then, the k-th signal received at the m-th array is given by

$$s_k(t - \tau_{m,k}) = \alpha(t - \tau_{m,k})e^{j\omega(t-\tau_{m,k})}. \tag{2.4}$$

2.2 Narrowband DOA estimation

2.2.1 Signal Model

Under the narrowband scenario, the bandwidth of the signal is assumed narrow enough and the modulating signal should remain unchanged (i.e. $\alpha(t - \tau_{m,k}) \approx \alpha(t)$) [3], and (2.1) is changed to

$$\begin{aligned} x_m(t) &= \sum_{k=1}^{K} \alpha_k(t - \tau_{m,k})e^{j\omega(t-\tau_{m,k})} \\ &\approx \alpha_k(t)e^{j\omega(t-\tau_{m,k})} = \sum_{k=1}^{K} e^{-j\omega\tau_{m,k}}s_k(t). \end{aligned} \tag{2.5}$$

Since we normally work at the baseband, the carrier component $e^{j\omega t}$ in $s_k(t)$ will be ignored from now on. Substituting (2.2) into (2.5), we have

$$x_m(t) = \sum_{k=1}^{K} s_k(t) e^{-j2\pi m \frac{d}{\lambda}\sin(\theta_k)}, \tag{2.6}$$

where λ is signal wavelength. With a sampling frequency f_s, the array measurements of M sensors can be written in a discrete form as

$$\begin{aligned} \mathbf{x}[p] &= [x_0[p], ..., x_{M-1}[p]]^T \\ &= \mathbf{A}\mathbf{s}[p] + \mathbf{n}[p], \end{aligned} \tag{2.7}$$

with $\mathbf{n} = [n_0[p], ..., n_{M-1}[p]]$ being the noise vector at time index p, $(\cdot)^T$ is the matrix transpose operator, and $\mathbf{A}$ is called the steering matrix of the array, given by

$$\begin{aligned} \mathbf{A} &= [\mathbf{a}(\theta_k), ..., \mathbf{a}(\theta_k)], \\ \mathbf{a}(\theta_k) &= [1, e^{-j2\pi \frac{d}{\lambda}\sin(\theta_k)}, ..., e^{-j(M-1)2\pi \frac{d}{\lambda}\sin(\theta_k)}]^T. \end{aligned} \tag{2.8}$$

Collecting P snapshots to form $\mathbf{X} = \big[\mathbf{x}[0], ..., \mathbf{x}[P-1]\big]$, one has

$$\begin{aligned} \mathbf{X} &= \mathbf{A}\mathbf{S} + \mathbf{N}, \\ \mathbf{N} &= \big[\mathbf{n}[0], ..., \mathbf{n}[P-1]\big]. \end{aligned} \tag{2.9}$$

Fig. 2.2 summarizes different methods for narrowband DOA estimation, and details of each method are presented in the following sections.

2.2.2 Beamforming based Methods

This class of methods employs a beamformer to scan the whole spatial space and compute a pseudospectrum[21]. A beamformer is able to attenuate signal powers from uninterested direction while enhancing signal power from interested direction by exploiting the linear combination of array output $\mathbf{x}[p]$ with a weight vector $\mathbf{w}$. Mathematically, the beamformer output is given by

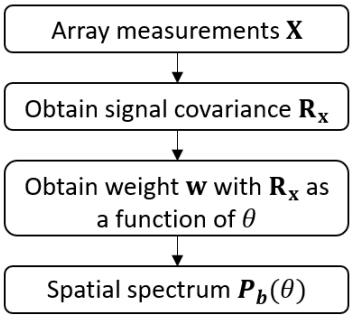

(a) Beamformer based method.

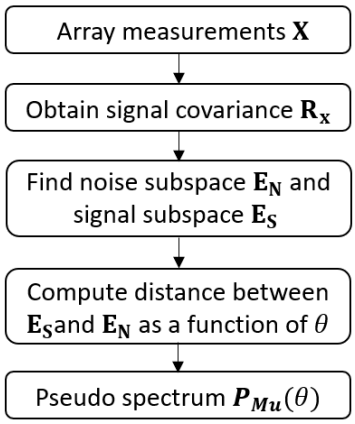

(b) Subspace based method (MUSIC).

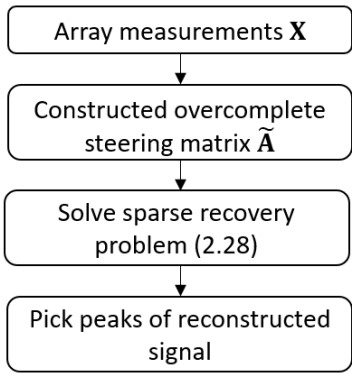

(c) Compressive sensing based method.

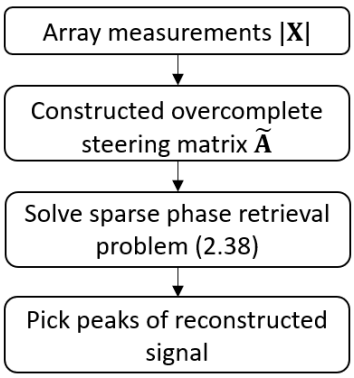

(d) Sparsity based non-coherent method.

Fig. 2.2 Summary of methods for narrowband DOA estimation.

$$z[p] = \mathbf{w}^H \mathbf{x}[p], \tag{2.10}$$

where $(\cdot)^H$ denotes the Hermitian transpose operator. DOA can be obtained by searching for the peak of power spectrum $P(\theta)$ of the array, given by

$$\begin{aligned} P(\theta) &= \mathbf{w}^H \mathbf{R}_x \mathbf{w}, \\ \mathbf{R}_x &= E\{\mathbf{x}[p]\mathbf{x}[p]^H\}, \end{aligned} \tag{2.11}$$

where $\mathbf{R}_x$ denotes the covariance matrix of array measurements and $E\{\cdot\}$ is the expectation operator. However, since $\mathbf{R}_x$ is not available in practice, it is normally estimated by

$$\mathbf{R}_x = \frac{1}{P}\sum_{p=0}^{P-1}\mathbf{x}[p]\mathbf{x}[p]^H. \tag{2.12}$$

One early method of this class is the Bartlett method [22], where the weight vector has a constant value for all its elements and forms a beam with unit magnitude response to the broadside of the array. Then, by steering the array in every possible direction (i.e. $\theta \in \{-90^\circ, 90^\circ\}$), the pseudospectrum can be obtained as a function of θ, denoted as

$$P_{Ba}(\theta) = \mathbf{a}^H(\theta)\mathbf{R}_x\mathbf{a}(\theta). \tag{2.13}$$

Another popular method is the minimum variance distortionless response beamformer (MVDR), also known as Capon beamformer in the narrowband case [11]. This beamformer is designed to minimize its total output power while maintaining a unit gain to the interested direction. The weight of the Capon beamformer is derived by the following optimization problem

$$\begin{aligned} &\min\ \mathbf{w}^H\mathbf{R}_x\mathbf{w} \\ &\text{subject to } \mathbf{w}^H\mathbf{a}(\theta) = 1. \end{aligned} \tag{2.14}$$

By using the Lagrange multipliers method, the Langrangian is given by

$$l(\mathbf{w},\eta) = \mathbf{w}^H\mathbf{R}_x\mathbf{w} + \eta(\mathbf{w}^h\mathbf{a}(\theta) - 1) + \eta^*(\mathbf{a}^H\mathbf{w} - 1), \tag{2.15}$$

where $(\cdot)^*$ is the complex conjugate operator. Differentiating the Langrangian with respect to $\mathbf{w}^H$, we have

$$\nabla l(\mathbf{w},\eta) = \mathbf{R}_x\mathbf{w} + \eta\mathbf{a}(\theta) = 0. \tag{2.16}$$

Then, the optimal weight of the beamformer is

$$\mathbf{w} = -\eta\mathbf{R}_x^{-1}\mathbf{a}(\theta). \tag{2.17}$$

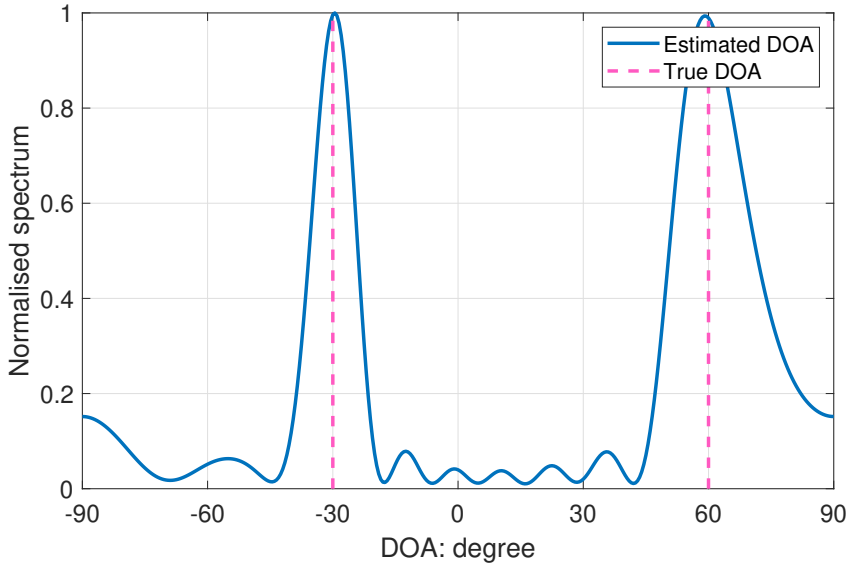

Fig. 2.3 Normalized spectrum of the Bartlett method, with 2 signals, 100 snapshots, 10 sensors, and SNR = 10 dB.

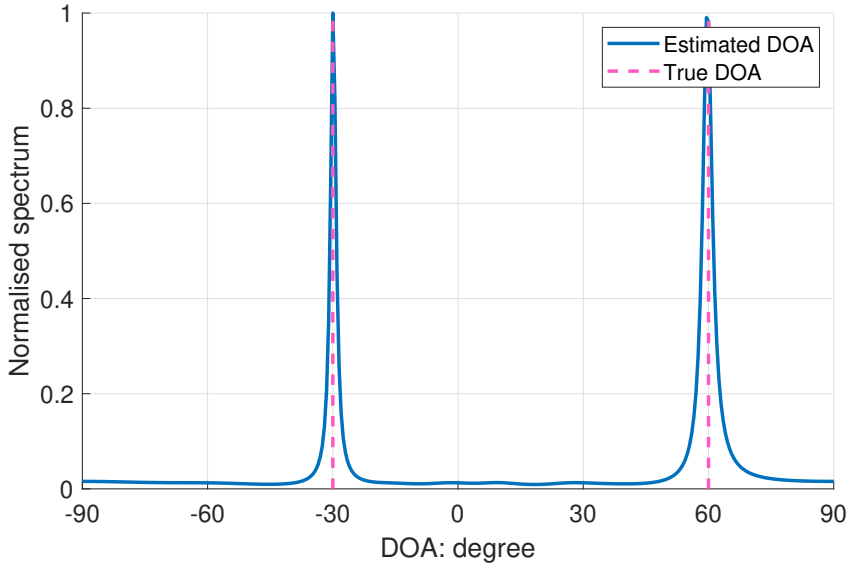

Fig. 2.4 Normalized spectrum of the Capon method, with 2 signals, 100 snapshots, 10 sensors, and SNR = 10 dB.

Since $\mathbf{w}^H\mathbf{a}(\theta) = 1$, it has

$$-\eta\mathbf{a}^H(\theta)\mathbf{R}_x^{-1}\mathbf{a}(\theta) = 1, \tag{2.18}$$

and the optmal weight is given by

$$\eta = \frac{-1}{\mathbf{a}^H(\theta)\mathbf{R}_x\mathbf{a}(\theta)}. \tag{2.19}$$

Substituting (6) into (4), the weight vector is

$$\mathbf{w} = \frac{\mathbf{R}_x^{-1}\mathbf{a}(\theta)}{\mathbf{a}^H(\theta)\mathbf{R}_x^{-1}\mathbf{a}(\theta)}. \tag{2.20}$$

Then, the output power of the Capon beamformer corresponding to direction θ is given by [2, 3]

$$P_{Ca}(\theta) = \frac{1}{\mathbf{a}^H(\theta)\mathbf{R}_x^{-1}\mathbf{a}(\theta)}. \tag{2.21}$$

Figs. 2.3 and 2.4 show the DOA results of the beamforming based methods employing a ULA shown in Fig. 2.1 with $M = 10$ sensors, where $K = 2$ signals arrive from directions $\boldsymbol{\theta} = [-30^\circ, 60^\circ]$. However, although the beamforming based methods can identify the DOAs of incident signals effectively, there resolution is rather limited [21].

2.2.3 Subspace Based Methods

The subspace based methods assume that the signals are uncorrelated with each other, and apply eigen-decomposition to the covariance matrix $\mathbf{R}_x$ to obtain two subspaces: signal space and noise subspace, which are spanned by different eigen-vectors [3, 13]. The signal subspace is orthogonal to the noise subspace, and the noise subspace is spanned by the eigenvectors associated with the smaller eigenvalues while the signal subspace is spanned by the eigenvectors associated with its larger ones. Under the assumption that signals and noise are uncorrelated, the covariance matrix $\mathbf{R}_x$ can be formulated as

$$\begin{aligned} \mathbf{R}_x &= \mathbf{X}\mathbf{X}^H = \mathbf{A}\mathbf{R}_s\mathbf{A}^H + \mathbf{R}_n \\ &= \mathbf{X}\mathbf{X}^H = \mathbf{A}\mathbf{R}_s\mathbf{A}^H + \sigma_m^2\mathbf{I}_M, \end{aligned} \tag{2.22}$$

where $\mathbf{R}_s$ and $\mathbf{R}_n$ are covariance matrices of signal and noise separately, σ_m represents noise power and $\mathbf{I}_M$ is the $M \times M$ identity matrix. Applying eigen-decomposition to $\mathbf{R}_x$, one has

$$\mathbf{R}_x = \mathbf{E}_M \mathbf{\Lambda} \mathbf{E}_M^H = \sum_{m=1}^{M} \lambda_i \mathbf{e}_i \mathbf{e}_i^H, \tag{2.23}$$

where $\mathbf{e}_i$ and λ_i denote the i-th eigenvector and eigenvalue separately, while $\mathbf{E}_M = [\mathbf{e}_1, .., \mathbf{e}_M]$ and $\boldsymbol{\lambda} = \text{diag}\{\lambda_1, ..., \lambda_M\},\ \lambda_1 > ..., \lambda_M$. $\text{diag}\{\cdot\}$ generates a diagonal matrix from its entries. Since $\mathbf{R}_x \mathbf{e}_i = \lambda_i \mathbf{e}_i$, we have

$$\begin{aligned} \lambda_i \mathbf{e}_i &= (\mathbf{A}\mathbf{R}_s\mathbf{A}^H + \sigma_m^2 \mathbf{I}_M)\mathbf{e}_i, \\ \mathbf{A}\mathbf{R}_s\mathbf{A}^H \mathbf{e}_i &= (\lambda_i - \sigma_m^2)\mathbf{e}_i. \end{aligned} \tag{2.24}$$

While $K < M$ (i.e. the number of impinging signals is less than the number of sensors), $\mathbf{A}\mathbf{R}_s\mathbf{A}^H$ is singular with rank K. As a result, there are $M - K$ eigenvalues of $\mathbf{A}\mathbf{R}_s\mathbf{A}$ equal to 0. Thus, it satisfies $\sigma_m^2 = \lambda_i$ when $M \geq i > K$. Then, (2.24) can be simplified as

$$\mathbf{A}\mathbf{e}_i = 0,\ M \geq i > K, \tag{2.25}$$

which implies that noise subspace spanned by the eigenvectors associated with noise are orthogonal to the signal subspace spanned by the steering vectors of impinging signals.

One most popular subspace method exploiting the orthogonality between the signal subspace and nosie subspace is the MUltiple SIgnal Classification (MUSIC) method [12]. This method is the most studied subspace based method and there are many variants existing such as root-MUISC [23], constrained MUSIC [24], and gold-MUSIC [25].

By defining the basis of the noise subspace as $\mathbf{E}_N = [\mathbf{e}_{K+1}, ..., \mathbf{e}_M]$, this method searches for the K steering vectors which are most orthogonal to the noise subspace through calculating the Euclidean distance between the two subspaces as $\mathbf{a}^H(\theta)\mathbf{E}_N\mathbf{E}_N^H\mathbf{a}(\theta)$. The MUSIC pseudospectrum can be evaluated as a function of θ, given by

$$P_{Mu}(\theta) = \frac{1}{\mathbf{a}^H(\theta)\mathbf{E}_N\mathbf{E}_N^H\mathbf{a}(\theta)}. \tag{2.26}$$

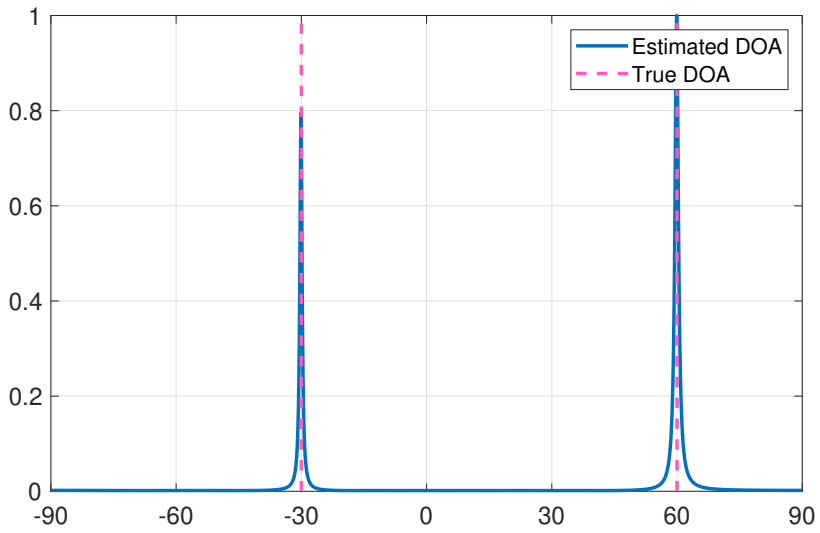

Fig. 2.5 Normalized spectrum of MUSIC, with 2 signals, 100 snapshots, 10 sensors, and SNR = 10 dB.

An example of DOA spatial spectrum with MUSIC is shown in Fig. 2.5.

2.2.4 Compressive Sensing Based Methods

In the past fifteen years, compressive sensing has been a very active research area, where the signals are assumed to be sparse in some domain [26]. A signal is said to be sparse if there is only a few entries of it are nonzero. Since the signals are generally sparse in the spatial domain, compressive sensing has been applied to DOA estimation problems and studied extensively [14, 15, 27–30]. Compared to the traditional beamforming based methods and subspace based methods presented earlier, the compressive sensing based methods require less number of signal snapshots and the impinging signals are not necessarily to be uncorrelated with each other [31].

Under the sparsity framework, the angle area of interest, i.e. from -90° to 90°, is divided into G ($G \gg K$) grid points, where there are only K out of G incident signals. Correspondingly, an overcomplete steering matrix $\tilde{\mathbf{A}} \in \mathbb{C}^{M\times G}$ is constructed, with each column representing a steering vector of a potential incident angle, given by

$$\tilde{\mathbf{A}} = [\mathbf{a}(\theta_1), ..., \mathbf{a}(\theta_G)]. \tag{2.27}$$

Accordingly, the signal vector $\mathbf{s}[p]$ is extended to a $G \times 1$ sparse vector

$$\tilde{\mathbf{s}}[p] = [s_1[p], ..., s_G[p]]^T. \tag{2.28}$$

Note that, there are only K entries at the corresponding incident angles supposed to be non-zero. As a result, (2.7) is reformulated as

$$\mathbf{x}[p] = \tilde{\mathbf{A}}\tilde{\mathbf{s}}[p] + \mathbf{n}[p]. \tag{2.29}$$

Unlike previous methods, $\tilde{\mathbf{A}}$ is known in advance. Thus, the DOA estimation problem is equivalent to finding the support of $\tilde{\mathbf{s}}[p]$ (i.e. non-zero positions of vector $\tilde{\mathbf{s}}[p]$), which can be solved by the following minimization problem

$$\begin{aligned} &\min \|\tilde{\mathbf{s}}\|_0 \\ &\text{subject to } \|\mathbf{x} - \tilde{\mathbf{A}}\tilde{\mathbf{s}}[p]\|_2^2 \leq \varepsilon, \end{aligned} \tag{2.30}$$

where $\|\cdot\|_0$ denots the l_0 norm of its variable, which enforces sparsity, $\|\cdot\|$ denotes the l_2 norm, and ε is the allowable error bound. Although the l_0 norm is non-convex in general [14], many greedy algorithms have been proposed to solve this problem, such as matching pursuit (MP)[32] and orthogonal matching pursuit (OMP) [33].

Alternatively, another method to solve the problem is relaxing the l_0 norm by the l_1 norm, which makes the problem convex [31]. As a result, the DOA estimation problem under the sparsity frame work is updated to

$$\begin{aligned} &\min \|\tilde{\mathbf{s}}\|_1 \\ &\text{subject to } \|\mathbf{x} - \tilde{\mathbf{A}}\tilde{\mathbf{s}}[p]\|_2^2 \leq \varepsilon, \end{aligned} \tag{2.31}$$

where $\|\cdot\|_1$ is the l_1 norm.

The above sparsity based method considers only one snapshot, and for multiple snapshots, (2.9) is changed to

$$\begin{aligned} \mathbf{X} &= \tilde{\mathbf{A}}\tilde{\mathbf{S}} + \mathbf{N}, \\ \tilde{\mathbf{S}} &= [\tilde{\mathbf{s}}[1], ..., \tilde{\mathbf{s}}[P]]. \end{aligned} \tag{2.32}$$

Obviously, signal matrix $\tilde{\mathbf{S}}$ is row sparse, with K rows corresponding to real DOAs being non-zero valued. Therefore, the DOA estimation problem with multiple snapshots is reformulated into a multiple measurement vector recovery (MMV) problem [34],

$$\begin{aligned} &\min \|\tilde{\mathbf{S}}\|_{2,1} \\ &\text{subject to } \|\mathbf{X} - \tilde{\mathbf{A}}\tilde{\mathbf{S}}\|_F^2 \leq \varepsilon, \end{aligned} \tag{2.33}$$

where $\|\cdot\|_{2,1}$ is the $l_{2,1}$ norm, which promotes the row sparsity of $\tilde{\mathbf{S}}$ by taking the l_2 norm of its row vectors, forming a new column vector, and finally taking the l_1 norm of the new column vector, while $\|\cdot\|_F$ represents the Frobenius norm. The positions of non-zero rows of the reconstructed signal matrix $\tilde{\mathbf{S}}$ correspond to estimated DOAs of impinging signals.

With the sparsity based multi-snapshot signal model, an efficient method called l_1-SVD was proposed in [14]. In this method, singular value decomposition (SVD) is applied to $\mathbf{X}$,

$$\mathbf{X} = \mathbf{U}\mathbf{L}\mathbf{V}^H. \tag{2.34}$$

Then, a pesudo measurement matrix $\mathbf{X}_{svd}$ is constructed as

$$\mathbf{X}_{svd} = \mathbf{U}\mathbf{L}\mathbf{D}_k = \mathbf{X}\mathbf{V}\mathbf{D}_K, \tag{2.35}$$

where $\mathbf{D}_k = [\mathbf{I}_K, \mathbf{0}]^T$, $\mathbf{I}_K$ is the $K \times K$ identity matrix and $\mathbf{0}$ is a $(P-K) \times K$ all-zero matrix. Similarly, we can define $\tilde{\mathbf{S}}_{svd}$ and $\mathbf{N}_{svd}$ and have

$$\tilde{\mathbf{X}}_{svd} = \tilde{\mathbf{A}}\tilde{\mathbf{S}}_{svd} + \mathbf{N}_{svd}. \tag{2.36}$$

As result, the dimension of signals to be recovered has been reduced from P to K, and by enforcing sparsity in the spatial domain, the DOA estimation results can be obtained by solving the following minimization problem,

$$\begin{aligned} &\min \|\tilde{\mathbf{S}}_{svd}\|_{2,1} \\ &\text{subject to } \|\mathbf{X}_{svd} - \tilde{\mathbf{A}}\tilde{\mathbf{S}}_{svd}\|_F^2 \leq \varepsilon, \end{aligned} \tag{2.37}$$

On the other hand, another method called sparse representation of array covariance vectors (SRACV) was proposed in [35], where the measurement covariance matrix $\mathbf{R}_x$ described in (2.22) is reformulated as

$$\begin{aligned} \mathbf{R}_x &= \mathbf{A}\mathbf{R}_s\mathbf{A}^H \\ &= \mathbf{A}\mathbf{L} + \sigma_n^2\mathbf{I}_M. \end{aligned} \tag{2.38}$$

Similar to l_1-SVD, by employing an over-complete steering matrix $\tilde{\mathbf{A}}$ and $\tilde{\mathbf{L}}$, the DOA would be estimated by minimizing

$$\begin{aligned} &\min \|\tilde{\mathbf{L}}\|_{2,1} \\ &\text{subject to } \|\mathbf{X}_{svd} - \tilde{\mathbf{A}}\tilde{\mathbf{L}}\|_F^2 \leq \varepsilon. \end{aligned} \tag{2.39}$$

Both (2.37) and (2.39) can be solved by existing optimisation algorithms or toolboxes, such as proximal gradient [36] and cvx [37]. A simulation result based on the l_1-SVD method with a grid stepsize 0.5° is provided in Fig. 2.6.

2.2.4.1 Grid refinement

Since the estimation results of the proposed method are dependent on the grid size in the angle domain. A denser grid, i.e. large G, usually leads to a more accurate DOA results, but with a much higher computational complexity [14]. Therefore, instead of creating a dense grid initially, a coarse grid is firstly made; based on the initial DOA estimation results, a denser steering matrix is then built around the estimated locations of incident signals, and the

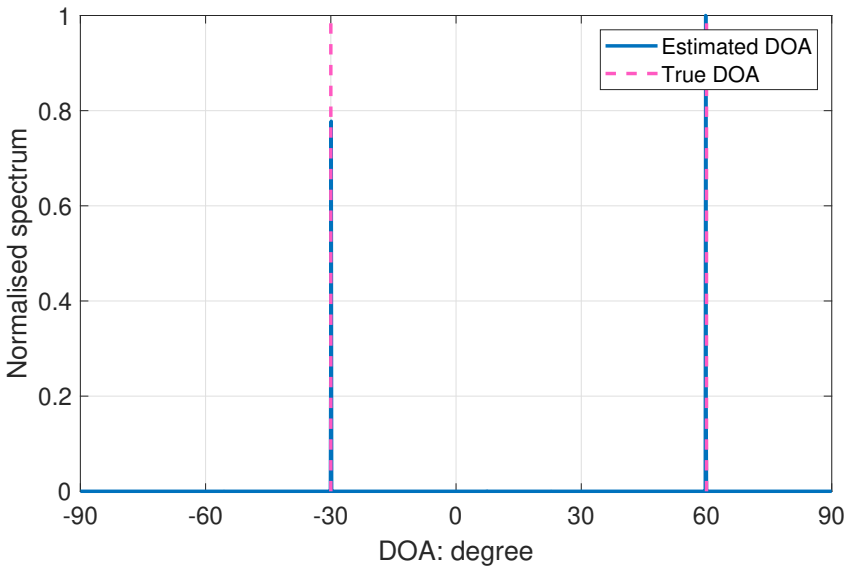

Fig. 2.6 Normalized spectrum of the l_1-SVD method, with 2 signals, 100 snapshots, 10 sensors, and SNR = 10 dB.

algorithm is employed again to find a more accurate DOA. The process of grid refinement is as follows,

1) Construct overcomplete steering matrix $\tilde{\mathbf{A}}$ with a coarse grid $\tilde{\boldsymbol{\theta}}^{(1)} = [\theta_1^{(1)}, ..., \theta_G^{(1)}]$, where the area of interest is limited within $\{\theta_1^{(1)}, \theta_G^{(1)}\}$.

2) Approximating the rough DOAs of impinging signals by solving (2.28).

3) Obtained a new refined grid $\tilde{\boldsymbol{\theta}}^{(2)}$ around the rough locations estimated with the coarse grid $\tilde{\boldsymbol{\theta}}^{(1)}$, and construct another overcomplete steering matrix.

4) Solve (2.28) with the refined steering matrix and obtain refined results.

Fig. 2.7 illustrates the process of grid refinement, where the refined grid is based upon the intervals around the rough results obtained with a coarse grid used in the previous step.

2.2.5 Non-Coherent DOA Estimation

The above DOA estimation methods implicitly assume that the phase information is available at the array of sensors and those high resolution methods often rely on this assumption. However, in real applications, the phase information may not be reliable. Under such a scenario, each sensor may suffer from independent phase errors and for the noiseless case,

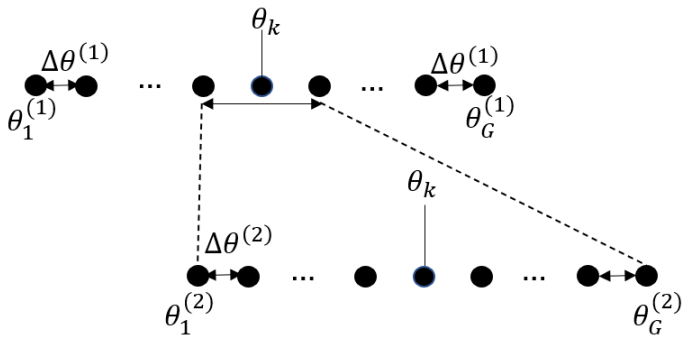

Fig. 2.7 Illustration of grid refinement.

the array measurement would be changed to

$$\mathbf{X} = \mathbf{EAS}, \tag{2.40}$$

where $\mathbf{E}$ is an $M \times M$ diagonal matrix with random phase terms, representing the phase errors at the sensor array. In the presence of phase errors, the performance of those aforementioned methods will degrade significantly [16, 38, 39].

In order to overcome this challenge, non-coherent DOA estimation has been studied recently, where only magnitude information is captured at all sensors. The signal model is changed to

$$\mathbf{Y} = |\mathbf{EAS}| + \mathbf{N}, \tag{2.41}$$

where $|\cdot|$ represents element-wise absolute value operator. Since the measurement is magnitude only and $\mathbf{E}$ is diagonal, we have

$$|\mathbf{EAS}| = |\mathbf{AS}|, \tag{2.42}$$

which indicates that, unlike those traditional methods, phase errors at sensors of an array have no effect on magnitude-only measurements [16], and hence, in the remaining part of this thesis, the phase error matrix $\mathbf{E}$ is dropped for convenience.

For such a non-coherent DOA estimation problem, [16] formulated it into a sparse phase retrieval form, given by

$$\begin{aligned} &\min \ ||\tilde{\mathbf{S}}||_{2,0} \\ &\text{subject to } \|\mathbf{Y}^2 - |\tilde{\mathbf{A}}\tilde{\mathbf{S}}|^2\|_F^2 < \varepsilon. \end{aligned} \tag{2.43}$$

For the $l_{2,0}$ norm of a matrix, it takes the l_2 norm of its row vectors, then forms a new column vector, and finally takes the l_0 norm of the new column vector. An existing greedy phase retrieval algorithm named GESPAR [40] is modified to solve it, as proposed in [16]. This algorithm is based on the local search method [41] which updates support of signals iteratively, and approximates best solution under given support by the damped Gaussian Newton (DGN) method [42].

The modified GESPAR [16] firstly generates a random support (i.e. K non-zero rows), and with the support, each column of the objective function (2.43) is reformulated as

$$\min_{\mathbf{s}_k[p]} \ \|(\mathbf{y}^2[p] - |\mathbf{A}_K \mathbf{s}_k[p]|^2\|_2^2, \tag{2.44}$$

where $\mathbf{s}_k \in \mathbb{C}^K \times 1$ represents the K possible nonzero elements of $\tilde{\mathbf{S}}$ and $\mathbf{A}_k$ are column vectors of $\tilde{\mathbf{A}}$ corresponding to the given support. The problem can be solved via DGN. However, for P snapshots in total, the method has to be applied to different snapshots separately. Then, support at each iteration is updated by a swap between support and off-support. The index of support to be chosen for swap is the entries with the smallest absolute value, while index of off-support for swap corresponds to largest absolute value of the entries of $\sum_{p=0}^{P-1} \nabla(\|\mathbf{y}^2[p] - |\tilde{\mathbf{A}}\tilde{\mathbf{s}}[p]|^2\|_2^2)$, where $\nabla(\cdot)$ represents gradient of its variable. This process continues until the iteration number exceed the predetermined maximum number of swaps.

In addition to the sparse phase retrieval method, a frequency estimation formulation is further proposed [17, 18], where the signal model is reformulated as

$$\begin{aligned} y_m^2[p] &= |\sum_{k=1}^{K} |s_k| e^{j\gamma_k} e^{-j2\pi \frac{d}{\lambda} \sin(\theta_k)}|^2, \\ &= \sum_{k=1}^{K} \sum_{k'=1}^{K} |s_k||s_{k'}| e^{j(\gamma_k - \gamma_{k'})} e^{-j2\pi m \frac{d}{\lambda}(\sin(\theta_k) - \sin(\theta_k'))}, \end{aligned} \tag{2.45}$$

where γ_k denotes the phase of the k-th signal. It can be observed from (2.45) that there are $K(K-1)/2$ harmonic terms, and only sinusoidal difference $\Delta\sin(\theta)_{kk'} = \sin(\theta_k) - \sin(\theta'_k)$ can be estimated. Moreover, its estimation accuracy relies on its frequency resolution, which requires a large number of measurements. In addition, this method fails to utilize the information of multiple snapshots jointly to improve its performance.

2.2.6 Inherent Ambiguities

Obviously, reconstructing signals from (2.43) and (2.45) with a ULA suffers from three ambiguities [16] (i.e. signals with different set of DOAs has the same magnitude measurement), and two of them would affect the DOA estimation results: one is mirroring and the other is spatial shift.

For mirroring, it refers to the phenomenon that the conjugated version of the original sources from the angles $[-\theta_1, \cdots, -\theta_K]$ will generate a set of measurements with the same magnitude as the original sources from $[\theta_1, \cdots, \theta_K]$.

$$\check{x}_m = \sum_{k=1}^{K} s_k^* e^{-jm2\pi\frac{d}{\lambda}\sin(-\theta_k)} = x_m^*, \tag{2.46}$$

where x_m is the measurement at the m-th sensor with $m = [0, ..., M-1]$, the time index p has been dropped for convenience, and the effect of noise has been ignored. Obviously, mirroring measurement $\check{x}_m$ shares the same magnitude as the original measurement x_m.

For the spatial shift ambiguity, it refers to the case that the received array signals are phase shifted by an unknown amount ϕ as follows

$$\check{x}_m = e^{-jm\phi} x_m = \sum_{k=1}^{K} s_k e^{-jm2\pi\frac{d}{\lambda}\sin(\theta_k)} e^{-jm\phi}. \tag{2.47}$$

In this case, with the same set of source signals, a set of DOA angles, $\ddot{\theta}_k$ satisfying

$$\sin\ddot{\theta}_k = \sin\theta_k + \frac{\phi\lambda}{2\pi d} \tag{2.48}$$

for all k, would generate the same magnitude-only measurements. One interesting property of this ambiguity is that, the DOA angle order stays the same, i.e. with $\sin\theta_1 < \sin\theta_2 < \cdots < \sin\theta_K$, we also have $\sin\ddot{\theta}_1 < \sin\ddot{\theta}_2 < \cdots < \sin\ddot{\theta}_K$ and this ambiguity will not affect the relevant sinusoidal distance $\Delta s_{\theta,kk'} = (\sin\theta_k + \frac{\phi\lambda}{2\pi d}) - (\sin\theta_{k'} + \frac{\phi\lambda}{2\pi d})$, $k \neq k'$ due to the common phase shift involved for all DOA angles.

These two ambiguities can be resolved by placing reference signal(s) at one end of interest area, as suggested in [16]. For spatial shift ambiguity, a reference signal with a known DOA forces the spatial shift variable ϕ to be zero, and thus resolves this ambiguity. The mirroring ambiguity is caused by the even property of the cosine function (the non-coherent measurements can be seen as sum of several cosine function), which means both $\pm m\frac{2\pi d}{\lambda}(\sin(\theta_k) - \sin(\theta_{ref})$ are possible solution candidates. The solution can be restricted to either $m\frac{2\pi d}{\lambda}(\sin(\theta_k) - \sin(\theta_{ref})$ with a reference signal at lower end or $-m\frac{2\pi d}{\lambda}(\sin(\theta_k) - \sin(\theta_{ref})$ with a reference signal at a high end.

A design example for the non-coherent DOA estimation result with $M = 20$ sensors, is given in Fig. 2.8 and Fig. 2.9, where the modified GESPAR [16] is applied as estimators. Two scenarios are considered: 1) $K = 1$ impinging signal coming from $\theta = 30^\circ$ and a reference signal placed at 0°; 2) $K = 2$ signals arriving from $[30^\circ, 60^\circ]$, where the reference signals are placed at $[0^\circ, 10^\circ]$.

2.3 Wideband DOA Estimation

2.3.1 Signal Model

Assume that there are K wideband signals $s_k(t)$ from directions θ_k, $k = 1, 2, ..., K$, respectively, impinging on a ULA of M sensors with an adjacent sensor spacing d. Since $\alpha(t - \tau_{m,k}) \neq \alpha(t)$ dose not hold for wideband signals, the corresponding received signal (2.1) at the m-th sensor is

$$x_m(t) = \sum_{k=1}^{K} \delta(t - \tau_{m,\theta_k}) * s_k(t) + n_m(t), \tag{2.49}$$

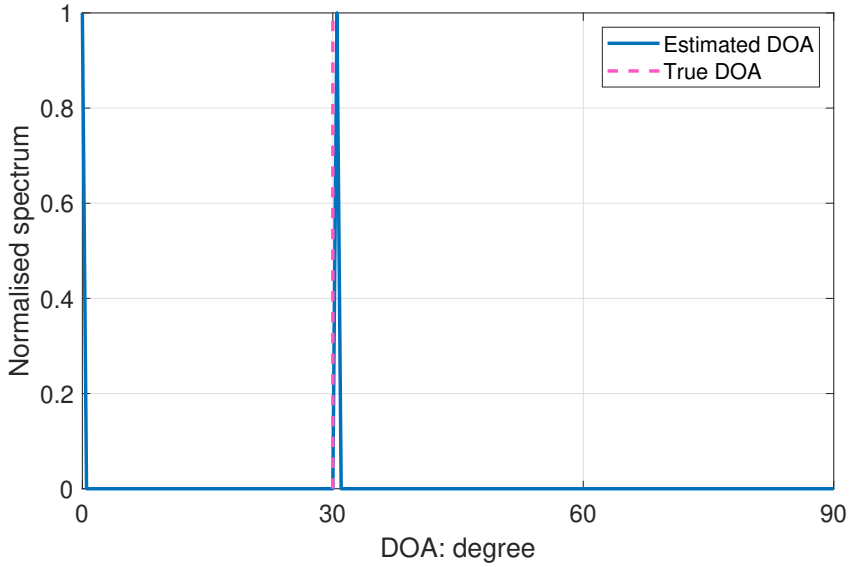

Fig. 2.8 Normalized spectrum of the GESPAR, with 1 signal, 5 snapshots, 20 sensors, and SNR = 15 dB.

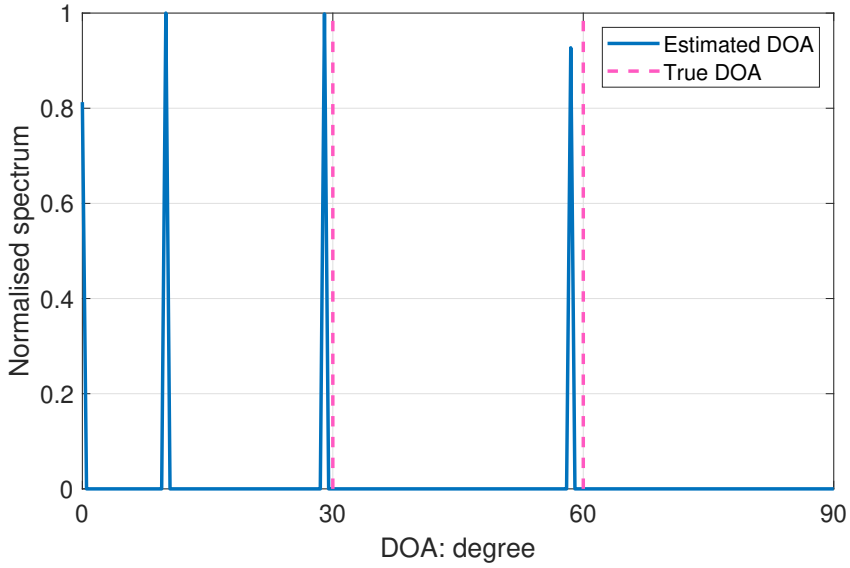

Fig. 2.9 Normalized spectrum of the GESPAR, with 2 signals, 5 snapshots, 20 sensors, and SNR = 15 dB.

where $n_m(t)$ is noise, c is signal propagation speed, and $\tau_{m,\theta_k} = \frac{md\sin\theta_k}{c}$ is the time delay of the k-th signal with DOA θ_k at the m-th sensor, $m \in \{0,...,M-1\}$, with the zeroth sensor regarded as the reference one.

With a sampling frequency f_s, the received signal at the m-th sensor can be expressed in a discrete convolution form [20], given by

$$x_m[p] = \sum_{k=1}^{K}(\sum_{i=-\infty}^{+\infty} a_{i,m,\theta_k} s_k[p-i]) + n_m[p], \tag{2.50}$$

where $s_k[p]$ represents the p-th snapshot of the k-th source signal, T_s is its sampling period, and

$$a_{i,m,\theta_k} = \text{sinc}(i - \tau_{m,\theta_k}/T_s). \tag{2.51}$$

$\text{sinc}(\cdot)$ is the normalized sinc function, defined as

$$\text{sinc}(v) = \sin(\pi v)/(\pi v) \tag{2.52}$$

2.3.2 Frequency based method

For such a wideband DOA estimation problem, a common approach is applying an L-point discrete Fourier transform (DFT) to those measurements, and decomposing wideband signals into different frequency bins, with each bin containing $R = \frac{P}{L}$ frequency snapshots. Then, the r-th frequency snapshot of the l-th subband at the m-th sensor after L-point DFT is modelled as

$$X_m[l,r] = \sum_{p=0}^{L-1} x_m[L(r-1)+p]e^{-j\frac{2\pi l}{L}p}. \tag{2.53}$$

Denoting $\mathbf{X}[l,r] = [X_0[l,r],...,X_{M-1}[l,r]]^T$, the signal model of the l-th subband with R frequency snapshots can be expressed as

$$\begin{aligned} \mathbf{X}[l] &= [\mathbf{X}[l,1],...,\mathbf{X}[l,R]], \\ &= \mathbf{A}(l)\mathbf{S}[l] + \mathbf{N}[l], \end{aligned} \tag{2.54}$$

where $\mathbf{A}(l) = [\mathbf{a}(l,\theta_1),...,\mathbf{a}(l,\theta_K)]$ is the steering matrix of the l-th subband, with

$$\mathbf{a}(l,\theta_k) = [1, e^{-j2\pi\frac{d}{\lambda_l}\sin(\theta_K)},...,e^{-j(M-1)2\pi\frac{d}{\lambda_l}\sin(\theta_K)}]^T, \tag{2.55}$$

where λ_l is the wavelength corresponding to the l-th subband, and

$$\begin{aligned}\mathbf{S}[l] &= [\mathbf{S}[l,0],...,\mathbf{S}[l,R-1]],\\ \mathbf{S}[l,r] &= [\mathbf{S}_1[l,r],...,\mathbf{S}_K[l,r]]^T,\end{aligned} \tag{2.56}$$

represents signals of the l-th subband. Under the subband model (2.54), each subband enjoys a similar signal model as the narrowband one, and those existing methods can be applied.

In [43], an effective compressive sensing based approach is proposed, where the DOA of the impinging signals across subbands of interest is estimated simultaneously by introducing $l_{2,1}$ norm to different subbands (i.e., the signal of different frequencies share the same spatial support). Under such a framework, an overcomplete steering matrix $\tilde{\mathbf{A}}(l)$ at frequency l is firstly built in a similar manner as in (2.27). Then, a block diagonal matrix $\tilde{\mathbf{A}}_b$ containing $Q,\ Q \leq L$ subband of interested is constructed, expressed as

$$\tilde{\mathbf{A}}_b = \text{blkdiag}\{\tilde{\mathbf{A}}(l_0),...,\tilde{\mathbf{A}}(l_{Q-1})\}, \tag{2.57}$$

where $\text{blkdiag}(\cdot)$ represents the block diagonal operator. Accordingly, the array measurements including all subbands of interest can be formulated as

$$\begin{aligned}\mathbf{X}_b &= [\mathbf{X}^T[l_0],...,\mathbf{X}^T[l_{Q-1}]]^T\\ &= \tilde{\mathbf{A}}_b\tilde{\mathbf{S}}_b + \mathbf{N}_b,\\ \tilde{\mathbf{S}}_b &= [\tilde{\mathbf{S}}^T[0],...,\tilde{\mathbf{S}}^T[Q-1]]^T.\end{aligned} \tag{2.58}$$

Finally, the wideband DOA estimation can be obtained by solving the following minimization problem

$$\begin{aligned}&\min \|\tilde{\mathbf{S}}_b\|_{2,1}\\ &\text{subject to} \|\mathbf{X}_b - \tilde{\mathbf{A}}_b\tilde{\mathbf{S}}_b\|_F^2.\end{aligned} \tag{2.59}$$

Note that, $\tilde{\mathbf{S}}_b$ is a $GQ \times I$ signal matrix, and in addition to its row sparsity, each subband also shares the same spatial sparsity. An example with a ULA of $M = 10$ sensors is presented in Fig. 2.10. The DOAs of signals are set as -20°, and 20°, and the frequency band of interest is within normalized frequency $[0.5\pi, \pi]$ with $I = 100$.

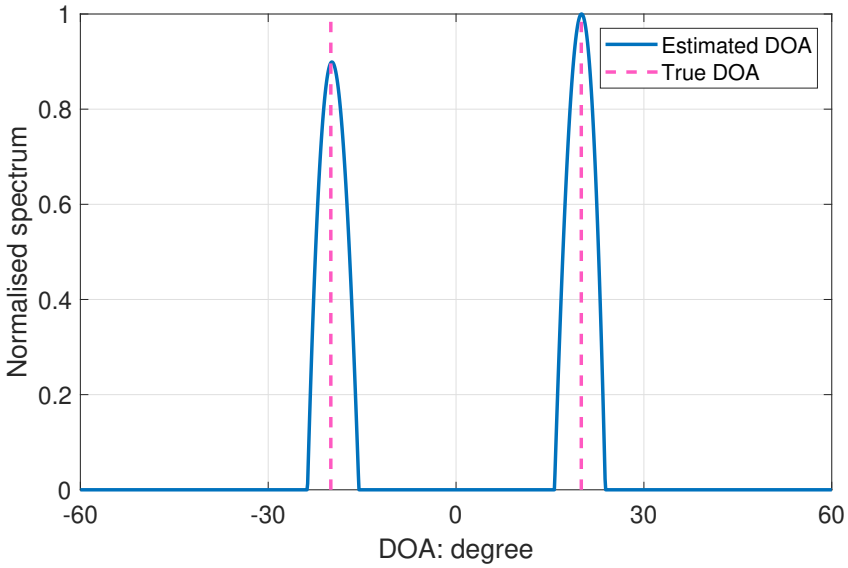

Fig. 2.10 Normalized spectrum of wideband signals, with 2 signals, 100 snapshots, 10 sensors, and SNR = 10 dB.

2.4 Simulations

In this section, the estimation performance of different DOA estimation methods are evaluated by root mean squared error (RMSE), which is defined as

$$\text{RMSE} = \sqrt{\frac{1}{IK}\sum_{i=1}^{I}\sum_{k=1}^{K}(\theta_k^i - \theta_{e,k}^i)^2}, \tag{2.60}$$

where i refers to the i-th trial while $\theta_{e,k}$ and θ_k represent estimated DOA and true DOA of the k-th impinging signals, separately,

The RMSE results versus different SNR for both coherent and non-coherent methods are considered in Fig. 2.11, with each point obtained by averaging over 100 independent trials.

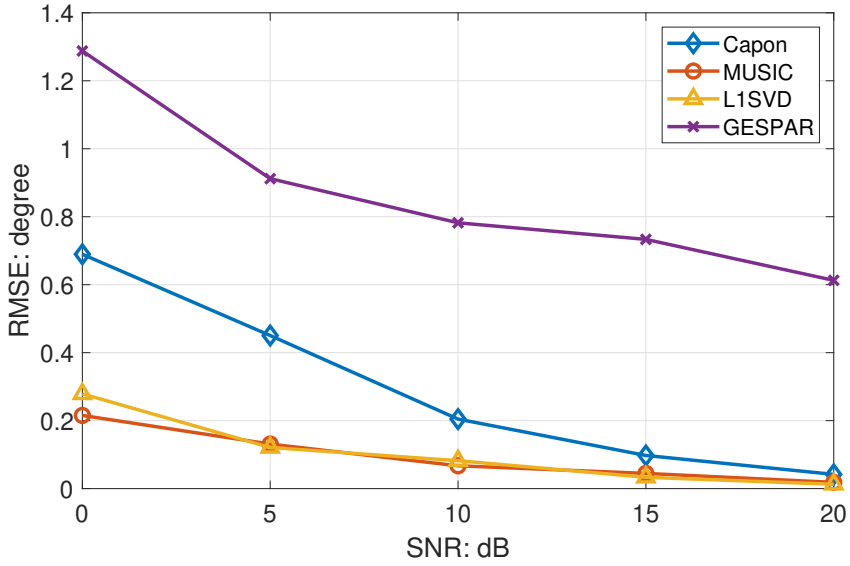

Fig. 2.11 RMSE vs SNR.

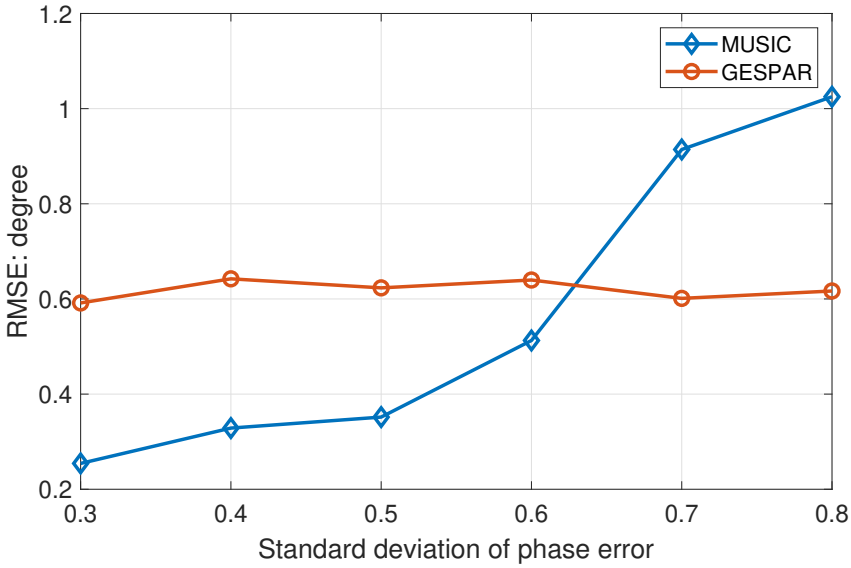

Fig. 2.12 RMSE vs phase error.

The number of sensors M is 20, and DOAs of signals are set as 30° and 60°. The number of snapshots is 20 and the array is assumed to be fully calibrated (i.e. $\mathbf{E} = \mathbf{0}$). Two reference signals are placed at 0° and 5° for the non-coherent method. The inter-sensor spacing d is set as $\lambda/2$, the area of interest is limited within $[0^\circ, 90^\circ]$, and the grid stepsize for the sparsity method is 0.1°. It can be seen that the coherent methods outperform the non-coherent method consistently, as the coherent method utilizes both magnitude and phase information.

Next, the effect of phase errors on coherent and non-coherent DOA methods are evaluated and the result is shown in Fig. 2.12, where the figure displays the RMSE results as a function of the standard deviation of sensor phase errors. The phase error is modelled by a diagonal matrix $\mathbf{E}$, with its entries following the zero-mean Gaussian distribution with standard derivation σ. Due to unreliable phase information when the standard deviation of phase error increases, RMSE of the MUSIC method gets worse than GESPAR which employs magnitude-only measurements.

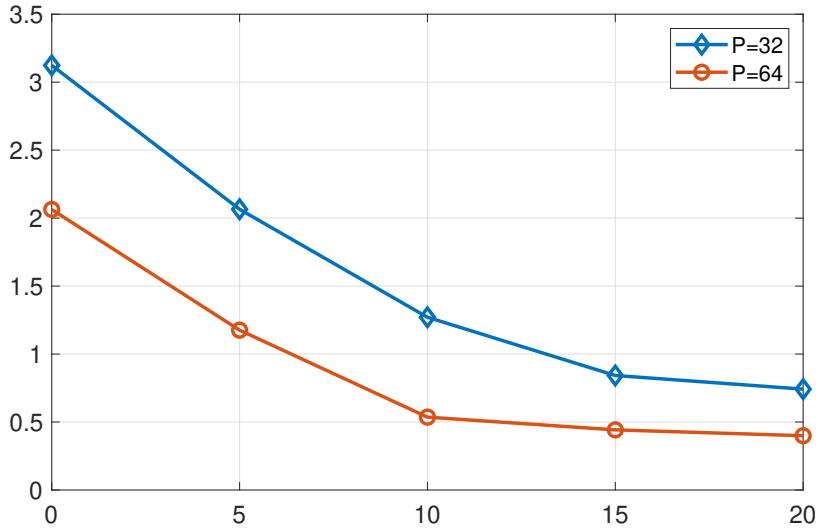

Fig. 2.13 RMSE vs SNR of wideband sources.

RMSE performance of the wideband sources versus SNR is shown in Fig. 2.13. The results are further parameterized by snapshots in time domain. It can be seen that, the wideband method is sensitive to the number snapshots, especially when the nosie level is high.

2.5 Summary

In this chapter, a range of existing methods for DOA estimation of both narrowband and wideband signals have been presented. For narrowband signals, methods including those based on beamforming, subspace and compressive sensing are introduced in detail. In the absence of sensor array phase errors, those methods can provide high resolution results, while their performance declines when phase error exists, which leads to the study of non-coherent DOA estimation, where magnitude-only measurements of the received array signals are available. However, the existing class of non-coherent DOA estimation methods requires reference signals to resolve the inherent ambiguities issue. For wideband signals, as a classic approach, DFT is applied to array signals to transform the wideband model into a narrowband form, and then existing narrowband DOA estimation methods can be applied to find the DOAs. But it is difficult to extend the DFT based approach to the non-coherent scenario and convolutional sparse coding will be introduced at a later stage of this thesis to tackle this problem.

Chapter 3

A Fast Group Sparsity Based Phase Retrieval Algorithm for Non-Coherent DOA Estimation

3.1 Introduction

Compared to existing coherent methods [11–14], the non-coherent methods are unaffected by phase errors at sensors of arrays, but the spatial shift and mirroring ambiguities associated with magnitude-only measurements would make the estimated DOA indistinguishable. Those inherent ambiguities are normally resolved by placing reference signals at one end of interested area in current literature [16–18]. However, in addition to the spatial shift and mirroring ambiguities, another new ambiguity called spatial order ambiguity cannot be solved by reference signals and would affect the DOA results and a solution to avoid this ambiguity is to limit the inter-sensor spacing of the employed ULAs to be less than a quarter of the signal wavelength to deal with the normal DOA range of $[-90^\circ, 90^\circ]$. This is consistent with previous observation that with the standard half-wavelength spacing [16, 18], the DOA range of the signals is limited to either $[0, 90^\circ]$ or $[-90^\circ, 0]$.

Another problem of the phase retrieval based non-coherent DOA estimation is that the traditional phase retrieval solutions originated from optical imaging, astronomy and

crystallography [44–47], where unknown signals in those applications contain only one single snapshot. However, there are normally multiple snapshots at an array of sensors for DOA estimation. As a result, while applying the phase retrieval approach in non-coherent DOA estimation, existing phase retrieval algorithms fail to jointly use the information of multiple snapshots to improve its performance. Although the modified GESPAR [16] extended GRSPAR [40] for multiple snapshots, it still ineffectively processes different snapshots independently.

To deal with the multi-snapshot scenario more effectively, an efficient group sparsity based phase retrieval algorithm based on the phase retrieval via majorizaion-minimization technique (PRIME) [48] and the proximal gradient method [36] is introduced in this chapter for non-coherent DOA estimation. The proposed algorithm is able to utilize multiple snapshots jointly and has a low computational complexity compared to the modified GESPAR. We refer to this algorithm as fasT grOup sparsitY Based phAse Retrieval (ToyBar) [49].

The remaining part of this chapter is structured as follows: The non-coherent signal model and its inherent ambiguities are described in Section 3.2. The proposed group sparsity based phase retrieval algorithm is given in Section 3.3 and simulation results are provided in Section 3.4. Conclusions are drawn in Section 3.5.

3.2 Non-Coherent Signal Model and Ambiguities

The non-coherent measurements of an ULA is given in (2.41), as

$$\mathbf{Y} = |\mathbf{AS}| + \mathbf{N}, \tag{3.1}$$

where $\mathbf{A}$ is the steering matrix of the array.

Two ambiguities associate with magnitude-only measurements would affect DOA results and have been reviewed in Section 2.2.5, which are mirroring and spatial shift. Both mirroring and spatial shift ambiguities can be removed by placing reference signal at either edge of the interested range. If there are more than one incident signals, multiple reference signals may be employed [16].

However, there is another ambiguity which has not been discussed in literature yet and we call it "spatial order ambiguity", as this ambiguity will change the spatial order of the impinging signals, i.e. with $\sin\theta_1 < \sin\theta_2 < \cdots < \sin\theta_K$, we cannot have $\sin\ddot{\theta}_1 < \sin\ddot{\theta}_2 < \cdots < \sin\ddot{\theta}_K$. Next, we discuss it in detail and show that this ambiguity can be avoided by limiting the adjacent sensor spacing to $\lambda/4$.

For this new ambiguity problem, we consider the following ambiguous signals $\check{x}_m[p]$ with the same magnitude as $x_m[p]$, where $\mathbf{x}_m[p]$ denotes the full array measurements of the m-th sensor at p time index, expressed as

$$\begin{aligned}\check{x}_m[p] &= e^{-jm\phi}\sum_{k=1}^{K} s_k[p]e^{-jm2\pi b_k}e^{-jm\frac{2\pi d}{\lambda}\sin\theta_k} \\ &= \sum_{k=1}^{K} s_k[p]e^{-jm\frac{2\pi d}{\lambda}(\sin\theta_k+\frac{\phi\lambda}{2\pi d}+\frac{b_k\lambda}{d})},\end{aligned} \tag{3.2}$$

where b_k is an arbitrary integer. To avoid spatial aliasing, normally we assume $d = \lambda/2$ [20]. Then, (3.2) becomes

$$\check{x}_m[p] = \sum_{k=1}^{K} s_k[p]e^{-jm\frac{2\pi d}{\lambda}(\sin\theta_k+\frac{\phi\lambda}{2\pi d}+2b_k)}. \tag{3.3}$$

Without the b_k term, the maximum value of $\frac{\phi\lambda}{2\pi d}$ which can give a valid shift will be 2, i.e. shifting a signal from -90° to 90°; if it is larger than 2, the new shifted value will be larger than 1, which is not valid for $\sin\theta$, $-90^\circ \le \theta \le 90^\circ$. Similarly, the minimum value for $\frac{\phi\lambda}{2\pi d}$ will be -2 and as a result we would have

$$-2 \le \frac{\phi\lambda}{2\pi d} \le 2. \tag{3.4}$$

Consider the original DOA angles are ordered as $\sin\theta_1 < \sin\theta_2 < ... < \sin\theta_K$ and with a shift by $-2 \le \frac{\phi\lambda}{2\pi d} < 0$, some of the DOA angles, such as $\sin\theta_{k_s}$, $k_s = 1,\cdots,K_s(K_s < K)$ are shifted to the left outside of the valid sinusoidal range so that $\sin\theta_k + \frac{\phi\lambda}{2\pi d} < -1$, for $k \le K_s$, while for the remaining angles, we still have $-1 \le \sin\theta_k + \frac{\phi\lambda}{2\pi d} \le 1$, for $K_s < k \le K$; then, we can choose $b_k = 0$ for $K_s < k \le K$ and $b_k = 1$ for $k \le K_s$. As a result, we would have $-1 \le (\sin\theta_k + \frac{\phi\lambda}{2\pi d} + 2b_k) \le 1$ for $k \le K_s$, which is valid angle values. However, in this case,

we can see that the order of the new set of angles $\ddot{\theta}_k$, satisfying $\sin\ddot{\theta}_k = \sin\theta_k + \frac{\phi\lambda}{2\pi d} + 2b_k$ for all k will be different from the original one, i.e. we will not have $\sin\ddot{\theta}_1 < \sin\ddot{\theta}_2 < \cdots < \sin\ddot{\theta}_K$ any more and the sinusoidal difference of the original signals has changed. The net result is that the first K_s signals are shifted to the right side of the valid angle range, while the remaining signals are shifted to the left.

For example, consider $K = 2$ signals with $\theta_1 = -30^\circ$, $\theta_2 = 90^\circ$ and $\frac{\phi\lambda}{2\pi d} = -2$. After this shift, $\sin\ddot{\theta}_2 = \sin\theta_2 - 2 = -1$ and $\sin\ddot{\theta}_1 = \sin\theta_2 - 2 = -2.5$. Obviously, θ_2 is shifted to -90° and $\ddot{\theta}_1$ does not exist. However, with half wavelength spacing, b_1 can be chosen as 1, which leads to $\sin\ddot{\theta}_1 = \sin\theta_2 - 2 + \frac{\lambda}{d} = -0.5$. As a result, the solution is $\ddot{\theta}_2 = -90^\circ$ and $\ddot{\theta}_1 = -30^\circ$. It can be seen that the order of DOA has changed as $\sin\ddot{\theta}_2 < \sin\ddot{\theta}_1$ as well as the sinusoidal difference (from $\Delta s_{\theta,21} = 1.5$ to $\Delta\ddot{s}_{\theta,21} = 0.5$), but they still share the same magnitude measurement.

We have a similar conclusion if we consider the shift to the left with $0 < \frac{\phi\lambda}{2\pi d} \leq 2$. This ambiguity cannot be solved by adding reference signals as the spacing in sine value among the new set of DOA angles will be different.

However, it can be resolved by reducing inter-sensor spacing d to $d \leq \frac{\lambda}{4}$. In the limit, we choose $d = \frac{\lambda}{4}$. Then

$$\check{x}_m[p] = \sum_{k=1}^{K} s_k[p] e^{-jm\frac{2\pi d}{\lambda}(\sin\theta_k + \frac{\phi\lambda}{2\pi d} + 4b_k)}. \tag{3.5}$$

With $-2 \leq \frac{\phi\lambda}{2\pi d} \leq 2$, for any value of $b_k \neq 0$, we always have

$$|\sin\theta_k + \frac{\phi\lambda}{2\pi d} + 4b_k| > 1, \tag{3.6}$$

which means it is not a valid choice for any physical DOA angle. As a result, we can only have $b_k = 0$, i.e. we have avoided the spatial order ambiguity. Note here, we have assumed $-2 \leq \frac{\phi\lambda}{2\pi d} \leq 2$, but $\frac{\phi\lambda}{2\pi d}$ can take any value outside this range; however, if it does take a value outside this range, it will be reduced to within this range by choosing an appropriate integer value for b_k in $4b_k$.

Therefore, in order to avoid this ambiguity, d is now chosen to be less than or equal to $\lambda/4$ instead of $\lambda/2$ for the normal angle range of interest $[-90^\circ, 90^\circ]$.

3.3 The Proposed Algorithm for Non-Coherent DOA Estimation

The joint group sparsity based non-coherent DOA estimation is reviewed in Chapter 2, and the problem is formulated as

$$\begin{aligned} \min \quad & \|\tilde{\mathbf{S}}\|_{2,0} \\ \text{s.t.} \quad & \|\mathbf{Y} - |\tilde{\mathbf{A}}\tilde{\mathbf{S}}|\|_F^2 < \varepsilon. \end{aligned} \tag{3.7}$$

Since the l_0 norm is noncovex, its relaxed version l_1 norm is employed instead [50], and the resulting estimation problem can be solved by the following unconstrained optimisation problem

$$\min_{\tilde{\mathbf{S}}} \ \||\tilde{\mathbf{A}}\tilde{\mathbf{S}}| - \mathbf{Y}\|_F^2 + \rho\|\tilde{\mathbf{S}}\|_{2,1}, \tag{3.8}$$

where ρ is the regularization parameter, and the $\|\cdot\|_{2,1}$ is $l_{2,1}$ norm, which promotes the row sparsity of $\tilde{\mathbf{S}}$.

Since the phase retrieval problem is a general instance of a non-convex quadratic program, and therefore it is non-convex [51], which results in the optimization problem NP-hard. However, this non-convex problem can be replaced by a surrogate convex function via the majorization-minimization (MM) method. Under the MM framework, a non-increasing property hold as [48, 52]

$$f(\mathbf{s}^{q+1}) \leq g(\mathbf{s}^{q+1}|\mathbf{s}^q) \leq g(\mathbf{s}^q|\mathbf{s}^q) = f(\mathbf{s}^q), \tag{3.9}$$

where $f(\mathbf{s})$ is the original function, q indicates the iteration index and $g(\mathbf{s}|\mathbf{s}^q)$ is the majorization function satisfying

$$\begin{aligned} g(\mathbf{s}|\mathbf{s}^q) &\geq f(\mathbf{s}), \ \ \forall \mathbf{s}, \\ g(\mathbf{s}^q|\mathbf{s}^q) &= f(\mathbf{s}^q). \end{aligned} \tag{3.10}$$

By applying the PRIME technique [48], this phase retrieval problem can be majorized by a surrogate function. Considering the problem (3.8) with one snapshot and dropping the time

index p for convenience, we have

$$\min_{\tilde{\mathbf{s}}} \ \||\tilde{\mathbf{A}}\tilde{\mathbf{s}}| - \mathbf{y}\|_2^2 + \rho\|\tilde{\mathbf{s}}\|_1. \tag{3.11}$$

By following the same approach in [48], the above minimization problem (3.11) can be reformulated as

$$\begin{aligned} &\min_{\tilde{\mathbf{s}}} \sum_{m=1}^{M} (|\tilde{\mathbf{a}}_m\tilde{\mathbf{s}}|^2 - 2y_m|\tilde{\mathbf{a}}_m\tilde{\mathbf{s}}| + |y_m|^2) + \rho\|\tilde{\mathbf{s}}\|_1 \\ &= \min_{\tilde{\mathbf{s}}} \sum_{m=1}^{M} (|\tilde{\mathbf{a}}_m\tilde{\mathbf{s}}|^2 - 2y_m|\tilde{\mathbf{a}}_m\tilde{\mathbf{s}}|) + \rho\|\tilde{\mathbf{s}}\|_1, \end{aligned} \tag{3.12}$$

where $\tilde{\mathbf{a}}_m$ represents the m-th row of the steering matrix $\tilde{\mathbf{A}}$, and y_m is the m-th component of $\mathbf{y}$. According to the Cauchy-Schwarz inequality, it has

$$\mathrm{Re}(\tilde{\mathbf{a}}_i\tilde{\mathbf{s}}(\tilde{\mathbf{s}}^q)^H\tilde{\mathbf{a}}_i^H) \leq |\tilde{\mathbf{a}}_i\tilde{\mathbf{s}}||\tilde{\mathbf{a}}_i\tilde{\mathbf{s}}^q|, \tag{3.13}$$

where $\mathrm{Re}(\cdot)$ represents real part of its variable. Thus, (3.12) can be majorized as

$$\min_{\tilde{\mathbf{s}}} \sum_{m=1}^{M} (|\tilde{\mathbf{a}}_m\tilde{\mathbf{s}}|^2 - 2|y_m|\frac{\mathrm{Re}(\tilde{\mathbf{a}}_m\tilde{\mathbf{s}}(\tilde{\mathbf{s}}^q)^H\mathbf{a}_m^H)}{|\tilde{\mathbf{a}}_m\tilde{\mathbf{s}}^q|}) + \rho\|\tilde{\mathbf{s}}\|_1, \tag{3.14}$$

which can be formulated as

$$\min_{\tilde{\mathbf{s}}} \ \|\tilde{\mathbf{A}}\tilde{\mathbf{s}} - \mathbf{c}^q\|_2^2 + \rho\|\tilde{\mathbf{s}}\|_1, \quad \text{with} \quad \mathbf{c}^q = \mathbf{y} \odot e^{j\arg(\tilde{\mathbf{A}}\tilde{\mathbf{s}}^q)}, \tag{3.15}$$

where $\odot$ denotes the Hadamard product, $\tilde{\mathbf{s}}^q$ is a known complex vector and $\arg(\cdot)$ represents the phase of its variable applied element-wise.

Thus, applying the same approach described in (3.15) column by column to the objective function, the original objective function (3.8) is majorized as

$$\min_{\tilde{\mathbf{S}}} \ \|\tilde{\mathbf{A}}\tilde{\mathbf{S}} - \mathbf{C}^q\|_F^2 + \rho\|\tilde{\mathbf{S}}\|_{2,1}, \tag{3.16}$$

where

$$\mathbf{C}^q = \mathbf{Y} \odot e^{j\arg(\tilde{\mathbf{A}}\tilde{\mathbf{S}}^q)}. \tag{3.17}$$

Since (3.16) is convex, it can be solved by the proximal gradient method [36, 53], which aims at solving problems in the form of

$$\min_{\tilde{\mathbf{S}}} F(\tilde{\mathbf{S}}) + G(\tilde{\mathbf{S}}), \tag{3.18}$$

where both $F(\tilde{\mathbf{S}})$ and $G(\tilde{\mathbf{S}})$ are convex and $F(\tilde{\mathbf{S}})$ is differentiable. Then, this method iteratively refines its solution by

$$\tilde{\mathbf{S}}^{q+1} = \mathbf{prox}_{\lambda G}(\tilde{\mathbf{S}}^q - \lambda \nabla F(\tilde{\mathbf{S}}^q)), \tag{3.19}$$

where λ is the stepsize and $\nabla F(\tilde{\mathbf{S}}^q)$ is the gradient of $F(\tilde{\mathbf{S}})$. The proximal operator **prox** is defined as

$$\mathbf{prox}_{\lambda G}(\tilde{\mathbf{S}}) = \underset{\mathbf{Z}}{\operatorname{argmin}}(\frac{1}{2\lambda}\|\mathbf{Z} - \tilde{\mathbf{S}}\|_F^2 + G(\mathbf{Z})). \tag{3.20}$$

Therefore, substituting the first term of object function (3.8) as $F(\tilde{\mathbf{S}})$ and second term as $G(\tilde{\mathbf{S}})$, $\tilde{\mathbf{S}}^{q+1}$ can be obtained by solving the following problem

$$\tilde{\mathbf{S}}^{q+1} = \underset{\mathbf{Z}}{\operatorname{argmin}}\{\|\frac{1}{2\lambda}\|\mathbf{Z} - (\tilde{\mathbf{S}}^q - \lambda \nabla F(\tilde{\mathbf{S}}^q))\|_F^2 + \rho\|\mathbf{Z}\|_{2,1}\}. \tag{3.21}$$

Since $G(\tilde{\mathbf{S}}) = \|\cdot\|_{2,1}$ is separable as $\|\tilde{\mathbf{S}}\|_{2,1} = \sum_{i=1}^{G}\|\tilde{\mathbf{s}}_i\|_2$, where $\tilde{\mathbf{s}}_i$ represents the i-th row of $\tilde{\mathbf{S}}$, the proximal operator can be applied to each row independently as [36], [54]

$$\tilde{\mathbf{s}}_i^{q+1} = \underset{\mathbf{z}_i}{\operatorname{argmin}}\{\rho\|\mathbf{z}_i\|_2 + \frac{1}{2\lambda}\|\mathbf{z}_i - (\tilde{\mathbf{s}}_i^q - \lambda \nabla F(\tilde{\mathbf{s}}_i^q))\|_2^2\}, \tag{3.22}$$

where $\mathbf{z}_i$ is the i-th row of $\mathbf{Z}$, with

$$\nabla F(\tilde{\mathbf{s}}_i^q) = 2(\tilde{\mathbf{A}}^H)_i(\tilde{\mathbf{A}}\tilde{\mathbf{S}}^q - \mathbf{C}^q),\ i = 1, \cdots, G, \tag{3.23}$$

is the i-th row of $\nabla F(\tilde{\mathbf{S}}^q)$, and $(\tilde{\mathbf{A}}^H)_i$ is the i-th row of $\tilde{\mathbf{A}}^H$. This is equivalent to applying the row-wise proximal operator of l_2 norm to (3.21), which has an analytical solution as [54]

$$\tilde{\mathbf{s}}_i^{q+1} = (\tilde{\mathbf{s}}_i^q - \lambda \nabla F(\tilde{\mathbf{s}}_i^q)) \max(1 - \frac{\rho\lambda}{\|\tilde{\mathbf{s}}_i^q - \lambda \nabla F(\tilde{\mathbf{s}}_i^q)\|_2}, 0). \tag{3.24}$$

The positions of non-zero rows of the reconstructed signal matrix $\tilde{\mathbf{S}}^q$ correspond to DOAs of incident signals.

3.3.1 Convergence Analysis

The non-convex group sparse phase retrieval problem is replaced by a convex surrogate via the majorization-minimization technique. If the second inequality of (3.9) holds, we have

$$\|\tilde{\mathbf{A}}\tilde{\mathbf{S}}^{q+1} - \mathbf{C}^{q+1}\|_F^2 + \rho\|\tilde{\mathbf{S}}^{q+1}\|_{2,1} \leq \|\tilde{\mathbf{A}}\tilde{\mathbf{S}^q} - \mathbf{C}^q\|_F^2 + \rho\|\tilde{\mathbf{S}}^q\|_{2,1}, \tag{3.25}$$

and thus the generated sequence $\tilde{\mathbf{S}^q}$ will at least converge to a stationary point.

Following the convergence analysis of the proximal gradient method in [55], [56], next we give an analysis of the derived algorithm.

Consider the general model (3.16), $F(\mathbf{S}) = \|\tilde{\mathbf{A}}\tilde{\mathbf{S}} - \mathbf{C}^q\|_F^2$ and $G(\tilde{\mathbf{S}}) = \rho\|\tilde{\mathbf{S}}\|_{2,1}$. The smallest Lipschitz constant of $F(\mathbf{S})$ is the Hessian of it, which is equal to $L = 2\lambda_{max}(\mathbf{A}^H\mathbf{A})$, where $\lambda_{max}(\cdot)$ extracts the maximum eigenvalue of its variable. Thus, if $\lambda \leq \frac{1}{L}$, for any $\tilde{\mathbf{S}}^q$, $F(\tilde{\mathbf{S}}^{q+1})$ is upper bounded by [56],

$$\begin{aligned} F(\tilde{\mathbf{S}}^{q+1}) \leq F(\tilde{\mathbf{S}}^q) + \mathrm{Re}(< \nabla F(\tilde{\mathbf{S}}^q), \tilde{\mathbf{S}}^{q+1} - \tilde{\mathbf{S}}^q >) \\ + \frac{1}{2\lambda}\|\tilde{\mathbf{S}}^{q+1} - \tilde{\mathbf{S}}^q\|_F^2, \end{aligned} \tag{3.26}$$

where $< \cdot, \cdot >$ represents Frobenius inner product and $\mathrm{Re}(\cdot)$ represents real part of its variable. Since the $l_{2,1}$ norm is also convex, for $\tilde{\mathbf{S}}^q$, there should be a subgradient $\mathbf{V} \in \partial\|\tilde{\mathbf{S}}^{q+1}\|_{2,1}$, which satisfies

$$G(\tilde{\mathbf{S}}^{q+1}) \leq G(\tilde{\mathbf{S}}) - \mathrm{Re}(< \mathbf{V}, \tilde{\mathbf{S}} - \tilde{\mathbf{S}}^{q+1} >). \tag{3.27}$$

Therefore, using (3.26) and (3.27), the upper bound of the objective function (3.16) is given by

$$\begin{aligned} F(\tilde{\mathbf{S}}^{q+1}) + G(\tilde{\mathbf{S}}^{q+1}) \leq F(\tilde{\mathbf{S}}^{q}) + G(\tilde{\mathbf{S}}^{q}) - \mathrm{Re}(< \mathbf{V}, \tilde{\mathbf{S}}^{q} - \tilde{\mathbf{S}}^{q+1} >) \\ + \mathrm{Re}(< \nabla F(\tilde{\mathbf{S}}^{q}), \tilde{\mathbf{S}}^{q} - \tilde{\mathbf{S}}^{q+1} >) + \frac{1}{2\lambda} \|\tilde{\mathbf{S}}^{q+1} - \tilde{\mathbf{S}}^{q}\|_F^2. \end{aligned} \tag{3.28}$$

The sequence $\tilde{\mathbf{S}}^{q}$ is generated by the proximal gradient method, which can be written as

$$\begin{aligned} \tilde{\mathbf{S}}^{q+1} &= \mathbf{prox}_{\lambda g}(\tilde{\mathbf{S}}^{q} - \lambda \nabla F(\tilde{\mathbf{S}}^{q})) \\ &= \underset{\mathbf{Z}}{\mathrm{argmin}} (G(\mathbf{Z}) + \frac{1}{2\lambda} \|\mathbf{Z} - (\tilde{\mathbf{S}}^{q} - \lambda \nabla F(\tilde{\mathbf{S}}^{q})\|_F^2) \\ &= \underset{\mathbf{Z}}{\mathrm{argmin}} (G(\mathbf{Z}) + F(\tilde{\mathbf{S}}^{q}) + < \nabla F(\tilde{\mathbf{S}}^{q}), \mathbf{Z} - \tilde{\mathbf{S}}^{q} > \\ &+ \frac{1}{2\lambda} \|\mathbf{Z} - \tilde{\mathbf{S}}^{q}\|_F^2). \end{aligned} \tag{3.29}$$

The last equality is obtained by ignoring constant terms unrelated to $\mathbf{Z}$.

With the optimal condition of (3.29), if $\tilde{\mathbf{S}}^{q+1}$ exists, its subgradient $\mathbf{V} \in \partial \|\tilde{\mathbf{S}}^{q+1}\|_{2,1}$ should satisfy

$$\mathbf{V} + \frac{1}{\lambda}(\tilde{\mathbf{S}}^{q+1} - \tilde{\mathbf{S}}^{q}) + \nabla F(\tilde{\mathbf{S}}^{q}) = \mathbf{0}. \tag{3.30}$$

Thus, by substituting (3.30) into (3.28), one has

$$F(\tilde{\mathbf{S}}^{q}) + G(\tilde{\mathbf{S}}^{q}) - F(\tilde{\mathbf{S}}^{q+1}) - G(\tilde{\mathbf{S}}^{q+1}) \geq \frac{1}{2\lambda} \|\tilde{\mathbf{S}}^{q} - \tilde{\mathbf{S}}^{q+1}\|_F^2. \tag{3.31}$$

Therefore, the sequence $\tilde{\mathbf{S}}^{q}$ produced by the proximal gradient method is guaranteed to converge with stepsize $\lambda \leq \frac{1}{L}$.

3.3.2 Acceleration Scheme

Since the group sparse phase retrieval problem is transformed into a convex surrogate and solved by the proximal gradient method, it can be further accelerated by applying the Nesterov acceleration [55, 57]. This method does not apply proximal operator to previous

Table 3.1 Algorithm Summary (ToyBar)

Input: $\tilde{\mathbf{A}}$, $\mathbf{Y}$, ρ, λ,
Output: $\tilde{\mathbf{S}}$ (reconstructed signal).
Initialization: Set $\tilde{\mathbf{S}}^0$ as a random matrix, $\mathbf{B}^0 = \tilde{\mathbf{S}}^0$, $\beta^0 = 1$.
General steps: for q=0, ..., Q
1) Calculate $\mathbf{C}^q = \mathbf{Y} \odot e^{j\arg(\tilde{\mathbf{A}}\mathbf{B}^q)}$
2) Calculate $\tilde{\mathbf{S}}^{q+1}$, for i=1,...,G
Gradient:$\nabla F(\tilde{\mathbf{b}}_i^q) = 2(\tilde{\mathbf{A}}^H)_i(\tilde{\mathbf{A}}\mathbf{B}^q - \mathbf{C}^q)$,
Find $\tilde{\mathbf{s}}_i^{q+1}$ as
$\tilde{\mathbf{s}}_i^{q+1} = (\mathbf{b}_i^q - \lambda\nabla F(\mathbf{b}_i^q))\max(1 - \frac{\rho\lambda}{\|\mathbf{b}_i^q - \lambda\nabla F(\mathbf{b}_i^q)\|_2}, 0)$,
where $\mathbf{b}_i^q$ is the i-th row of $\mathbf{B}^q$.
3) **Update**: $\beta^{q+1} = \frac{1+\sqrt{1+4(\beta^q)^2}}{2}$,
$\mathbf{B}^{q+1} = \tilde{\mathbf{S}}^{q+1} + \frac{\beta^q - 1}{\beta^{q+1}}(\tilde{\mathbf{S}}^{q+1} - \tilde{\mathbf{S}}^q)$.

$\tilde{\mathbf{S}}^{q+1}$ directly, but another point $\mathbf{B}^{q+1}$ based on $\tilde{\mathbf{S}}^{q+1}$ and $\tilde{\mathbf{S}}^q$ expressed as

$$\mathbf{B}^{q+1} = \tilde{\mathbf{S}}^{q+1} + \frac{\beta^q - 1}{\beta^{q+1}}(\tilde{\mathbf{S}}^{q+1} - \tilde{\mathbf{S}}^q), \tag{3.32}$$

where

$$\beta^{q+1} = \frac{1 + \sqrt{1 + 4(\beta^q)^2}}{2}. \tag{3.33}$$

The full algorithm is presented in the above Algorithm Summary, which is referred to as fasT grOup sparsitY Based phAse Retrieval (ToyBar).

3.3.3 Maximum Number of Resolvable Signals

Traditionally, for a M-sensor ULA, at most $K = M - 1$ impinging signals can be resolved. However, due to lack of phase information, from the viewpoint of phase retrieval, only less than $M - 1$ signals can be constructed with M measurements. In [58], it proves that for full sparse signals ($K = G$), at most $G = 2M - 1$ signals can be recovered with the generic measurement frame $\mathbf{A} = \{\mathbf{a}_m\}_{m=1}^M$ if both the measurement matrix and signals are real-valued, where $\mathbf{a}_m$ is the m-th row of $\mathbf{A}$ and by generic it means $\mathbf{A}$ is an open dense subset of $\mathbb{R}(\mathbb{C})$ i.e.

random Gaussian matrix. For the complex-valued scenario, [59] conjectures that $M = 4G-4$ generic measurements is required to recover G signals. This conjecture has been proved in [60] for $G = 2^b - 1, b \geq 1$. For K-sparse signals, $4K-1$ ($8K-2$) generic measurements are needed for real (complex) scenarios [61].

Since the steering matrix is not generic, the above condition might not hold for the non-coherent measurements of an array. The authors in [62] show that $K^2 - K + 1$ measurements are required to recover K signals with Fourier magnitude measurements by pointing out that reconstructing K-sparse signals from its magnitude measurements is the same as recovering its auto-correlation from its Fourier measurements [62]. As the steering matrix has a similar structure to the Fourier measurements matrix, similar theorem can be derived.

Theorem 3.3.1. *To reconstruct a K-sparse signals $\mathbf{s}$, at least $K^2 - K + 1$ measurements are necessary.*

Proof. Defining a vector $\mathbf{u}$ as

$$\mathbf{u} = \left[|\mathbf{s}|^2, \mathbf{s}_{1,K}, ..., \mathbf{s}_{K-1,K}, \mathbf{s}^*_{K-1,K}, ..., \mathbf{s}^*_{1,K}\right]^T, \tag{3.34}$$

where $\mathbf{s}_{k,K} = [s_k s^*_{k+1}, s_k s^*_{k+2} ..., s_k s^*_K]$ for $k = 1, ..., K-1$, and $|\mathbf{s}|^2 = \sum_{k=1}^K |s_k|^2$.

Then, we can find a matrix $\mathbf{D}$ satisfying

$$|\tilde{\mathbf{A}}\tilde{\mathbf{s}}|^2 = \mathbf{D}\mathbf{u}, \tag{3.35}$$

□

with

$$\mathbf{d}_m^T = \begin{bmatrix} 1 \\ e^{-jm\frac{2\pi d}{\lambda}\Delta\sin\boldsymbol{\theta}_{1K}} \\ \vdots \\ e^{-jm\frac{2\pi d}{\lambda}\Delta\sin\boldsymbol{\theta}_{K-1,K}} \\ e^{jm\frac{2\pi d}{\lambda}\Delta\sin\boldsymbol{\theta}_{K-1,K}} \\ \vdots \\ e^{jm\frac{2\pi d}{\lambda}\Delta\sin\boldsymbol{\theta}_{1K}} \end{bmatrix}, \tag{3.36}$$

where $\Delta\sin\boldsymbol{\theta}_{k,K} = [\sin\theta_k - \sin\theta_{k+1}, ..., \sin\theta_k - \sin\theta_K]$. Therefore, recovering $\tilde{\mathbf{s}}$ from its magnitude measurements is equivalent to reconstructing sparse signal $\mathbf{u}$ with overcomplete dictionary $\mathbf{D}$. For an M-element array, it can recover up to K signals, with K satisfying $K^2 - K + 1 \leq M$. Note that, the number of signals that can be resolved with magnitude measurements is still an open question, and the above result is not a tight bound and only used as a reference.

3.4 Simulations

In this section, several simulations are provided to show the performance of the proposed ToyBar with ULA. Without loss of generality, the inter-sensor distance d is $\lambda/4$ for avoiding the spatial ordering ambiguity and two reference signals with DOA $\{-90^\circ,\ -85^\circ\}$ are applied for avoiding spatial shift and mirroring ambiguities. The steering matrix is formed with a grid stepsize of 0.5° and performance of the modified GESPAR [16] is compared with the proposed ToyBar. The maximum iteration number of the modified GESPAR is set as 64000 in the following simulations, while for the ToyBar, the iteration number is 500, and 30 random initializations are used in order to find the global minimum of the non-convex problem. The stepsize used in Toybar is set as $1/(2\lambda_{max}(\tilde{\mathbf{A}}^H\tilde{\mathbf{A}}))$, where $\lambda_{max}(\cdot)$ is the maximum eigenvalue of its variable. Since the modified GESPAR is designed for magnitude square of the measurements, the data used for GESPAR is $(|\tilde{\mathbf{A}}\tilde{\mathbf{S}}| + \mathbf{N})^2$.

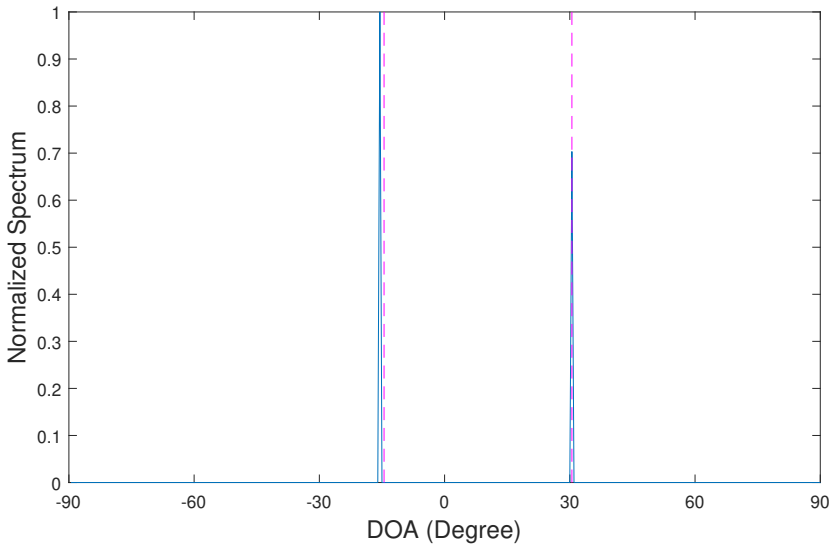

Fig. 3.1 Estimation results by the proposed ToyBar.

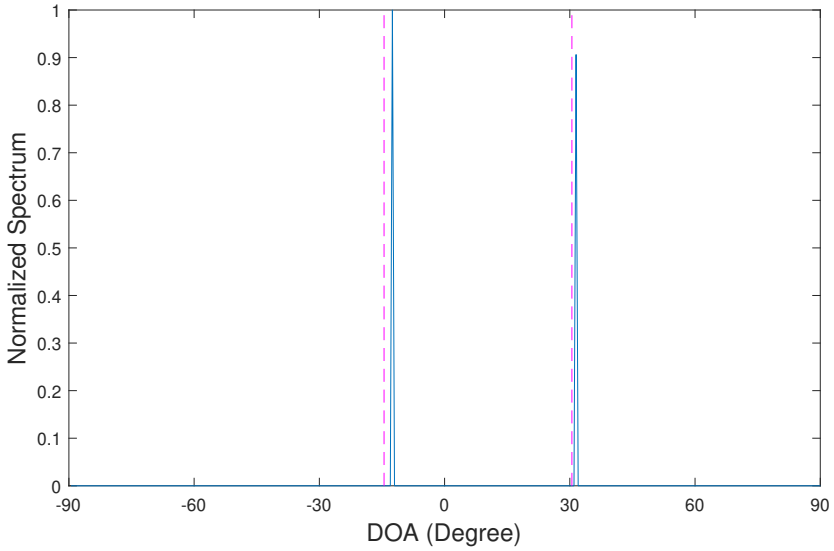

Fig. 3.2 Estimation results by the modified GESPAR.

The first simulation shows the obtained spatial spectrum of the modified GESPAR and ToyBar with SNR=15 dB while applying a $M = 20$ ULA, where the dotted lines are true DOA and solid lines are estimation results. There are $K = 2$ incident signals from $\{-15^\circ, 30^\circ\}$. As shown in Figs. 3.1 and 3.2, both methods have obtained a good estimation of the true DOAs of incident signals.

To further compare the accuracy of both algorithms, Fig. 3.3 shows the root mean square error (RMSE) of the DOA estimation results as a function of SNR over 100 trials. It can be observed that the proposed ToyBar consistently outperforms the modified GESAPR. For SNR$\geq$ 15, increasing SNR has a rather limited effect on performance.

In Fig. 3.4, results of RMSE versus the number of snapshots of both algorithms are provided. SNR is fixed at 25 dB but the number of snapshots P is from 20 to 100. Each point is averaged over 50 trials. Under all snapshot settings, the proposed algorithm has a lower RMSE than the modified GESPAR.

The fourth simulation studies the RMSE results versus the number of impinging signals K, as presented in Fig. 3.5, where only the proposed ToyBar is employed with $M = 20$ and $M = 30$ sensors. The SNR is set to 20 dB, $P = 40$ snapshots are collected and four reference signals are employed. It can be observed that, the number of signals can be recovered is less than the coherent scenario with full measurements ($K = M - 1$), but it exceeds the bounds derived in section 3.3. One possible reason is that the aim of DOA estimation is recovering the correct support of sparse signals, not exact values of signals. However, the real bound for support recovery is still an open problem, and should be further investigated.

Finally, to compare the computational complexity of the modified GESPAR and the proposed ToyBar, the average running time of both algorithms under CPU I5 5200U at 2.2GHz and 4 GB RAM is listed in Table 3.2. It can be seen that a larger number of snapshots significantly increases the running time of GESPAR and it always requires much longer running time than the proposed ToyBar. There are two possible reasons. One is that GESPAR is a greedy algorithm and requires more iterations to achieve a good performance; the other one is that, it was originally designed for the traditional phase retrieval problem, which always assumes that the input signal has one snapshot only, and thus its modified version

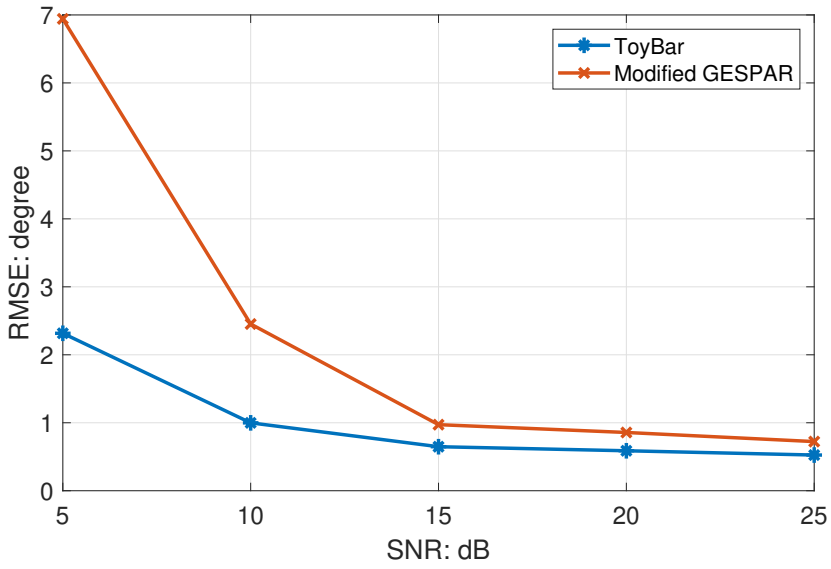

Fig. 3.3 RMSE vs SNR.

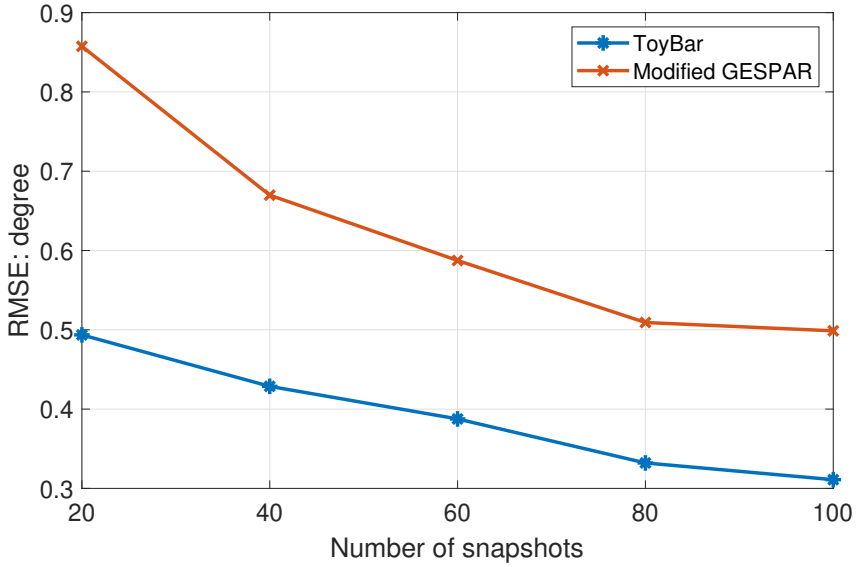

Fig. 3.4 RMSE vs number of snapshots.

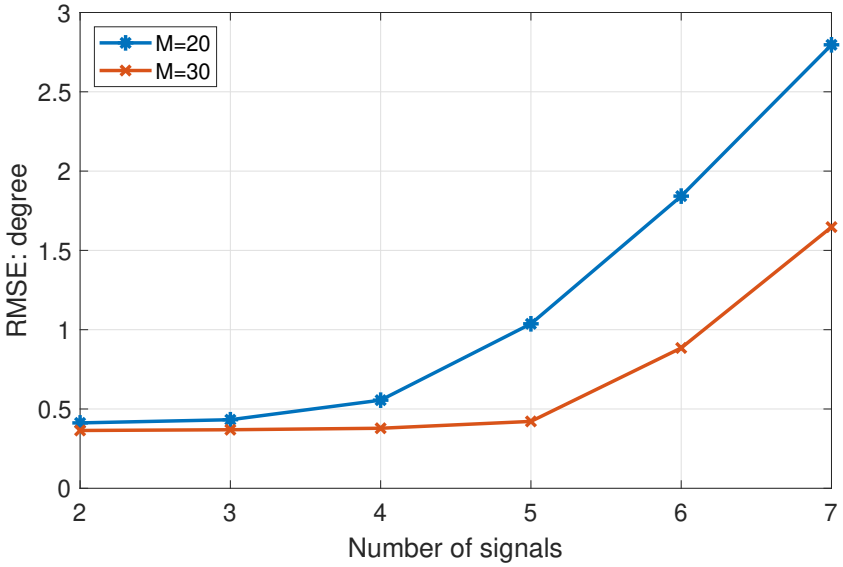

Fig. 3.5 RMSEvsK

for multiple snapshots has to exploit different time samples separately. By contrast, the proposed algorithm exploits multiple data samples directly through group sparsity, which is more efficient than the modified GESPAR.

Table 3.2 Running times of different algorithms.

Snapshots	Modified GESPAR(s)	ToyBar(s)
P=20	950.48	26.10
P=60	2251.32	33.15
P=100	3998.16	39.43

3.5 Conclusions

In this paper, the non-coherent DOA estimation problem has been studied and an efficient and effective sparse phase retrieval algorithm for multiple snapshots called ToyBar was proposed. The problem was first formulated as a group sparse phase retrieval problem, which was then solved by the proximal gradient method after transforming the original non-convex problem into its convex surrogate via majorization-minimization. Ambiguities associated with the magnitude-only measurements of ULAs are avoided by applying reference signals and limiting inter-sensor spacing to $\lambda/4$. As demonstrated by simulations, the proposed

algorithm ToyBar has a better performance in terms of both computational complexity and estimation accuracy.

Chapter 4

Non-Coherent DOA Estimation without Reference Signals by Different Array Structures

4.1 Introduction

As discussed earlier, non-coherent DOA estimation based on the ULA structure requires the assistance of one or more reference signals with precisely known DOA in advance to resolve the ambiguities problem among non-coherent measurements. In [16], the inherent ambiguity issue was resolved by placing a reference signal at a lower angle when only one unknown source impinges upon the array and more reference signals are needed when more unknown impinging signals are present. In order to estimate the DOA of multiple signals with one reference signal, [17–19] proposed to employ a high gain reference signal (power of reference signal is 12 dB over than unknown signals). Alternatively, the authors in [17] also suggested that, with the aid of measurements by another array deployed with a different orientation to the first array, one reference signal is capable of resolving the ambiguities for multiple incident signals. By assuming a large gain reference signal, the Cramer-Rao Bound (CRB) of non-coherent DOA estimation for one unknown incident signal was presented in

[63, 64]. However, applying reference signal is a challenge in practical array operation and cannot always be guaranteed [65, 66].

In this chapter, two array structure are suggested to solve the inherent ambiguities problem. The first is a dual-array structure, which consists of two ULAs with an offset between them. In essence, it utilizes the non-linear property of the sinusoidal function, and unique DOA estimation results are guaranteed with two sets of sinusodial differences. Based on the proposed dual-array structure, two non-coherent DOA estimation methods are proposed without reference signals. Instead of using ULAs, uniform circular arrays (UCAs) is then proposed as another solution to overcome the ambiguities arising in non-coherent measurements, as analysed in detail. With these two array structures, non-coherent DOA estimation can be resolved without the requirement of reference signals in multiple impinging sources scenarios; one reference signal is still required in the scenario with only one incident signal, but the DOA of the reference signal can be arbitrary and unknown.

The remaining part of this chapter is structured as follows. Section 4.2 introduces the signal model of the dual-array structure and ambiguities followed by two proposed non-coherent DOA estimation methods and simulation results of the dual-array structure. The analysis of UCA for non-coherent DOA estimation is displayed in Section 4.3, along with simulation results. Conclusions are drawn in Sec. 4.4.

4.2 The Dual-Array Structure

4.2.1 Signal Model

The proposed array structure consists of two ULAs with an adjacent sensor spacing d as shown in Fig. 4.1. The first array is in the horizontal direction while the second has a known angle $\breve{\theta}$ to the first. The area of interest $[-90^\circ, 90^\circ]$ is considered with respect to the broadside of each array. The number of sensors of the first array is M_1 while the second is M_2 and one sensor is shared. Thus, there are $M_1 + M_2 - 1$ sensors in total.

Assume that there are K narrowband signals s_k with the same wavelength λ impinging from directions θ_k, $k = 1, 2, ..., K$, respectively. The signal model of ULA has been reviewed

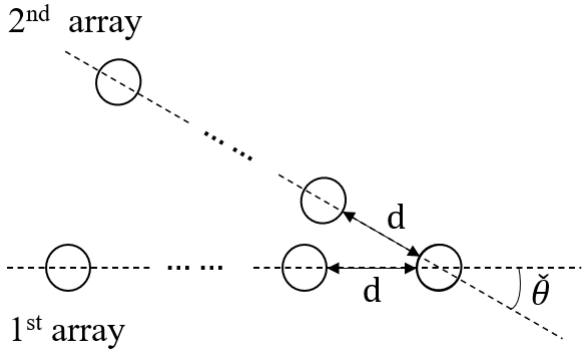

Fig. 4.1 The dual-array structure with a shared sensor.

in Section 2.2, and the signal received by the dual-array structure is then given by

$$\begin{aligned} \mathbf{Y}_1 &= |\mathbf{A}_1\mathbf{S}| + \mathbf{N}_1, \\ \mathbf{Y}_2 &= |\mathbf{A}_2\mathbf{S}| + \mathbf{N}_2, \end{aligned} \tag{4.1}$$

where $\mathbf{Y}_1$ and $\mathbf{Y}_2$ are measurements at the first and second sub-arrays separately, while $\mathbf{N}_1$ and $\mathbf{N}_2$ are white Gaussian noise. $\mathbf{S}$ is the source signal matirx contains P columns, represents P collected snapshots, expressed as

$$\mathbf{s}[p] = [s_1[p], s_2[p], .., s_K[p]]^T. \tag{4.2}$$

$\mathbf{A}_1(\theta)$ and $\mathbf{A}_2(\theta)$ are steering matrices with respect to the first and second arrays separately, given by

$$\begin{aligned} \mathbf{A}_1 &= [\mathbf{a}(\theta_{1,1}), ..., \mathbf{a}(\theta_{K,1})], \\ \mathbf{A}_2 &= [\mathbf{a}(\theta_{1,2}), ..., \mathbf{a}(\theta_{K,2})], \end{aligned} \tag{4.3}$$

with their columns, $\mathbf{a}_1(\theta_{k,1})$ and $\mathbf{a}_2(\theta_{k,2})$, for $k = 1, ..., K$, being the corresponding steering vectors, expressed as

$$\begin{aligned} \mathbf{a}(\theta_{k,1}) &= [1, e^{-j2\pi\frac{d}{\lambda}\sin(\theta_{k,1})}, ..., e^{-j(M_1-1)2\pi\frac{d}{\lambda}\sin(\theta_{k,1})}]^T, \\ \mathbf{a}(\theta_{k,2}) &= [1, e^{-j2\pi\frac{d}{\lambda}(\sin(\theta_{k,2})}, ..., e^{-j(M_2-1)2\pi\frac{d}{\lambda}\sin(\theta_{k,2})}]^T, \end{aligned} \tag{4.4}$$

where $\theta_{k,1}$ and $\theta_{k,2}$ are arriving angle of the k-th signal with respect to the broadside of the first and second arrays, respectively.

4.2.2 Non-coherent DOA Estimation with Dual Array

In this sub-section, based on the dual-array structure, two methods for non-coherent DOA estimation without reference siganls are presented. The first method estimates the set of ambiguous DOAs relative to each subarray, which also shows that the dual-array structure is capable of solving the inherent shift and mirroring ambiguities without the aid of reference signals. Then, a more effective joint group sparsity based DOA estimation method is proposed.

4.2.2.1 Separate Estimation Method

With the specific array structure, the area to be estimated for the first array $\boldsymbol{\theta}_1$ is set as

$$\boldsymbol{\theta}_1 \in [-90^\circ + \breve{\theta}, 90^\circ], \tag{4.5}$$

while for the second array, it is

$$\boldsymbol{\theta}_2 \in [-90^\circ, 90^\circ - \breve{\theta}]. \tag{4.6}$$

This is the common angle range of interest of both arrays, which is then uniformly divided into G ($G \gg K$) grid points. Then, two corresponding overcomplete steering matrices $\tilde{\mathbf{A}}_1$ and $\tilde{\mathbf{A}}_2$ are constructed with each column representing a steering vector of a potential incident angle

$$\begin{aligned} \tilde{\mathbf{A}}_1 &= [\mathbf{a}(-90^\circ + \breve{\theta}), ..., \mathbf{a}(90^\circ)], \\ \tilde{\mathbf{A}}_2 &= [\mathbf{a}(-90^\circ), ..., \mathbf{a}(90^\circ - \breve{\theta})]. \end{aligned} \tag{4.7}$$

Accordingly, the signal vector $\mathbf{s}[p]$ is replaced by two $G \times 1$ sparse vectors, given by

$$\begin{aligned} \tilde{\mathbf{s}}_1[p] &= [s_{1,1}[p], \cdots, s_{G,1}[p]]^T, \\ \tilde{\mathbf{s}}_2[p] &= [s_{1,2}[p], \cdots, s_{G,2}[p]]^T, \end{aligned} \tag{4.8}$$

where only K entries at the corresponding incident angles are supposed to be non-zero. For the multiple-snapshot case, measurements of both arrays are expressed as $\mathbf{Y}_1 = [\mathbf{y}_1[0], \cdots, \mathbf{y}_1[P-1]]$ and $\mathbf{Y}_2 = [\mathbf{y}_2[0], \cdots, \mathbf{y}_2[P-1]]$, where P is the number of snapshots. Signal matrices with respect to the two sub-arrays are defined separately as

$$\begin{aligned} \tilde{\mathbf{S}}_1 &= [\tilde{\mathbf{s}}_1[0], \cdots, \tilde{\mathbf{s}}_1[P-1]], \\ \tilde{\mathbf{S}}_2 &= [\tilde{\mathbf{s}}_2[0], \cdots, \tilde{\mathbf{s}}_2[P-1]]. \end{aligned} \tag{4.9}$$

These signals can be reconstructed separately following a sparse phase retrieval minimization problem,

$$\begin{aligned} &\min_{\tilde{\mathbf{S}}_1} \|\mathbf{Y}_1^2 - |\tilde{\mathbf{A}}_1 \tilde{\mathbf{S}}_1|^2\|_F^2, \;\; s.t. \; \|\tilde{\mathbf{S}}_1\|_{2,0} \leq K, \\ &\min_{\tilde{\mathbf{S}}_2} \|\mathbf{Y}_2^2 - |\tilde{\mathbf{A}}_2 \tilde{\mathbf{S}}_2|^2\|_F^2, \;\; s.t. \; \|\tilde{\mathbf{S}}_2\|_{2,0} \leq K, \end{aligned} \tag{4.10}$$

where K, $\|\cdot\|_{2,0}$ and $\|\cdot\|_F$ represent the number of incident signals, $l_{2,0}$ norm and Frobenius norm, respectively.

However, the reconstructed signals suffer from ambiguities as described in Section 2.2.5 and true DOAs cannot be found directly by solving the problem. Instead, only the sinusoidal difference of all impinging signals of the first sub-array and the second sub-array, defined as

$$\begin{aligned} \Delta s_{\theta,kk',1} &= \sin\theta_{k,1} - \sin\theta_{k',1} \\ \Delta s_{\theta,kk',2} &= \sin\theta_{k,2} - \sin\theta_{k',2}. \end{aligned} \tag{4.11}$$

are estimated. It is noted that, any ambiguity would not affect the sinusoidal distance $\Delta s_{\theta,max}$ between the smallest and largest angles of reconstructed signals in the presence of ambiguities.

Moreover, by assuming $\sin\theta_1 < \sin\theta_2 < \cdots < \sin\theta_K$, the sinusoidal differences between smallest and largest DOA of incident signals impinging on the first and second arrays, $\Delta s_{\theta,max,1}$ and $\Delta s_{\theta,max,2}$, have the following relationship with the four real DOA angles $\theta_{K,1}$, $\theta_{1,1}$, $\theta_{K,2}$, $\theta_{1,2}$,

$$\begin{aligned} \Delta s_{\theta,max,1} &= \sin(\theta_{K,1}) - \sin(\theta_{1,1}), \\ \Delta s_{\theta,max,2} &= \sin(\theta_{K,2}) - \sin(\theta_{1,2}). \end{aligned} \tag{4.12}$$

One condition for the above equations is that angle range of the signals of interest of the first array should be limited between $-90^\circ + \check{\theta}$ and 90°. Given $\check{\theta}$, we also have

$$\begin{aligned} \theta_{K,2} &= \theta_{K,1} - \check{\theta} \\ \theta_{1.2} &= \theta_{1,1} - \check{\theta}, \end{aligned} \tag{4.13}$$

where $\sin\theta_1 < \sin\theta_2 < \cdots \sin\theta_K$. From (4.12) and (4.13), we have

$$\cos(\theta_{K,1}) - \cos(\theta_{1,1}) = (\Delta s_{\theta,max,1} - \frac{(\Delta s_{\theta,max,2})}{cos\check{\theta}})/\tan\check{\theta} \tag{4.14}$$

Using trigonometric identities, from (4.12) and (4.14), the sum of the smallest and largest angles $\theta_S = \theta_{1,1} + \theta_{K,1}$ is given by

$$\theta_S = 2\text{atan}\frac{\frac{\Delta s_{\theta,max,2}}{\cos\check{\theta}} - (\Delta s_{\theta,max,1})}{(\Delta s_{\theta,max,1}\tan\check{\theta})}. \tag{4.15}$$

The largest angle θ_K is then derived from (4.12) and (4.15) as

$$\sin(\frac{2\theta_{K,1} - \theta_S}{2}) = \frac{\Delta s_{\theta,max,1}}{2\cos(\theta_S/2)}. \tag{4.16}$$

By (4.15) and (4.16), we obtain

$$\begin{aligned} \theta_{K,1} &= \text{asin}(\frac{\Delta s_{\theta,max,1}}{2\cos(\theta_S/2)}) + \frac{\theta_S}{2}, \\ \theta_{1,1} &= \theta_S - \theta_{K,1}. \end{aligned} \tag{4.17}$$

However, even with the smallest and largest angles unambiguously known, the remaining $K-2$ estimation results still suffer from the mirroring ambiguity, which means $\Delta s_{\theta,1k}$ could represent either $\sin\theta_k - \sin\theta_1$ or $\sin\theta_K - \sin\theta_k$.

As a result, with the different sinusoidal distance $\Delta s_{\theta,1,k1}$ between $\theta_{1,1}$ and $\theta_{k,1}, k = 2,...,K-1$, there are two possible solutions: the true DOAs and its mirroring versions, given by

$$\begin{aligned} \theta_{k,1} &= \text{asin}(\Delta s_{\theta,1,1k} + \sin(\theta_{1,1})) \\ \overline{\theta}_{k,1} &= \text{asin}(\sin(\theta_{K,1}) - \Delta s_{\theta,1,1k}) \end{aligned} \tag{4.18}$$

This mirroring ambiguity can be resolved with the aid of the second array as pointed in [17]. Use Θ_1 to denote the set of all possible solutions

$$\mathbf{\Theta}_1 = [\theta_{2,1}, \overline{\theta}_{2,1}, ..., \theta_{K-1,1}, \overline{\theta}_{K-1,1}], \tag{4.19}$$

where $\overline{\theta}_{k,1}$ is mirroring version of $\theta_{k,1}$. Similarly, for the second array, we have

$$\mathbf{\Theta}_2 = [\theta_{2,2}, \overline{\theta}_{2,2}, ..., \theta_{K-1,2}, \overline{\theta}_{K-1,2}]. \tag{4.20}$$

Given the known fixed difference angle $\breve{\theta}$, the intersection of $\Theta_2 - \breve{\theta}$ and Θ_1 will give the final estimation results.

4.2.2.2 Joint Group Sparsity Based Method

The above result indicates that, the magnitude-only measurements of the dual-array carry enough information to uniquely identify the DOAs of the impinging signals. Thus, instead of estimating two sets of sinusoidal differences $\Delta s_{\theta,kk',1}$ and $\Delta s_{\theta,kk',2}$ separately and then working out their true values, an effective joint group sparsity based method is proposed to find the DOAs directly.

The measurements at the dual-array can be expressed jointly as

$$\begin{aligned} \mathbf{Y} &= \left[\mathbf{Y}_1^T, \mathbf{Y}_2^T\right]^T \\ &= |\mathbf{AS}| + \mathbf{N}, \end{aligned} \tag{4.21}$$

with

$$\begin{aligned}\mathbf{S} &= \left[\mathbf{s}[0],\cdots,\mathbf{s}[P-1]\right],\\ \mathbf{N} &= \left[\mathbf{N}_1^T,\mathbf{N}_2^T\right]^T,\\ \mathbf{A} &= \left[\mathbf{A}_1^T,\mathbf{A}_2^T\right].\end{aligned} \tag{4.22}$$

Since the first sensor is shared, when forming $\mathbf{A}$ and $\mathbf{Y}$, we can choose to remove the corresponding rows of $\mathbf{A}_2$ and $\mathbf{Y}_2$.

Consider the sparse steering matrix defined in (4.7), it is obvious that the incident signals from an arbitrary arriving angle would share the same spatial support of $\tilde{\mathbf{A}}_1$ and $\tilde{\mathbf{A}}_2$, although the DOAs with respect to each of them are different. As a result, for a sparse overcomplete representation, (4.21) can be expressed as

$$\mathbf{Y} = |\tilde{\mathbf{A}}\tilde{\mathbf{S}}| + \mathbf{N}, \tag{4.23}$$

where $\tilde{\mathbf{S}} = \left[\tilde{\mathbf{s}}[0],\cdots,\tilde{\mathbf{s}}[P-1]\right]$ and the measurement matrix $\tilde{\mathbf{A}}$ is defined as

$$\tilde{\mathbf{A}} = [\tilde{\mathbf{A}}_1^T,\tilde{\mathbf{A}}_2^T]^T. \tag{4.24}$$

Finally, the joint group sparsity based non-coherent DOA estimation problem can be formulated as follows

$$\begin{aligned}\min \quad & ||\tilde{\mathbf{S}}||_{2,1}\\ \text{s.t.} \quad & \|\mathbf{Y}^2 - |\tilde{\mathbf{A}}\tilde{\mathbf{S}}|^2\|_F^2 < \varepsilon.\end{aligned} \tag{4.25}$$

Both problems (4.10) and (4.25) can be solved by the the proposed ToyBar algorithm. Note that, this proposed method will not work if there is only one incident signal due to lack of sinusoidal difference information $\Delta s_{\theta,kk'}$. Therefore, for such a scenario, an additional signal has to be deployed. However, different from existing methods, DOA of the additional signal does not need to be known in advance and its DOA will be estimated simultaneously together with other impinging signals.

4.2.3 Cramér-Rao Bound

In this section, the Cramér-Rao Bound (CRB) for the non-coherent DOA estimation problem is derived. Although an approximation expression of CRB for non-cohernet DOA estimation was derived in [63, 64], a high gain reference signal has to be applied at one end of interested range, which is not applicable to the signal model in this work. Since the reconstructed signals are up to a global phase factor, for complex signal $\mathbf{s}$, the Fisher information matrix (FIM) would be singular [67–69]. Thus, in this work, instead of estimating the phase information of signals, only phase differences between signals are considered.

From (4.21), the probability density function is expressed as

$$p(\mathbf{Y};\mathbf{\Phi}) = \prod_{p}^{P} \prod_{m=0}^{M_1+M_2-1} \frac{1}{2\pi\sigma_m^2} e^{(\mathbf{y}_m[p]-|\mathbf{a}_m\mathbf{s}[p]|)^2/2\sigma_m^2}, \tag{4.26}$$

where $\mathbf{a}_m$ and $\mathbf{y}_m$ represent the m-th row of $\mathbf{A}$ and $\mathbf{Y}$, separately. From the signal model the unknown parameter vector of arriving angles, magnitude, phase difference and noise level can be represented as

$$\begin{aligned} \mathbf{\Phi} &= [\boldsymbol{\theta}, |\boldsymbol{s}[p]|, \Delta\boldsymbol{\gamma}, \sigma^2]^T \\ \boldsymbol{\theta} &= [\theta_1, ..., \theta_K], \\ |\boldsymbol{s}[p]| &= [|s_1[p]|, ..., |s_K[p]|], \\ \mathbf{\Delta\gamma} &= [\Delta\gamma_{12}, \Delta\gamma_{13}, ..., \Delta\gamma_{(K-1)K}], \\ \Delta\gamma_{kk'} &= \gamma_k - \gamma_{k'}, \end{aligned} \tag{4.27}$$

where γ_k is the phase of the k-th signals and σ^2 is noise power. Since there are $\frac{K^2-K}{2}$ cross terms in $|\mathbf{As}[p]|$, there are also $\frac{K^2-K}{2}$ entries in $\mathbf{\Delta\gamma}$. For deterministic but unknown $\mathbf{AS}$, the FIM is defined as

$$\mathbf{FIM}(\mathbf{\Phi}) = \mathbb{E}\{\frac{\partial \ln^2 p(\mathbf{Y};\boldsymbol{\phi})}{\partial\mathbf{\Phi}\partial\mathbf{\Phi}^T}\} \tag{4.28}$$

The $\{i,j\}$-th entry of the FIM $\mathbf{F}$ is given by [70]

$$\begin{aligned}\mathbf{F}_{i,j} = &\Big[\frac{\partial \boldsymbol{\mu}(\boldsymbol{\Phi})}{\partial \Phi_i}\Big]^T \boldsymbol{\Gamma}^{-1}(\boldsymbol{\Phi})\Big[\frac{\partial \boldsymbol{\mu}(\boldsymbol{\Phi})}{\partial \Phi_j}\Big] \\ &+\frac{1}{2}\Big[\boldsymbol{\Gamma}^{-1}(\boldsymbol{\beta})\frac{\partial \boldsymbol{\Gamma}^{-1}(\boldsymbol{\Phi})}{\partial \Phi_i}\boldsymbol{\Gamma}^{-1}(\boldsymbol{\Phi})\frac{\partial \boldsymbol{\Gamma}^{-1}(\boldsymbol{\Phi})}{\partial \Phi_j}\Big],\end{aligned} \tag{4.29}$$

where $\mathbf{I}_{M_1+M_2-1}$ is the identity matrix and $\boldsymbol{\mu}(\boldsymbol{\Phi}) = |\mathbf{AS}|$ and

$$\boldsymbol{\Gamma}^{-1}(\boldsymbol{\Phi}) = \frac{1}{\sigma_m^2}\mathbf{I}_{M_1+M_2-1}. \tag{4.30}$$

Since $\boldsymbol{\mu}(\boldsymbol{\Phi})$ is independent with the noise level, we have

$$\mathbf{F} = \begin{bmatrix}\tilde{\mathbf{F}} & 0\\ 0 & 0\end{bmatrix} + \begin{bmatrix}0 & 0\\ 0 & \mathbf{F}_\sigma\end{bmatrix}, \tag{4.31}$$

where the DOA related block is in $\tilde{\mathbf{F}}$ and its $\{i,j\}$-th entry is expressed as

$$\tilde{\mathbf{F}}_{i,j} = \Big[\frac{\partial \boldsymbol{\mu}(\boldsymbol{\Phi})}{\partial \Phi_i}\Big]^T \boldsymbol{\Gamma}^{-1}(\boldsymbol{\Phi})\Big[\frac{\partial \boldsymbol{\mu}(\boldsymbol{\Phi})}{\partial \boldsymbol{\phi_j}}\Big], \tag{4.32}$$

where $(\cdot)^{-1}$ is the matrix inverse operator. As the FIM is block diagonal, $\mathbf{F}_\sigma$ has no effect on CRB result of DOAs. Thus, CRB of DOAs can be determined by the inverse of $\tilde{\mathbf{F}}$.

Denotes $|\mathbf{a}_m\mathbf{s}| = (\mathbf{s}^H\mathbf{a}_m^H\mathbf{a}_m\mathbf{s})^{\frac{1}{2}} = (\mathbf{s}^H\mathbf{A}_m\mathbf{s})^{\frac{1}{2}}$ and drop index p for convenience, we have

$$
\begin{aligned}
\frac{\partial|\mathbf{a}_m\mathbf{s}|}{\partial\theta_k} &= \frac{1}{2}(\mathbf{s}^H\mathbf{A}_m\mathbf{s})^{\frac{1}{2}}\frac{\partial(\mathbf{s}^H\mathbf{A}_m\mathbf{s})}{\partial\theta_k} \\
&= \frac{1}{2}(\mathbf{s}^H\mathbf{A}_m\mathbf{s})^{-\frac{1}{2}}\Big(jm\frac{2\pi d}{\lambda}\cos\theta_k s_k^*\mathbf{A}_n(k,:)\mathbf{s} \\
&- jm\frac{2\pi d}{\lambda}\cos\theta_k s_k\mathbf{s}^H\mathbf{A}_m(:,k)\Big) \\
&= (\mathbf{s}^H\mathbf{A}_m\mathbf{s})^{-\frac{1}{2}}\mathrm{Im}\Big(-m\frac{2\pi d}{\lambda}\cos\theta_k s_k^*\mathbf{A}_m(k,:)\mathbf{s}\Big) \\
\frac{\partial|\mathbf{a}_m\mathbf{s}|}{\partial|s|_k} &= \frac{1}{2}(\mathbf{s}^H\mathbf{A}_m\mathbf{s})^{-\frac{1}{2}}\frac{\partial(\mathbf{s}^H\mathbf{A}_m\mathbf{s})}{\partial|s|_k} \\
&= \frac{1}{2}(\mathbf{s}^H\mathbf{A}_m\mathbf{s})^{-\frac{1}{2}}(e^{-j\gamma_k}\mathbf{A}_m(k,:)\mathbf{s} \\
&+ e^{j\gamma_k}\mathbf{s}^H\mathbf{A}_m(:,k)) \\
&= (\mathbf{s}^H\mathbf{A}_m\mathbf{s})^{-\frac{1}{2}}\mathrm{Re}\Big(e^{j\gamma_k}\mathbf{s}^H\mathbf{A}_m(:,k)\Big) \\
\frac{\partial|\mathbf{a}_m\mathbf{s}|}{\partial\Delta\gamma_{kk'}} &= \frac{1}{2}(\mathbf{s}^H\mathbf{A}_m\mathbf{s})^{-\frac{1}{2}}\frac{\partial(\mathbf{s}^H\mathbf{A}_m\mathbf{s})}{\partial\Delta\gamma_{kk'}} \\
&= \frac{1}{2}(\mathbf{s}^H\mathbf{A}_m\mathbf{s})^{-\frac{1}{2}}(-js_k^*\mathbf{A}_m(k,k')s_{k'} \\
&+ js_k s_{k'}^*\mathbf{A}_m(k',k)) \\
&= (\mathbf{s}^H\mathbf{A}_m\mathbf{s})^{-\frac{1}{2}}\mathrm{Im}\Big(s_k s_{k'}^*\mathbf{A}_m(k',k)\Big),
\end{aligned}
\tag{4.33}
$$

where $(\cdot)^*$ is the complex conjugate operator, $\mathbf{A}_m(k,:)$ is the k-th row of $\mathbf{A}_m$ and $\mathbf{A}_m(:,k)$ is the k-th column of $\mathbf{A}_m$. Substituting (4.33) into (4.31), the FIM can be obtained as

$$
\tilde{\mathbf{F}} = \sum_{p=1}^{P}\frac{1}{\sigma_m^2}\mathbf{G}[p]\mathbf{G}[p]^H, \tag{4.34}
$$

where

$$
\mathbf{G}[p] = \begin{bmatrix}
\mathrm{Im}\Big(\mathrm{diag}(\mathbf{s}[p]^*)(\mathbf{E}\odot\mathbf{A})^H\mathrm{diag}(\mathbf{A}\mathbf{s}[p])\Big)\tilde{\mathbf{y}}[p] \\
\mathrm{Re}\Big(\mathrm{diag}(e^{-j\boldsymbol{\gamma}})\mathbf{A}^H\mathrm{diag}(\mathbf{A}\mathbf{s}[p])]\Big)\tilde{\mathbf{y}}[p] \\
-\mathrm{Im}\Big(\mathrm{diag}\{\dot{\mathbf{s}}[p]\}\dot{\mathbf{A}}\odot\mathrm{diag}\{\ddot{\mathbf{s}}[p]\}\ddot{\mathbf{A}}\Big)\tilde{\mathbf{y}}[p]
\end{bmatrix}, \tag{4.35}
$$

with

$$
\begin{aligned}
\mathbf{E} &= [\mathbf{e}_1, ...\mathbf{e}_K], \\
\mathbf{e}_k &= [0, \frac{2\pi d}{\lambda}\cos\theta_{k,1}, ..., (M_1-1)\frac{2\pi d}{\lambda}\cos\theta_{k,1}, \\
&\quad \frac{2\pi d}{\lambda}\cos\theta_{k,2}, ..., (M_2-1)\frac{2\pi d}{\lambda}\cos\theta_{k,2}]^T, \\
\tilde{\mathbf{y}}[p] &= \mathrm{diag}\{|\mathbf{A}\mathbf{s}[p]|^{-\frac{1}{2}}\}, \\
\dot{\mathbf{s}} &= [\overbrace{s_1[p], ..., s_1[p]}^{K-1}, \overbrace{s_2[p]..., s_2[p]}^{K-2}, ..., s_{K-1}[p]], \\
\dot{\mathbf{A}} &= [\overbrace{\mathbf{A}(:,1)^T, ..., \mathbf{A}(:,1)^T}^{K-1}, ..., \mathbf{A}(:,K-1)^T], \\
\ddot{\mathbf{s}} &= [s_2^*[p], s_3^*[p], ..., s_K^*[p], s_3^*[p], ..., s_K^*[p], ..., s_K^*[p]], \\
\ddot{\mathbf{A}} &= [\mathbf{A}(:,2)^H, ..., \mathbf{A}(:,K)^H, ..., \mathbf{A}(:,K)^H].
\end{aligned}
\tag{4.36}
$$

The CRB associated with the DOA of signals can be obtained by the diagonal elements of the inverse FIM $\tilde{\mathbf{F}}$.

4.2.4 Grid Refinement

Similar to other compressive sensing based DOA estimation methods, the estimation results of the proposed methods are dependent on the grid size in the angle domain. A denser grid usually leads to a more accurate DOA results, but with a much higher computational complexity,

Therefore, instead of creating a dense grid initially, a coarse grid is firstly made; based on the DOA results, a denser steering matrix is then built around the estimated locations of incident signals [14], and the algorithm is employed again to find a more accurate DOA.

4.2.5 Simulations

In this section, performance of the two proposed non-coherent DOA estimation methods based on the dual-array structure is investigated. Inter-sensor distance d of both arrays is $\lambda/4$ in order to avoid spatial order ambiguity. The number of snapshots P collected is set to 20 in all following simulations. The numbers of sensors of both arrays are set as $M_1 = M_2 = 20$

while angle $\breve{\theta}$ between them are 20° unless specified otherwise. No reference signals is employed, and the proposed ToyBabar is applied and steering matrices of first and second arrays are formed with a step size of 0.5° for both separate estimation and jointly group sparsity methods.

4.2.5.1 Separate Estimation method

Consider an example that there are $K = 3$ signals impinging on the array, with incident angles $-30^\circ, 0^\circ$, and 30° (relative to the first array). The signal to noise ratio is 20 dB. DOA results of an single trial have been shown in Table 4.1, which indicates that signals can be identified correctly without the presence of reference signal with non-coherent measurements.

Table 4.1 DOA estimation result by the separate estimation method

True DOA	Average Estimated DOA
-30°	-29.84°
0°	0.33°
30°	30.18°
RMSE	0.236°

In the second set of simulations, the estimation accuracy with respect to input SNR with different sensor numbers is considered. There are three unknown signals from the same set of directions as before. The RMSE results are shown in Fig. 4.2. As expected, a higher SNR has yielded a more accurate result. When SNR$\geq$ 15dB, noise has a limited effect with RMSEs being smaller than 2° when M =20 and tend to zero by increasing the number of sensors. However, when noise level is equal or higher than 5 dB, noise has a more serious effect.

For the third set of simulations, with SNR fixed at 20 dB, the RMSE performance with respect to the DOA separation between adjacent signals is investigated. The number of sensors of each array is set from 20 to 60. In Fig. 4.3, the RMSE result for $K = 2$ signals are provided, with one signal fixed at 45° (relative to the first array) and the other located at $+h^\circ$ away from it. Each point presented in Fig. 4.3 is again an average over 100 trials. Evidently, the accuracy improves with a larger separation h° and an increasing number of sensors.

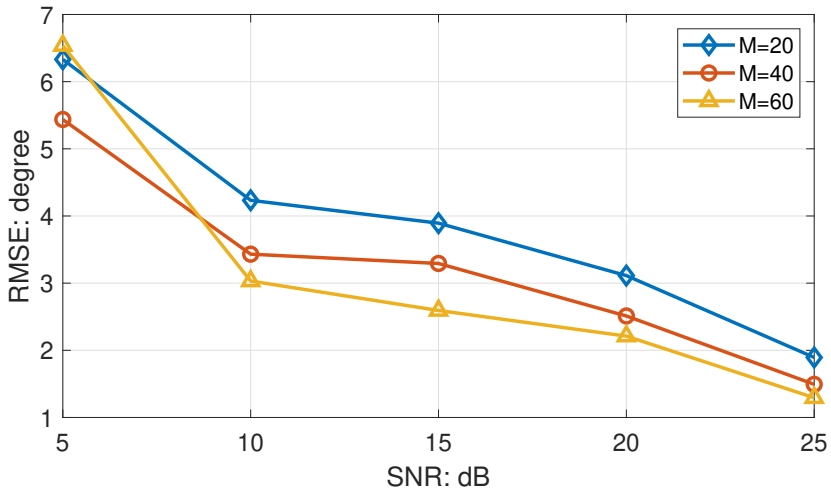

Fig. 4.2 RMSE result versus input SNR with different number of sensors.

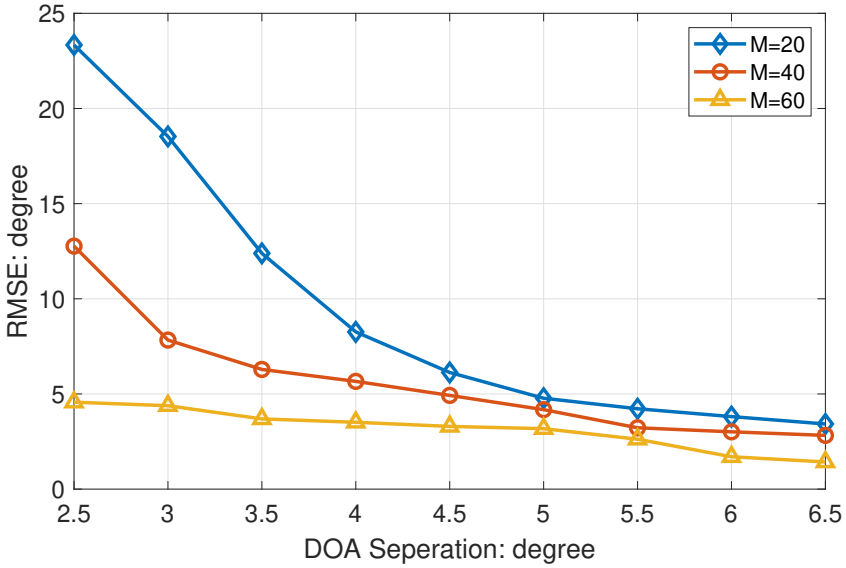

Fig. 4.3 RMSE result versus DOA separation with different number of sensors.

4.2.5.2 Joint Group Sparsity Based Method

In this section, the joint group sparsity based method is investigated, where $K = 3$ signals arriving from -60°, 0°, and 30° with respect to the first array are considered. The first simulation compares the estimation result from separate estimation method and jointly group sparsity based method, which are shown in Table 4.2 , where the input SNR is considered as 15 dB. Clearly, both methods are able to closely identify or correctly locate all 3 incident angles, but the separate estimation method leads to less accurate estimation results. One possible reason is that (4.15) is not sensitive to incident angles when they close to $\pm\frac{\pi}{2}$ and results in a large calculation error for those angles. On the contrary, as the jointly group sparsity method further exploits spatial structure of the dual-array, it has smaller estimation errors. Additionally, a normalised spectrum of the proposed method is presented in Fig. 4.4.

Table 4.2 DOA estimation result by the separate estimation method

True DOA	-60°	0°	30°
Separate Estimation Method	-62.0°	0.6°	30.4°
Jointly Group Sparse Method	-60.0°	0.0°	30.5°

In order to illustrates the performances of separate estimation and jointly group sparse methods with different SNR, the performances are evaluated by the RMSE results as a function of SNR and its simulation is presented in Fig. 4.5, with each point obtained by averaging over 100 trials. Not surprisingly, although both methods acquire more accurate results with increasing SNR, the jointly group method consistently outperforms the separate estimation one.

We also examine the performance of both non-coherent and coherent methods in the presence of sensor phase errors. RMSE results are obtained with an average of 100 trials. For the coherent method, l_1-svd is applied [14]. The SNR is fixed at 20 dB, while the entries of the phase error matrix $\mathbf{E}$ follow the Gaussian distribution with standard deviation σ. As shown, the proposed non-coherent method is not affected by phase errors, with a steady performance, while the performance of the coherent method declines as the intensity of phase errors increases.

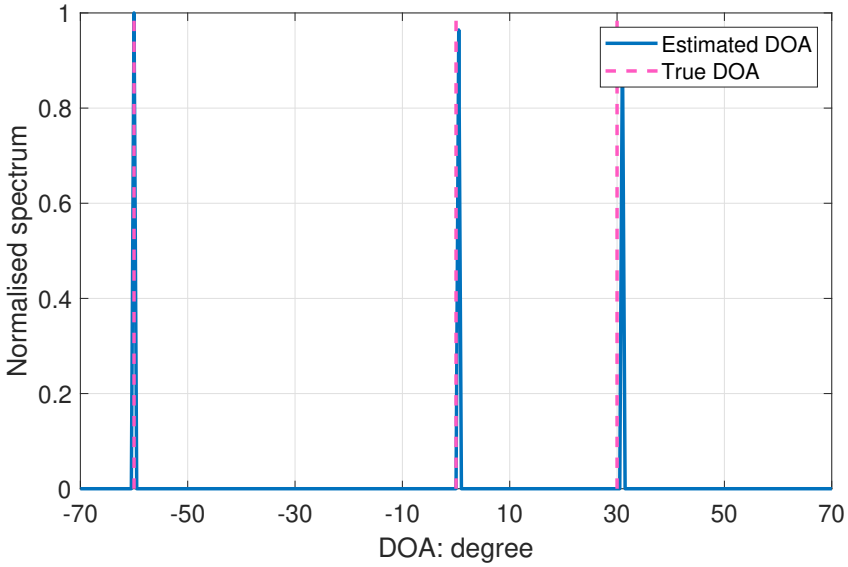

Fig. 4.4 Normalized spectrum of joint estimation method.

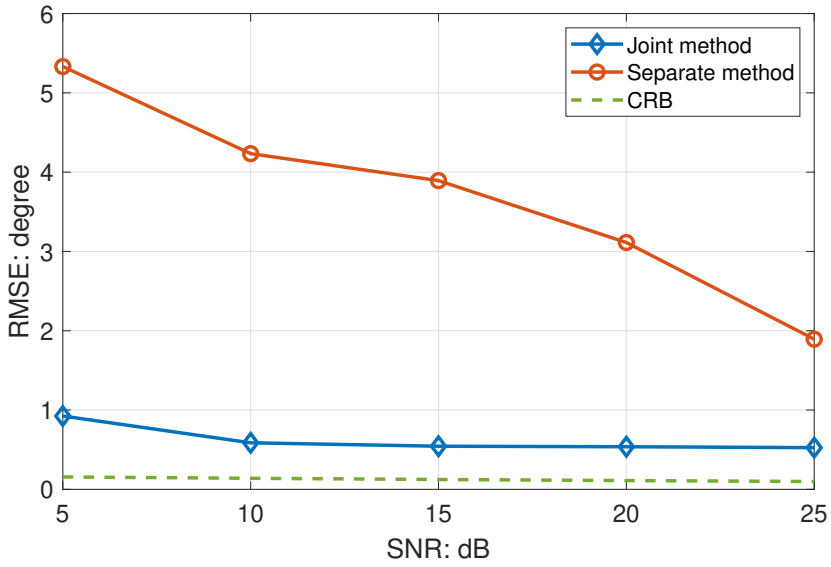

Fig. 4.5 RMSE results versus SNR.

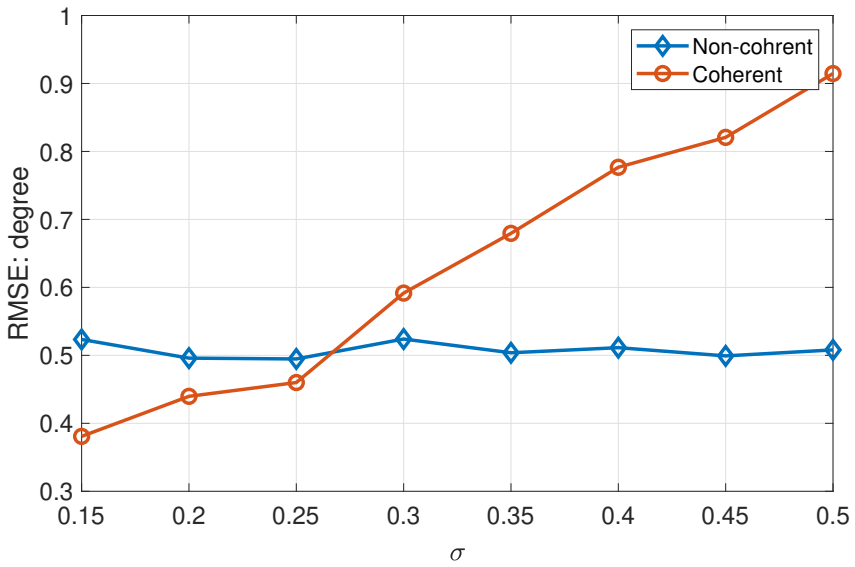

Fig. 4.6 RMSE results versus sensor phase error.

Furthermore, based on the dual-array structure, the performance of ToyBar proposed in last chapter is further studied and compared with the modified GESPAR [16]. The angle between the two subarrys is set as $\breve{\theta} = 20^\circ$ unless specified otherwise. Accordingly, the area of interest for the first array is set to $[-70^\circ, 90^\circ]$ while for the second array it is $[-90^\circ, 70^\circ]$. Grid refinement is empolyed in the following comparison, with a step size of 0.5° for initial DOA estimation. After obtaining the initial DOA eastimates $\hat{\theta}_k$, the grid refinement approach is applied, with a new grid with stepsize 0.05° is formed around an interval of $\hat{\theta}$, which includes 1.5° to either side of it. i.e 0.05° spacing within $[\hat{\theta}_k - 1.5^\circ, \hat{\theta}_k + 1.5^\circ]$. While applied the refine step to GESPAR, the iterations halved as the number of grids decreased. Results obtained with this refinement step are referred to as “ToyBar-Refined" and “GESPAR-Refined" in the following.

The SNR is 15 dB and there are $K = 3$ signals impinging on the array, with incident angles $-30^\circ, -10^\circ$, and 50° (relative to the first array). The number of snapshots is 20 and the number of sensors is $M_1 = M_2 = 20$. Fig. 4.7 provides the result of ToyBar, while Fig. 4.8 is for GESPAR. The dotted lines represent the true incident angles. It can be seen that all 3 signals have been identified by both GESPAR and the proposed method. However,

Table 4.3 Running times versus number of snapshots.

Snapshots	20	60	100
Toybar(s)	57.7	84.6	115.2
ToyBar-Refined(s)	89.2	134.1	181.4
GESPAR(s)	2154.2	6551.4	10816.5
GESPAR-Refined(s)	3384.7	10317.6	17045.5

although GESPAR provides a sharper peak, it requires prior knowledge of the number of incident signals, while the proposed method does not.

Next, performances of the proposed ToyBar and GESPAR are evaluated with different SNR values ranging from 5 dB to 25 dB with three signals identical to the first experiment in terms of the root mean square error (RMSE), and the results are shown in Fig. 4.9, with each point obtained by averaging over 100 trials. Clearly, both algorithms have achieved more accurate results with increasing SNR, but the estimation of the proposed ToyBar is slightly more accurate than GESPAR; besides, the refined step is able to further improve the performance of both algorithms, but the refined ToyBar also outperforms the refined GESPAR.

In Fig. 4.10, results of RMSE versus the number of snapshots of both algorithms are provided. SNR is fixed at 15 dB but the number of snapshots P is from 20 to 100. Each point is averaged over 100 trials. Under all snapshot settings, the proposed algorithm has a lower RMSE than the modified GESPAR. In addition, compared to the proposed ToyBar, the modified GESPAR is less sensitive to snapshots.

To compare the computational complexity of GESPAR and the proposed ToyBar with the dual-array, the average computation time of both algorithms with different number of snapshots is listed in Table 4.3, where the average running time of both algorithms are under CPU I5 5200U at 2.2GHz and 4 GB RAM. It can be seen that an increasing number of snapshots significantly increases the running time of GESPAR and it always requires much longer running time than the proposed method. Similarly, the computational complexity of GESPAR-Refined is also much higher than ToyBar-Refined.

Finally, the performance of the DOA esitmation results under various angles $\breve{\theta}$ between the two arrays is examined. The RMSE results versus $\breve{\theta}$ is shown in Fig. 4.11. SNR$=$ 15

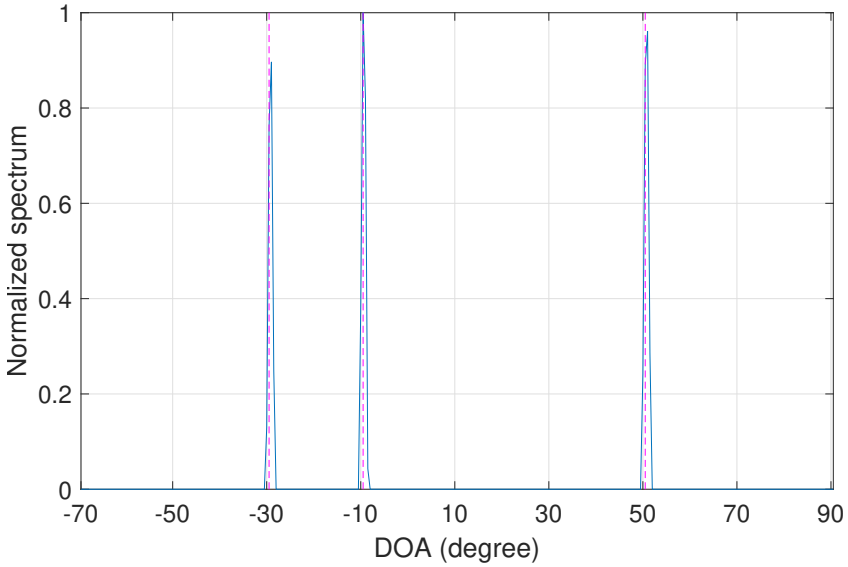

Fig. 4.7 Estimation results by the proposed ToyBar.

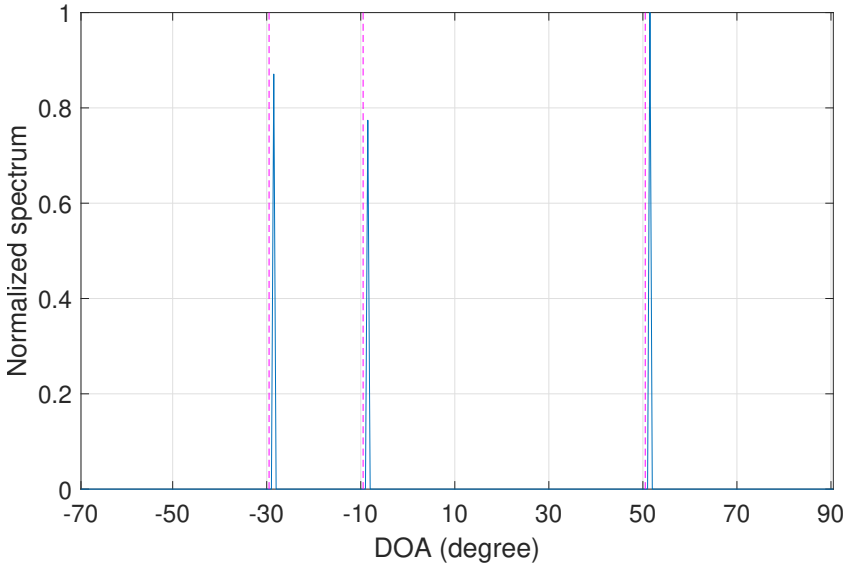

Fig. 4.8 Estimation results by the modified GESPAR.

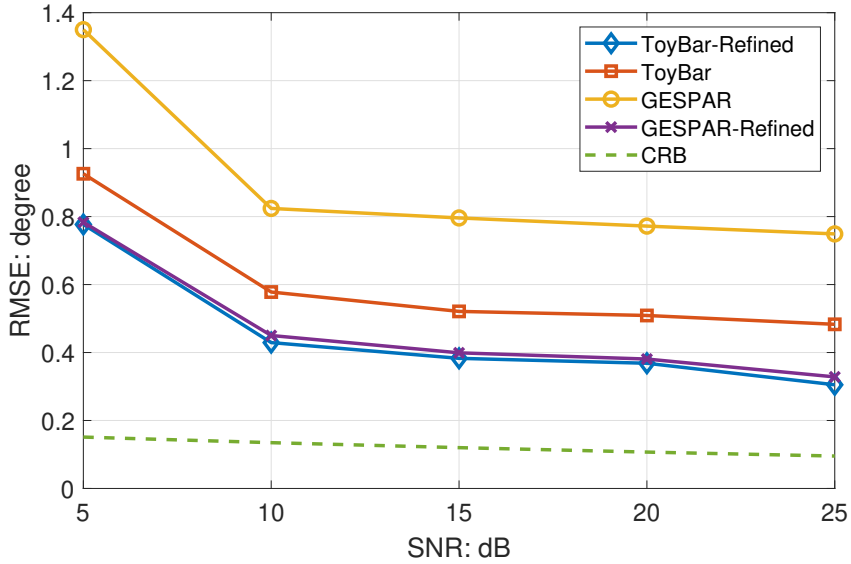

Fig. 4.9 RMSEs versus different SNR.

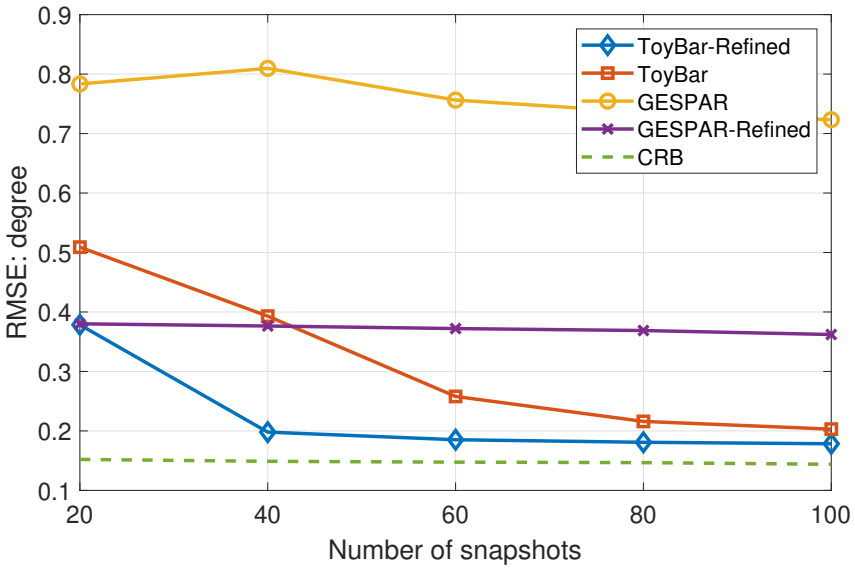

Fig. 4.10 RMSEs versus number of snapshots.

dB and other simulation parameters are the same as the first simulation. It can be seen that, although a larger $\check{\theta}$ always improves the estimation accuracy. the proposed Toybar has a better performance than the modified GESPAR. In addition, the refinement step can improve the performance of the proposed ToyBar and the modified GESPAR significantly when $\check{\theta}$ is small. However, since the effective range of estimation is restricted by $\check{\theta}$, $\check{\theta}$ should be chosen carefully in order to cover more area within $[-90°, 90°]$.

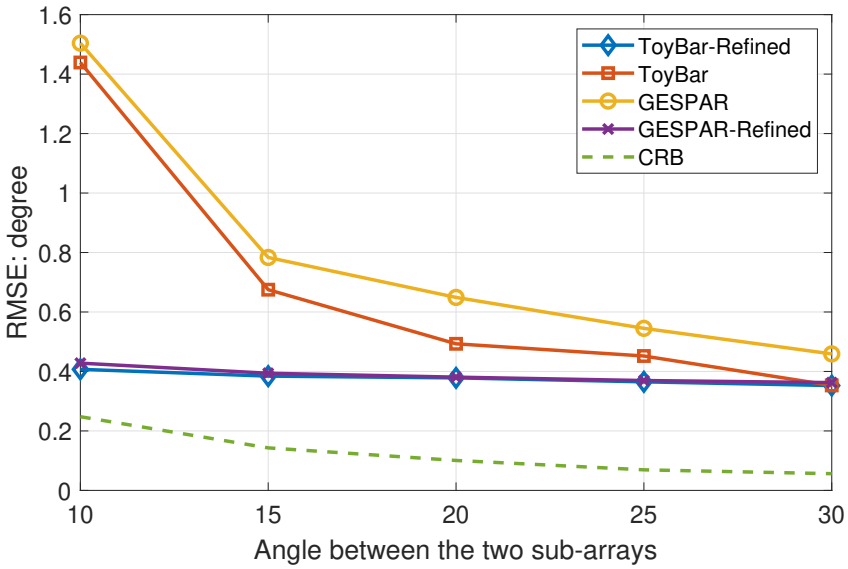

Fig. 4.11 RMSE results versus $\check{\theta}$ for SNR=15dB.

4.3 Non-Coherent DOA Estimation with UCA

4.3.1 Signal Model with UCA

Although the proposed dual-array structure works well, a small area within $[-90°, 90°]$ has to be sacrificed. Therefore, in order to deal with the full range $[-90°, 90°]$, non-coherent DOA estimation with UCA is investigated. A UCA consists of M sensors with inter-sensor spacing d is presented in Fig. 4.12, where the radius r of the circular array is given by

$$r = \frac{Md}{2\pi}. \tag{4.37}$$

Accordingly, the steering vector of the k-th signal $\mathbf{a}(\theta_k)$, for $k = 1, ..., K$, is expressed as [71]

$$\mathbf{a}(\theta_k) = [e^{j\xi\cos(\theta_k-\gamma_1)}, ..., e^{j\xi\cos(\theta_k-\gamma_M)}]^T, \tag{4.38}$$

where $\xi = 2\pi r/\lambda$, and $\gamma_m = 2\pi m/M$, $m = 1, ..., M$.

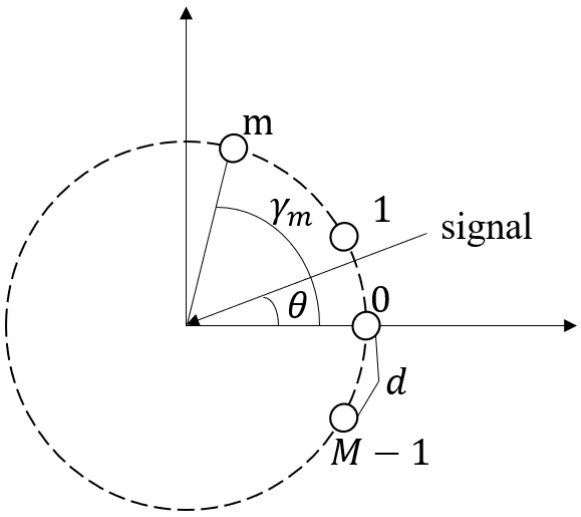

Fig. 4.12 A uniform circular array with M sensors and a inter-sensor spacing of d, where a signal impinges from θ.

Under the sparsity framework, the admissible DOA range is divided into G grid points with $G \gg N$, and an overcomplete steering matrix

$$\tilde{\mathbf{A}} = [\mathbf{a}(\theta_1), ..., \mathbf{a}(\theta_G)] \tag{4.39}$$

can be formed with each column representing a potential incident angle. Accordingly, the signal vector $\mathbf{s}[p]$ is extended to a $G \times 1$ sparse matrix $\tilde{\mathbf{S}} \in \mathbb{C}^{G\times P}$, where only K rows at the corresponding incident angles are supposed to be non-zero. The array measurements of UCA is formulated as

$$\mathbf{Y} = |\tilde{\mathbf{A}}\tilde{\mathbf{S}}| + \mathbf{N}, \tag{4.40}$$

where $\mathbf{Y} = \big[\mathbf{y}[0], ..., \mathbf{y}[P-1]\big]$, and $\mathbf{N} = \big[\mathbf{n}[0]], ..., \mathbf{n}[P-1]\big]$.

4.3.2 Ambiguity

Results obtained from non-coherent measurements with uniform linear array (ULA) suffers from some inherent ambiguities, which would affect the DOA estimation results: mirroring and spatial shift [44]. Denote the measurement at the m-th sensor of the UCA as

$$x_m = \sum_{k=1}^{K} s_k e^{j\xi\cos(\theta_k - \gamma_m)}, \tag{4.41}$$

where time index p is dropped. Next, the ambiguities issues with UCA is addressed.

For mirroring ambiguity, it refers to the phenomenon that signals arriving from $-\theta_k$ will generate the measurements with the same magnitude. With UCA, however, we have

$$|\check{x}_m| = |\sum_{k=1}^{K} s_k e^{j\xi\cos(-\theta_k - \gamma_m)}| = |\sum_{k=1}^{K} s_k e^{j\xi\cos(\theta_k + \gamma_m)}|. \tag{4.42}$$

Obviously, the magnitude of $\check{x}_m$ is in general different from x_m, thus the mirroring ambiguity in ULAs will not appear in UCAs.

For spatial shift ambiguity, it refers to that the received signals at the array are phased shifted by a specific amount ϕ_m,

$$\check{x}_m = e^{j\xi\phi_m} \sum_{k=1}^{K} s_k e^{j\xi\cos(\theta_k - \gamma_m)} = \sum_{k=1}^{K} s_k e^{j\xi\cos(\theta_k - \check{\theta}_{m,k} - \gamma_m)}. \tag{4.43}$$

Although $\check{x}_m$ would share the same magnitude as with x_m at the m-th sensor, $\check{\theta}_{m,k}$ for the corresponding k-th signal at different sensors are different due to the non-linear property of the cosine function, which implies that, there is no common shift variable ϕ_m to simultaneously keep the same magnitude as x_m and same shifted angle $\check{\theta}_{m,k}$ for all M sensors.

Thus, we can conclude that the inherent mirroring and spatial shift ambiguities involved in ULAs will not appear in UCAs. But there is another ambiguity involved in non-coherent measurements of UCAs. For the whole range $[-\pi, \pi]$, K incident signals $\mathbf{s}^*$ from angle $(\theta_k \pm \pi)$ would share the same magnitude as x_m, expressed as

$$\check{x}_m = \sum_{k=1}^{K} s_k^* e^{j\xi\cos(\theta_k \pm \pi - \gamma_m)} = \sum_{k=1}^{K} s_k^* e^{-j\xi\cos(\theta_k - \gamma_m)} = x_m^*. \tag{4.44}$$

There are two possible solutions to solve this ambiguity. One is to limit the area of interest to $[-90^\circ, 90^\circ]$, since for $-\pi/2 \leq \theta_k \leq \pi/2$, $\theta_k \pm \pi$ will exceed the limit.

Another one is applying a reference signal at the end of interested area $[-\pi]$ and assume no signal come from 0° (Generally, define θ_{ref} and remove either column of $[\theta_{ref} \pm \pi]$ as appropriate from $\tilde{\mathbf{A}}$). With this reference signal, either $\theta_k - \pi$ or $\theta_k + \pi$ will be out of the range $[-\pi, \pi]$. In practice, due to influence of noise, a short range of $[\theta_k \pm \pi - u, \theta_k \pm \pi + u]$ should be removed from the area of interest.

Note that, as mentioned earlier, non-coherent DOA estimation does not work if there is only one incident signal; and for such a scenario, a reference signal has to be deployed; however, its DOA does not need to be known in advance.

4.3.3 Simulations

Simulation results are provided to show the performance of the UCA without reference signals. The area of interest is considered within $[-\pi/2, \pi/2]$ with a grid step size 0.5° to avoid ambiguity involved in UCAs. The number of sensors N is set as 19 while the radius r of UCAs is set as $r = Md/2\pi$ with $d = \lambda/2$, and $P = 500$ snapshots are collected in all simulations. ToyBar is applied, its iteration number is 500 and 30 random initializations are used in order to find the global minimum.

In the simulations, $K = 3$ signals with DOA -40°, 0° and 30° are placed. With input SNR fixed at 20 dB, the spectrum of the DOA estimation result is shown in Fig. 4.13, where dotted lines represent true DOAs and solid lines are estimated ones. It can be seen that unambiguous results has been obtained directly. RMSE results of UCA with different SNR values ranging from 0 dB to 20 dB are also displayed in Fig. 4.14 , with each point being an average of 100 trials. The Cramér-Rao bound is also provided, as derived in Section 4.2.3.

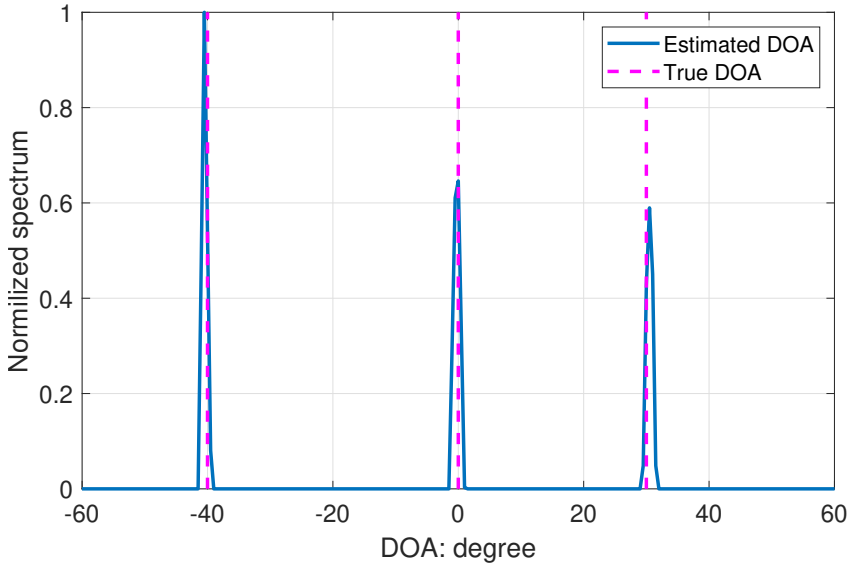

Fig. 4.13 Normalised spectrum.

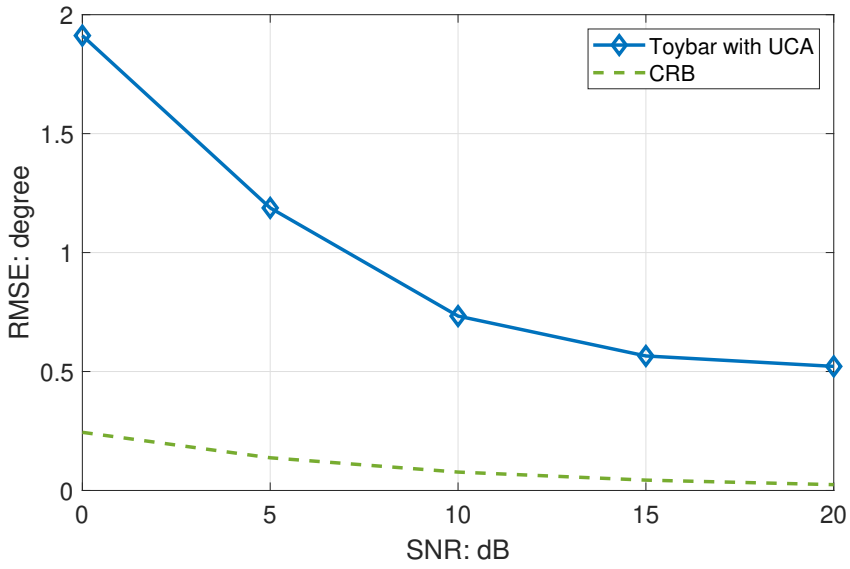

Fig. 4.14 Results by on-grid model.

4.4 Summary

Two array structures to remove the spatial shift and mirroring ambiguity for non-coherent DOA estimation without reference signals have been proposed. The first is a novel dual-array structure, which exploits the spatial information of both sub-arrays simultaneously, while the second is the UCA structure. Based on these two array structures, similar joint group sparsity based phase retrieval problems have been formulated and Toybar or other existing group sparsity based solutions can be applied to identify the unambiguous DOAs directly.

Chapter 5

Off-Grid Non-Coherent DOA Estimation and Source Localization of Narrowband Signals

In the sparsity based DOA estimation methods, DOAs of incident signals are assumed to fall on the discrete grid points. In practice, quite often the true DOAs may not lie on the predefined grid points, which leads to an off-grid problem. One solution to it is applying a denser grid, which significantly increases the computational complexity. Another solution is grid refinement [14], which defines a coarse grid at first and then, based on the initial DOA results, a denser steering matrix is built around the estimated locations of incident signals. However, computational complexity of this method is still high. Moreover, source localization is another important problem in sensor array signal processing and it faces a similar challenge for sparsity based solutions.

Although several off-grid methods has been proposed for coherent DOA estimation [72–77], off-grid DOA estimation and source localization with non-coherent measurements has not been addressed yet. In this chapter, off-grid DOA estimation and source localization problem with magnitude-only measurements is studied, where UCA is employed in order to be reference-signal free.

The remaining part is structured as follows. The off-grid non-coherent signal and DOA estimation method with simulation results is presented in Section 5.1. The off-grid signal model with distributed sensor arrays for source localization is described in Section 5.2, with a non-coherent localisation method is proposed, supported by simulation results. Conclusions are drawn in Section 5.3.

5.1 Off-Grid DOA Estimation

5.1.1 The Developed Algorithm

The non-coherent DOA estimation method has been proposed in the last chapter, where the DOAs of signals are assumed to be located on the predefined grids. While the signals are off the grids, we let

$$\overline{\boldsymbol{\theta}} = [\overline{\theta}_1, ..., \overline{\theta}_k] \tag{5.1}$$

denote the true DOAs of K incident signals off the pre-defined grids and θ_{g_k} represent the nearest grid point for the k-th signal. Array measurements under the sparsity framework can be approximated by

$$\begin{aligned} \mathbf{X} &\approx (\tilde{\mathbf{A}} + \tilde{\mathbf{B}}\tilde{\boldsymbol{\Delta}})\tilde{\mathbf{S}}, \\ \tilde{\mathbf{B}} &= [\mathbf{b}(\theta_1), ..., \mathbf{b}(\theta_G)], \\ \mathbf{b}(\theta_g) &= \frac{\partial \mathbf{a}(\theta_g)}{\partial \theta_g}, \\ \tilde{\boldsymbol{\Delta}} &= \mathrm{diag}(\tilde{\boldsymbol{\beta}}), \end{aligned} \tag{5.2}$$

where

$$\beta_g = \begin{cases} \bar{\theta}_k - \theta_{g_k}, & \text{if } g = g_k, \\ 0, & \text{otherwise.} \end{cases} \tag{5.3}$$

β_g satisfies

$$-\frac{v}{2} \leq \beta_g \leq \frac{v}{2}, \tag{5.4}$$

and v is grid stepsize. As a result, the non-coherent measurements are formulated into

$$\mathbf{Y} \approx |(\tilde{\mathbf{A}} + \tilde{\mathbf{B}}\tilde{\mathbf{\Delta}})\tilde{\mathbf{S}}| + \mathbf{N}. \tag{5.5}$$

The off-grid non-coherent DOA estimation problem can be solved by the following unconstrained optimisation problem

$$\min_{\tilde{\mathbf{S}},\tilde{\mathbf{\Delta}}} \; \||(\tilde{\mathbf{A}} + \tilde{\mathbf{B}}\tilde{\mathbf{\Delta}})\tilde{\mathbf{S}}| - \mathbf{Y}\|_F^2 + \rho\|\tilde{\mathbf{S}}\|_{2,1}. \tag{5.6}$$

where the $\|\cdot\|_{2,1}$ is the $l_{2,1}$ norm, which enforces row sparsity of $\tilde{\mathbf{S}}$. Jointly estimate $\tilde{\mathbf{\Delta}}$ and $\tilde{\mathbf{S}}$ from (5.6) is a non-convex optimization problem. In the following, a two-step method is proposed.

In the first step, $\tilde{\mathbf{\Delta}}$ is assumed to be zero, and the corresponding optimization problem is formulated as

$$\min_{\tilde{\mathbf{S}}} \; \||\tilde{\mathbf{A}}\tilde{\mathbf{S}}| - \mathbf{Y}\|_F^2 + \rho\|\tilde{\mathbf{S}}\|_{2,1}, \tag{5.7}$$

The objective function (5.7) can be solved by existing group sparse phase retrieval algorithms, such as the proposed ToyBar.

In the second step, in order to estimate the off-grid bias, the PRIME technique [48] is employed. After applying PRIME column by column to (5.6), its first term can be replaced by a convex surrogate, and the corresponding objective function is changed to

$$\min_{\tilde{\mathbf{S}}} \; \|(\tilde{\mathbf{A}} + \tilde{\mathbf{B}}\tilde{\mathbf{\Delta}})\tilde{\mathbf{S}} - \bar{\mathbf{C}}\|_F^2 + \rho\|\tilde{\mathbf{S}}\|_{2,1}, \tag{5.8}$$

with

$$\bar{\mathbf{C}} = \mathbf{Y} \odot e^{j\arg((\tilde{\mathbf{A}}+\tilde{\mathbf{B}}\mathbf{\Delta})\tilde{\mathbf{S}}_e)}, \tag{5.9}$$

where $\tilde{\mathbf{S}}_e$ is estimated signals from step one, which is up to a global phase ambiguity.

After that, similar to [77], an iterative algorithm for estimating dictionary bias $\tilde{\boldsymbol{\beta}}$ is proposed. This method first estimates K non-zero rows of estimated signals $\tilde{\mathbf{S}}_e$ as

$$\bar{\boldsymbol{s}}_K^i = (\bar{\boldsymbol{A}}_K^i)^\dagger \bar{\mathbf{C}}, \tag{5.10}$$

where $(\cdot)^{\dagger}$ is the pseudo-inverse operator, $i \in \{1,...,I\}$ is iteration index,

$$\bar{\boldsymbol{A}}_K^i = \bar{\boldsymbol{A}}(\theta_K^i) \tag{5.11}$$

is the steering matrix with K columns corresponding the estimated DOAs $\boldsymbol{\theta}^i = [\theta_1^i,...,\theta_K^i]$, and θ_K^i is updated in each iteration. $\bar{\mathbf{A}}_K^0$ is initialized as K columns of $\tilde{\mathbf{A}}$, which corresponds to DOAs of estimated signals $\tilde{\mathbf{S}}_e$. As the bias $\tilde{\boldsymbol{\beta}}$ shares same support with $\tilde{\mathbf{S}}_e$, $\bar{\mathbf{B}}_K$ is obtained, which is the sub-matrix of $\tilde{\mathbf{B}}$ with corresponding K columns at the support of $\tilde{\mathbf{S}}_e$. By denoting

$$\begin{aligned} \bar{\boldsymbol{\Delta}}_K^i &= \mathrm{diag}(\bar{\boldsymbol{\beta}}_K^i), \\ \bar{\boldsymbol{\beta}}^i &= [\beta_1^i,...\beta_K^i]^T, \end{aligned} \tag{5.12}$$

as the bias of corresponding DOAs of incident signals, $\bar{\boldsymbol{\Delta}}_K^i$ can be estimated by solving

$$\min_{\bar{\boldsymbol{\beta}}_K} \|(\bar{\mathbf{A}}_K + \bar{\mathbf{B}}_K\bar{\boldsymbol{\Delta}}_K^i)\bar{\mathbf{S}}_K^i - \bar{\mathbf{C}}\|_F^2. \tag{5.13}$$

Dropping index i for simplicity, (5.13) can be reformulated as [73, 77]

$$\begin{aligned} &\|(\bar{\mathbf{A}}_K + \bar{\mathbf{B}}_K\bar{\boldsymbol{\Delta}}_K)\bar{\mathbf{S}}_K - \bar{\mathbf{C}}\|_F^2 \\ &\approx \mathrm{tr}\big\{\bar{\mathbf{S}}_K^H\bar{\boldsymbol{\Delta}}\bar{\mathbf{B}}_K^H\bar{\mathbf{B}}_K\bar{\boldsymbol{\Delta}}\bar{\mathbf{S}}_K\big\} - 2\mathrm{Re}\big\{(\bar{\mathbf{C}} - \bar{\mathbf{A}}\bar{\mathbf{S}}_K)^H\bar{\mathbf{B}}_K\bar{\boldsymbol{\Delta}}_K\bar{\mathbf{S}}_K\big\} \\ &= \bar{\boldsymbol{\beta}}_K^T\big(\bar{\mathbf{B}}_K^H\bar{\mathbf{B}}_K \odot (\bar{\mathbf{S}}_K\bar{\mathbf{S}}_K^H)^*\big)\bar{\boldsymbol{\beta}}_K \\ &- 2\mathrm{Re}\big\{\mathrm{diag}[\bar{\mathbf{S}}_K(\bar{\mathbf{C}} - \bar{\mathbf{A}}_K\bar{\mathbf{S}}_K)^H\bar{\mathbf{B}}_K]\bar{\boldsymbol{\beta}}_K\big\}, \end{aligned} \tag{5.14}$$

where $\mathrm{tr}(\cdot)$ and $\mathrm{Re}(\cdot)$ represent the trace and real part of its variable, separately. With the optimal condition of (5.14), $\bar{\boldsymbol{\beta}}_K^i$ can be obtained by

$$\bar{\boldsymbol{\beta}}_K^i = \mathrm{Re}\{(\mathbf{D}^i)^{-1}\mathbf{h}^i\}, \tag{5.15}$$

where $(\cdot)^{-1}$ is the inverse operator, and

$$\begin{aligned}\mathbf{D}^i &= \bar{\mathbf{B}}_K^H \bar{\mathbf{B}}_K \odot (\bar{\mathbf{S}}_K^i \bar{\mathbf{S}}_K^i)^*, \\ \mathbf{h}^i &= \left\{\text{diag}[\bar{\mathbf{S}}_K^i (\bar{\mathbf{C}} - \bar{\mathbf{A}}_K \bar{\mathbf{S}}_K^i)^H \bar{\mathbf{B}}_K]\right\}^T.\end{aligned} \tag{5.16}$$

Since $-\frac{v}{2} \leq \beta_g \leq \frac{v}{2}$, for $k = 1, ..., K$, it has

$$\beta_k^{i+1} = \begin{cases} -v/2, & \text{if } \beta_k^i < v/2, \\ v/2 & \text{if } \beta_k^i > v/2, \\ \beta_k^i, & \text{otherwise.} \end{cases} \tag{5.17}$$

Note that, the non-coherent DOA estimation results still suffer from the global phase ambiguity, that is

$$\begin{aligned}\bar{\mathbf{C}} &= \mathbf{Y} \odot e^{j\arg(\tilde{\mathbf{A}}\tilde{S}_e)} \approx \mathbf{A}_r \mathbf{S}_r e^{j\phi}, \\ \bar{\mathbf{S}}_K &= (\bar{\boldsymbol{A}}_K^t)^\dagger \bar{\mathbf{C}} \approx \mathbf{S}_r e^{j\phi},\end{aligned} \tag{5.18}$$

where $\mathbf{S}_r$ and $\mathbf{A}_r$ represent the real signal and its corresponding real steering matrix, respectively, and ϕ is a global phase factor. It can be seen that, when substituting (5.18) into (5.15), the global phase factor cancels, which means that the global phase ambiguity will not affect bias estimation in this step. With $\bar{\boldsymbol{\beta}}^i$, the steering matrix $\bar{\mathbf{A}}_K$ is updated as

$$\boldsymbol{\theta}^{i+1} = \boldsymbol{\theta}^0 + \boldsymbol{\beta}^i, \;\; \bar{\boldsymbol{A}}_K^{i+1} = \bar{\boldsymbol{A}}_K(\theta^{i+1}). \tag{5.19}$$

where θ^0 is the initial DOAs obtained from the first step, i.e corresponding DOA of the non-zero rows of $\tilde{\boldsymbol{S}}_e$. Finally, the output DOA $\boldsymbol{\theta}_e$ is obtained as

$$\boldsymbol{\theta}_e = \boldsymbol{\theta}_0 + \boldsymbol{\beta}^I. \tag{5.20}$$

The full algorithm is summarized in the Table 5.1.

Table 5.1 Algorithm Summary (Two-Step Off-Grid)

Input: $\tilde{\mathbf{A}}$, $\mathbf{Y}$,
Initializtion: $\bar{\boldsymbol{\beta}}_K^0 = \mathbf{0}$.
Step 1: Estimate $\tilde{\mathbf{S}}_e$ via existing group sparse phase retrieval algorithms.
Obtain $\bar{\boldsymbol{A}}_K^0$ and $\boldsymbol{\theta}^0$,
Calculate $\bar{\mathbf{C}} = \mathbf{Y} \odot e^{j\arg(\tilde{\mathbf{A}}\tilde{\mathbf{S}}_e)}$.
Step 2: for i=1, ..., I
1) Calculate $\bar{\mathbf{S}}_K^i = (\bar{\boldsymbol{A}}_K^i)^\dagger \bar{\mathbf{C}}$.
2) Calculate $\bar{\boldsymbol{\beta}}_K^i = \mathrm{Re}\{(\mathbf{D}^i)^{-1}\mathbf{h}^i\}$ from (5.16),
3) Restrict elements of $\bar{\boldsymbol{\beta}}_K^i$ within range $[-\frac{v}{2}, \frac{v}{2}]$.
4) Calculate $\boldsymbol{\theta}^{i+1} = \boldsymbol{\theta}^0 + \boldsymbol{\beta}_K^i$,
$\bar{\mathbf{A}}_K^{i+1} = \bar{\mathbf{A}}_K(\theta^{i+1})$.
Output estimated DOA: $\boldsymbol{\theta}_e = \boldsymbol{\theta}^0 + \bar{\boldsymbol{\beta}}^I$.

5.1.2 Simulation Results

In this section, simulation results are provided to show the performance of the proposed off-grid non-coherent DOA estimation method in comparison with the on-grid model, where results of on-grid model are obtained from the first step of the proposed method. The area of interest is considered within $[-\pi/2, \pi/2]$ to avoid ambiguity involved in UCAs. The number of sensors N is set as 19 while the radius r of UCAs is set as $r = Md/2\pi$ with $d = \lambda/2$, and $P = 500$ snapshots are collected in all simulations. ToyBar is applied in the first step of the proposed method, its iteration number is 500 and 30 random initializations are used in order to find the global minimum of the phase retrieval problem, while the iteration number for the second step is 50.

In the first set of simulations, the steering matrix is formed with a step size of 2° and input SNR is set as 20 dB. DOA estimation results of both on-grid and off-grid model are compared and shown in Figs. 5.1 and 5.2, where dotted lines represent true DOAs and solid lines are estimated ones. We can observe that, although both models can identify DOAs more or less correctly, the off-grid model provides a more accurate result.

In the second set of simulations, RMSE results of the off-grid model and on-grid model with different SNR values ranging from 0 dB to 20 dB are compared, with each point being

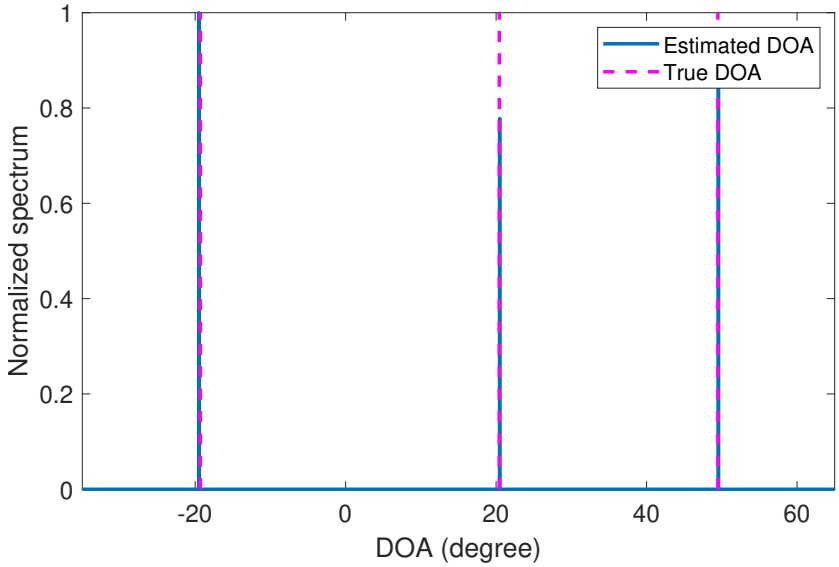

Fig. 5.1 Results by off-grid model.

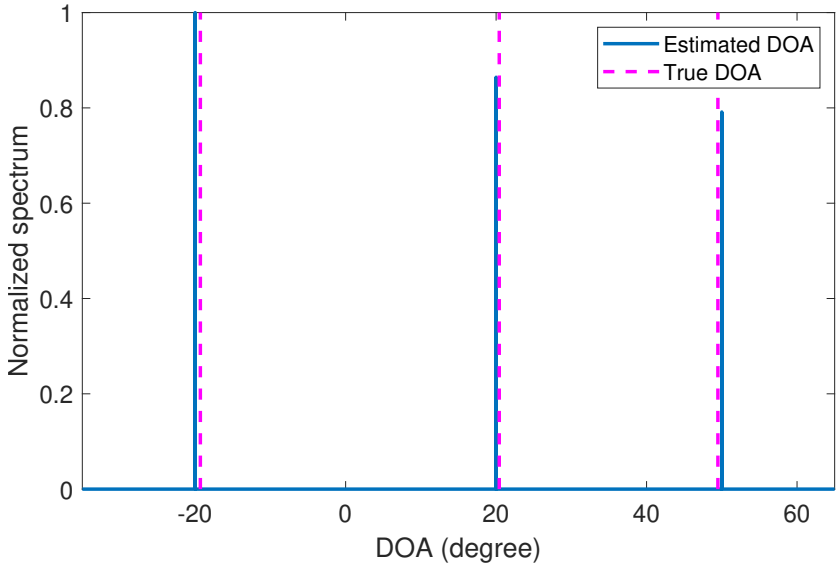

Fig. 5.2 Results by on-grid model.

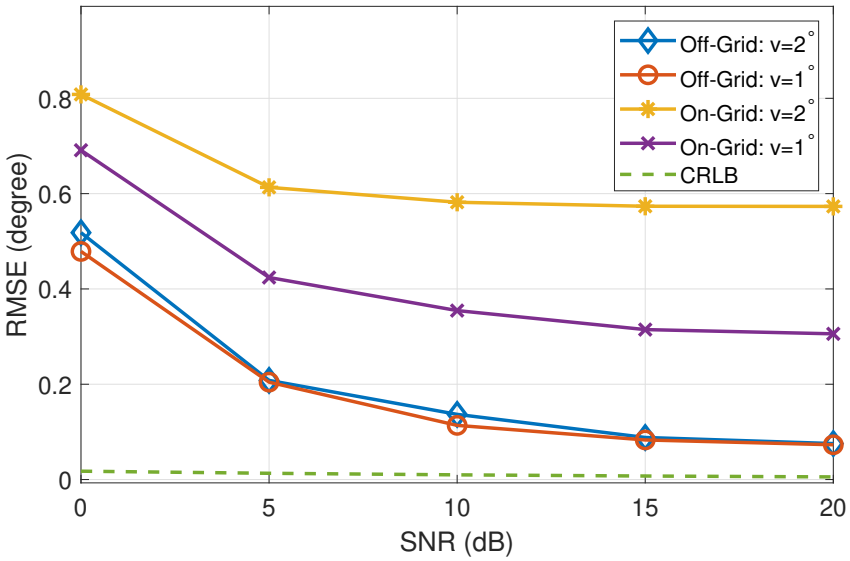

Fig. 5.3 RMSE versus SNR.

Table 5.2 Running times of off-grid and on-grid models.

Stepsize	On-grid(s)	Off-grid(s)
2°	25.54	25.56
1°	52.65	52.69

an average of 200 trials. The Cramér-Rao bound is also provided. In all trials, locations of $K = 3$ signals are defined as $[-40^\circ + u_1, 0^\circ + u_2, 30^\circ + u_3]$, where u_k is randomly generated at each run within $[-1^\circ, 1^\circ]$. The results are further parameterized by the grid stepsize v. According to Fig. 5.3, it can be observed that, although a smaller stepsize can improve the performance of both on-grid and off-grid models, the off-grid model outperforms the on-grid model even when the on-grid model has a denser grid; moreover, the improvement achieved by a denser grid for the proposed off-grid method is very small, which means the second step of the method is working effectively.

Finally, the computational complexity of both on-grid and off-grid models with different stepsizes is compared in terms of running time, and the results are shown in Table 5.2, based on a computer with 1.8GHz CPU i7-10510U and 16GB RAM. We can see that a smaller stepsize significantly increases the computation time, whereas the extra time cost by the second step of the off-grid model is minimal.

5.2 Localization with Distributed Sensor Arrays

Many methods have been proposed for source localisation based on sensor arrays, such as those based on received signal strength (RSS) [78], time of arrival (TOA) [79], time difference of arrival (TDOA)[80, 81], direct position determination (DPD) [82, 83] and angle of arriving (AOA) [84, 85].

For AOA based methods, a distributed sensor array structure is employed with multiple sensor arrays distributed in a two-dimensional (2-D) space, where synchronization among all distributed sensor arrays is not required. There are normally two steps: the first is applying existing direction of arrival methods such as those proposed in [12–14] to estimate AOAs at all distributed sensor arrays, while the second is to find intersections of those estimated AOAs in order to localize the sources [84, 85]. Recently, in [86, 87], with the distributed array network, information across all sensor arrays is jointly exploited and the source localization problem was re-formulated into a sparsity maximization problem, where the area of interest in a 2-D Cartesian system is divided into grids along the x-axis and y-axis; under such a framework, a common spatial sparsity support corresponding to all distributed sensor arrays is enforced, leading to a better estimation performance, which also avoids the possible pairing and ambiguity problems associated with a two-step AOA based solution.

In this section, based on the same distributed array structure, the non-coherent source localisation problem is studied and an off-grid algorithm is developed.

5.2.1 Signal Model with Distributed Arrays

Assume that there are K narrowband sources located at Cartesian coordinates $L_k(x_k, y_k)$, $k = 1, 2, ..., K$, impinging on D deployed sensor arrays with coordinates $C_d(x_d, y_d)$, as shown in Fig. 5.4.

The number of sensors of the d-th sensor array is M_d, and the corresponding non-coherent measurements at the d-th sensor array is expressed as

$$\mathbf{Z}_d = |\mathbf{A}_d \mathbf{S}_d| + \mathbf{N}_d, \tag{5.21}$$

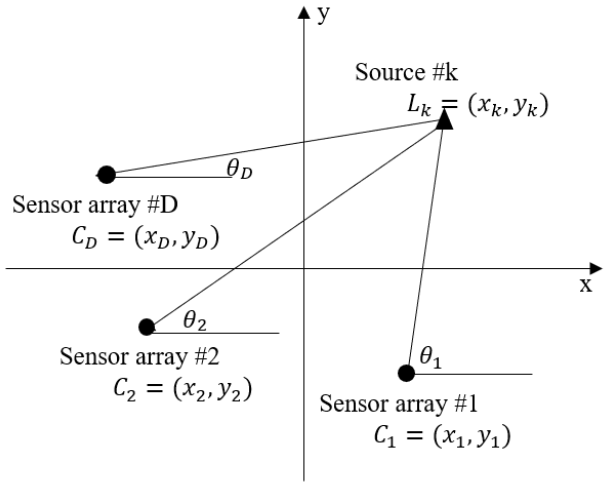

Fig. 5.4 Source localization geometry.

with $\mathbf{S}_d = [\mathbf{s}[1], ..., \mathbf{s}_d[P]]^T$ and $\mathbf{s}_d[p] = [s_{d,1}[p], ..., s_{d,K}[p]]^T$, where $s_{d,k}$ represents the p-th snapshot of the k-th signal, $\mathbf{N}_d$ is the $M_d \times P$ random Gaussian noise vector at the d-th sensor array, $|\cdot|$, and $[\cdot]^T$ are the element-wise absolute value operator and matrix transpose operator, separately, and

$$\mathbf{A}_d = [\mathbf{a}_d(\theta_1), ..., \mathbf{a}_d(\theta_K)]^T \tag{5.22}$$

is the steering matrix with its columns $\mathbf{a}(\theta_k)$, $k = 1, ..., K$, being the corresponding steering vectors. When employing a uniform circular array [88], $\mathbf{a}_{d,k}$ is given by

$$\begin{aligned} \mathbf{a}_d(\theta_k) &= [e^{-j\frac{2\pi r}{\lambda}\cos(\theta_{d,k}-\gamma_1)}, ..., e^{-j\frac{2\pi r}{\lambda}\cos(\theta_{d,k}-\gamma_{M_d})}], \\ \gamma_m &= 2\pi m/M_d,\ m = 1, ..., M_d \end{aligned} \tag{5.23}$$

where λ is wavelength of the signals, r is radius of the circular array, and $\theta_{d,k}$ denotes the arriving angle between the k-th source and d-th sensor array, expressed as

$$\begin{aligned} \theta_{d,k} &= \text{arctan2}(\Delta y_{d,k}, \Delta x_{d,k}), \\ \Delta y_{d,k} &= y_{L_k} - y_d, \\ \Delta x_{d,k} &= x_{L_k} - x_d, \end{aligned} \tag{5.24}$$

with arctan2$(\cdot)$ being the inverse tangent operator.

For D distributed arrays, the measurements can be jointly expressed as

$$\mathbf{Z} = |\mathbf{AS}| + \mathbf{N}, \;\; \mathbf{A} = \text{blkdiag}\{\mathbf{A}_1, ..., \mathbf{A}_D\}, \tag{5.25}$$

where blkdiag$\{\cdot\}$ generates a block diagonal matrix from its entries, $\mathbf{S} = [\mathbf{s}[1], ..., \mathbf{s}[P]]$, $\mathbf{s}[p] = [\mathbf{s}_1[p]^T, .., \mathbf{s}_D^T[p]]^T$, and $\mathbf{N} = [\mathbf{N}_1^T, ..., \mathbf{N}_D^T]^T$.

5.2.2 The Off-Grid Localisation Algorithm

By dividing the admissible area of interest into G_x and G_y grids along the x-axis and y-axis in the Cartesian coordinate system, separately, the overcomplete steering matrix of the d-th sensor array can be expressed as

$$\begin{aligned} \tilde{\mathbf{A}}_d =& [\mathbf{a}_d(\theta_{11}), ..., \mathbf{a}_d(\theta_{1G_y}, \\ & \mathbf{a}_d(\theta_{g_x 1}), ..., \mathbf{a}_d(\theta_{g_x G_y}), \\ & ..... \\ & \mathbf{a}_d(\theta_{G_x 1}), ..., \mathbf{a}_d(\theta_{G_x G_y})] \\ =& [\mathbf{a}(\theta_{d,1}), ..., \mathbf{a}(\theta_{d,G})], \end{aligned} \tag{5.26}$$

where $\theta_{d,g},\ g = (g_x - 1)G_x + g_y \in \{1, ..., G_x G_y\}$ is the angle between location (g_x, g_y) and the $d-th$ sensor array, obtained by

$$\theta_{d,g} = \text{arctan2}(\Delta y_{d,g_y}, \Delta x_{d,g_x}), \tag{5.27}$$

where $\Delta y_{d,g_x} = y_{g_x} - y_d$, $\Delta x_{d,g_y} = x_{g_y} - x_d$. Accordingly, the d-th array measurements (5.21) is changed to

$$\mathbf{Z}_d = |\tilde{\mathbf{A}}_d \tilde{\mathbf{S}}_d| + \mathbf{N}_d, \tag{5.28}$$

where $\tilde{\mathbf{S}}_d = [\tilde{\mathbf{s}}_d[1], ..., \tilde{\mathbf{s}}_d[P]]$ is the sparse signals matrix with the corresponding K rows being non-zero. Accordingly, a $(\sum_{d=1}^{D} M_d) \times G_x G_y$ steering matrix $\tilde{\mathbf{A}}$ covering all D sensor arrays

can be constructed and the array measurements are given by

$$\mathbf{Z} = |\tilde{\mathbf{A}}\tilde{\mathbf{S}}| + \mathbf{N}, \quad \tilde{\mathbf{A}} = \text{blkdiag}\{\tilde{\mathbf{A}}_1, ..., \tilde{\mathbf{A}}_D\}. \tag{5.29}$$

Let $\bar{\boldsymbol{x}} = [\bar{x}_1, ..., \bar{x}_K]$ and $\bar{\boldsymbol{y}} = [\bar{y}_1, ..., \bar{y}_K]$ denote the true locations of K sources and x_{g_k} and y_{g_k} represent the nearest grid point for the k-th source, and (5.28) can be approximated by the first order approximation of two variables, given by

$$\mathbf{Z}_d \approx |(\tilde{\mathbf{A}}_d + \tilde{\mathbf{B}}_{d,x}\boldsymbol{\Delta}_x + \tilde{\mathbf{B}}_{d,y}\boldsymbol{\Delta}_y)\tilde{\mathbf{S}}_d| + \mathbf{N}_d, \tag{5.30}$$

with $\mathbf{B}_{d,x} = [\mathbf{b}_x(\theta_{d,1}), ..., \mathbf{b}_x(\theta_{d,G})]$, $\mathbf{b}_x(\theta_{d,g}) = \frac{\partial \mathbf{a}(\theta_{d,g})}{\partial x_g}$, $\boldsymbol{\Delta}_x = \text{diag}(\boldsymbol{\beta}_x)$ and $\boldsymbol{\beta}_x = [\beta_{1,x}, ..., \beta_{G,x}]$, where

$$\beta_{g,x} = \begin{cases} \bar{x}_k - x_{g_x}, & \text{if } g = g_k, \\ 0, & \text{otherwise.} \end{cases} \tag{5.31}$$

Similarly, we have $\tilde{\mathbf{B}}_{d,y} = [\mathbf{b}_y(\theta_{d,1}), ..., \mathbf{b}_y(\theta_{d,G})]$, $\mathbf{b}_y(\theta_{d,g}) = \frac{\partial \mathbf{a}(\theta_{d,g})}{\partial y_g}$, $\boldsymbol{\Delta}_y = \text{diag}(\boldsymbol{\beta}_y)$ and $\boldsymbol{\beta}_y = [\beta_{1,y}, ..., \beta_{G,y}]$, where

$$\beta_{g,y} = \begin{cases} \bar{y}_k - x_{g_y}, & \text{if } g = g_k, \\ 0, & \text{otherwise.} \end{cases} \tag{5.32}$$

$\beta_{g,x}$ and $\beta_{g,y}$ satisfy $-\frac{v_x}{2} \leq \beta_{g,x} \leq \frac{v_x}{2}$ and $-\frac{v_y}{2} \leq \beta_{g,y} \leq \frac{v_y}{2}$, separately, where v_x and v_y are grid stepsizes with respect x-axis and y-axis, respectively.

It is noted that, incident sources from an arbitrary grid point in the Cartesian coordinate system would share the same spatial support of $\tilde{\mathbf{A}}_d$, $d = 1, ..., D$, although the arriving angles with respect to different arrays are different. Thus, a $(\sum_{d=1}^{D} M_d) \times G_x G_y$ steering matrix covering all D sensor arrays can be constructed as

$$\tilde{\mathbf{A}} = \text{blkdiag}\{\tilde{\mathbf{A}}_1, ..., \tilde{\mathbf{A}}_D\}, \tag{5.33}$$

Therefore, the source localization problem can be formulated as a joint group sparsity based optimization problem, given by

$$\min_{\tilde{\mathbf{S}},\boldsymbol{\beta}_x,\boldsymbol{\beta}_y} \|\mathbf{Z} - |(\tilde{\mathbf{A}} + \tilde{\mathbf{B}}_x\tilde{\boldsymbol{\Delta}}_x + \tilde{\mathbf{B}}_y\tilde{\boldsymbol{\Delta}}_y)\tilde{\mathbf{S}}|\|_F^2 + \rho\|\tilde{\mathbf{S}}\|_{2,1}, \tag{5.34}$$

where

$$\begin{aligned}
\tilde{\mathbf{B}}_x &= \text{blkdiag}\{\tilde{\mathbf{B}}_{1,x}, ..., \tilde{\mathbf{B}}_{D,x}\}, \\
\tilde{\mathbf{B}}_y &= \text{blkdiag}\{\tilde{\mathbf{B}}_{1,y}, ..., \tilde{\mathbf{B}}_{D,y}\}, \\
\tilde{\boldsymbol{\Delta}}_x &= \text{blkdiag}\{\boldsymbol{\Delta}_x, ..., \boldsymbol{\Delta}_x\}, \\
\tilde{\boldsymbol{\Delta}}_y &= \text{blkdiag}\{\boldsymbol{\Delta}_y, ..., \boldsymbol{\Delta}_y\},
\end{aligned} \tag{5.35}$$

with $\|\cdot\|_{2,1}$ and $\|\cdot\|_F$ represent $l_{2,1}$ norm and Frobenius norm, respectively. The $l_{2,1}$ norm $\|\cdot\|_{2,1}$ is defined as

$$\|\tilde{\mathbf{S}}\|_{2,1} := \sum_{g=1}^{G} \|\mathbf{s}_g\|_2, \tag{5.36}$$

with $\mathbf{s}_g$ being the g-th row vector of $\tilde{\mathbf{S}}$. In addition to the support shared in the temporal domain, groups of $\tilde{\mathbf{S}}$ also share the same support in spatial domain. As a result, $\tilde{\mathbf{S}}$ contains $G = G_x G_y$ groups and the g-th group, $g \in \{1, ..., G\}$, of $\tilde{\mathbf{S}}$ is a $1 \times DP$ vector, consisting of g-th row vectors of all $\tilde{\mathbf{S}}_d$, $d \in \{1, .., D\}$ in $\tilde{\mathbf{S}}$.

First, for the on-grid solution, i.e. the off-grid biases $\tilde{\boldsymbol{\Delta}}_x$ and $\tilde{\boldsymbol{\Delta}}_y$ are assumed to be zero, and the corresponding optimization problem in (5.34) is simplified to

$$\min_{\tilde{\mathbf{S}}} \|\mathbf{Z} - |\tilde{\mathbf{A}}\tilde{\mathbf{S}}|\|_F^2 + \rho\|\tilde{\mathbf{S}}\|_{2,1}. \tag{5.37}$$

The above formulation has the same form as those considered in group sparsity based phase retrieval problem for DOA estimation, which can be solved by existing algorithms such as the modified Gespar [16] and ToyBar [49].

For the general off-grid case, instead of jointly estimate $\tilde{\boldsymbol{\Delta}}_x$, $\tilde{\boldsymbol{\Delta}}_y$ and $\tilde{\mathbf{S}}$ in (5.34), this problem is solved iteratively. In the first step, we employ (5.37) to find the rough grid locations of targets. In the second step, in order to estimate the off-grid bias, the PRIME

technique [48] is employed column by column to (5.34), its first term can be replaced by a convex surrogate, and the corresponding objective function is changed to

$$\min_{\boldsymbol{\beta}_x,\boldsymbol{\beta}_y} \|(\tilde{\mathbf{A}}+\tilde{\mathbf{B}}_{d,x}\tilde{\boldsymbol{\Delta}}_x+\tilde{\mathbf{B}}_{d,y}\tilde{\boldsymbol{\Delta}}_y)\tilde{\mathbf{S}}-\bar{\mathbf{C}}\|_F^2+\rho\|\tilde{\mathbf{S}}\|_{2,1}, \tag{5.38}$$

with

$$\bar{\mathbf{C}}=\mathbf{Z}\odot e^{j\arg(\tilde{\mathbf{A}}\tilde{\mathbf{S}}_e)}, \tag{5.39}$$

where $\odot$ is the Hadamard product, $\arg(\cdot)$ represents the phase of its variable applied element-wise, and $\tilde{\mathbf{S}}_e$ is estimated signals from step one, which is susceptible to global phase ambiguity.

After that, an iterative algorithm for estimating dictionary bias $\tilde{\boldsymbol{\beta}}$ is proposed. This method first estimates K non-zero rows of estimated signals $\tilde{\mathbf{S}}_K^i$ as

$$\bar{\boldsymbol{S}}_K^i=(\bar{\boldsymbol{A}}_K^i)^\dagger\bar{\mathbf{C}}, \tag{5.40}$$

where $(\cdot)^\dagger$ is the pseudo-inverse operator, $i\in\{1,...,I\}$ is iteration index, $\bar{\boldsymbol{A}}_K^i$ is the steering matrix with K columns corresponding the estimated source locations, given by

$$\begin{aligned}\bar{\mathbf{A}}_K^i&=\text{blkdiag}\{\bar{\mathbf{A}}_{1,K}^i,...,\bar{\mathbf{A}}_{D,K}^i\},\\ \bar{\mathbf{A}}_{d,K}^i&=[\mathbf{a}(\theta_{d,1}^i),...,\mathbf{a}(\theta_{d,K}^i)],\end{aligned} \tag{5.41}$$

and $\theta_{d,K}^i$ is updated with x^i and y_i obtained from the previous iteration. x^0 and y^0 is initialized as K columns of $\tilde{\mathbf{A}}_d$, which corresponds to locations of estimated sources $\tilde{\mathbf{S}}_e$. As the biases $\tilde{\boldsymbol{\beta}}_x$ and $\tilde{\boldsymbol{\beta}}_y$ share the same support with $\tilde{\mathbf{S}}_e$, $\bar{\mathbf{B}}_{d,x}$ and $\bar{\mathbf{B}}_{d,y}$ are obtained, which are the sub-matrix of $\tilde{\mathbf{B}}_{d,x}$ and $\tilde{\mathbf{B}}_{d,y}$. Similarly, the biases of corresponding source locations $\bar{\boldsymbol{\Delta}}_{K,x}^i=\text{diag}(\bar{\boldsymbol{\beta}}_x^i)=[\beta_{1,x}^i,...\beta_{K,x}^i]^T$ and $\bar{\boldsymbol{\Delta}}_{K,y}^i=\text{diag}(\bar{\boldsymbol{\beta}}_y^i)=[\beta_{1,y}^i,...\beta_{K,y}^i]^T$ are obtained.

By denoting $\bar{\mathbf{B}}_x^i=\text{blkdiag}\{\mathbf{B}_{1,x}^i,...,\mathbf{B}_{D,x}^i\}$, $\bar{\mathbf{B}}_y^i=\text{blkdiag}\{\mathbf{B}_{1,y}^i,...,\mathbf{B}_{D,y}^i\}$,

$\bar{\mathbf{\Delta}}_x^i = \text{blkdiag}\{\bar{\mathbf{\Delta}}_{K,x}^i, ..., \bar{\mathbf{\Delta}}_{K,x}^i\}$, and $\bar{\mathbf{\Delta}}_y^i = \text{blkdiag}\{\bar{\mathbf{\Delta}}_{K,y}^i, ..., \bar{\mathbf{\Delta}}_{K,y}^i\}$, the off-grid biases can be estimated by solving

$$\min_{\bar{\boldsymbol{\beta}}_x, \bar{\boldsymbol{\beta}}_y} \|(\bar{\mathbf{A}}_K^i + \bar{\mathbf{B}}_x^i \bar{\mathbf{\Delta}}_x^i + \bar{\mathbf{B}}_{d,y}^i \bar{\mathbf{\Delta}}_y^i)\bar{\mathbf{S}}_K^i - \bar{\mathbf{C}}\|_F^2. \tag{5.42}$$

Once the PRIME technique is done, this process updates each off-grid bias $\bar{\boldsymbol{\beta}}_x$ and $\bar{\boldsymbol{\beta}}_y$ in (5.42) at a time.

Firstly, with $\bar{\beta}_y^i$ fixed to zero, $\bar{\beta}_x^i$ is pursued by solving

$$\min_{\bar{\boldsymbol{\beta}}_x} \|(\bar{\mathbf{A}}_K^i + \bar{\mathbf{B}}_x^i \bar{\mathbf{\Delta}}_x^i)\bar{\mathbf{S}}_K^i - \bar{\mathbf{C}}_d\|_F^2. \tag{5.43}$$

Since $\bar{\mathbf{A}}_K^i$ and $\bar{\mathbf{B}}_x^i$ are block diagonal, (5.43) can be reformulated as

$$\min_{\bar{\boldsymbol{\beta}}_x} \sum_{d=1}^{D} \|\|(\bar{\mathbf{A}}_{d,K}^i + \bar{\mathbf{B}}_{d,x}^i \bar{\mathbf{\Delta}}_x^i)\bar{\mathbf{S}}_{d,K}^i - \bar{\mathbf{C}}_d\|_F^2, \tag{5.44}$$

where $\mathbf{C}_d$ and $\bar{\mathbf{S}}_{d,K}^i$ are the approximated measurements and estimated signals of the d-th subarray. Dropping index i for simplicity, (5.44) can be approximated as [88, 77, 73]

$$\begin{aligned} &\sum_{d=1}^{D} \|(\bar{\mathbf{A}}_{d,K} + \bar{\mathbf{B}}_{d,x}\bar{\mathbf{\Delta}}_K)\bar{\mathbf{S}}_{d,K} - \bar{\mathbf{C}}_d\|_F^2 \\ &\quad \approx \sum_{d=1}^{D} \Big\{ \bar{\boldsymbol{\beta}}_x^T \big(\bar{\mathbf{B}}_{d,x}^H \bar{\mathbf{B}}_{d,x} \odot (\bar{\mathbf{S}}_{d,K}\bar{\mathbf{S}}_{d,K}^H)^*\big)\bar{\boldsymbol{\beta}}_x \\ &\quad - 2\text{Re}\{\text{diag}[\bar{\mathbf{S}}_{d,K}(\bar{\mathbf{C}}_d - \bar{\mathbf{A}}_K\bar{\mathbf{S}}_{d,K})^H \bar{\mathbf{B}}_{d,x}]\bar{\boldsymbol{\beta}}_x\}\Big\}, \end{aligned} \tag{5.45}$$

where $\text{tr}(\cdot)$ and $\text{Re}(\cdot)$ represent the trace and real part of its variable, separately. While the optimal condition, $\bar{\boldsymbol{\beta}}_x^i$ can be obtained by

$$\begin{aligned} &\bar{\boldsymbol{\beta}}_x^{i+1} = \text{Re}\{(\mathbf{J}_x^i)^{-1}\mathbf{h}^i\}, \mathbf{J}_x^i = \sum_{d=1}^{D} \mathbf{J}_{d,x}^i,\ \mathbf{h}_x = \sum_{d=1}^{D} \mathbf{h}_{d,x}^i, \\ &\mathbf{J}_{d,x}^i = (\mathbf{B}_{d,x}^i)^H \bar{\mathbf{B}}_{d,x}^i \odot (\bar{\mathbf{S}}_{d,K}^i \bar{\mathbf{S}}_{d,K}^i)^*, \\ &\mathbf{h}_{d,x}^i = \big\{\text{diag}[\bar{\mathbf{S}}_{d,K}^i(\bar{\mathbf{C}}_d - \bar{\mathbf{A}}_{d,K}^i \bar{\mathbf{S}}_{d,K}^i)^H \bar{\mathbf{B}}_{d,x}^i]\big\}^T. \end{aligned} \tag{5.46}$$

where $(\cdot)^{-1}$ is the inverse operator. While the off-grid bias with respect to x-axis is fixed, the off-grid bias of the y-axis $\boldsymbol{\beta}_y$ can be obtained by

$$\min_{\bar{\boldsymbol{\beta}}_y} \sum_{d=1}^{D} \|(\bar{\mathbf{A}}^i_{d,K} + \bar{\mathbf{B}}^i_{d,x}\bar{\boldsymbol{\Delta}}^i_x + \bar{\mathbf{B}}^i_{d,y}\bar{\boldsymbol{\Delta}}^i_y)\bar{\mathbf{S}}^i_{d,K} - \bar{\mathbf{C}}_d\|^2_F. \tag{5.47}$$

Similarly, we have

$$\begin{aligned}
\bar{\boldsymbol{\beta}}^i_y &= \mathrm{Re}\{(\mathbf{J}^i_y)^{-1}\mathbf{h}^i_y\}, \mathbf{J}^i_y = \sum_{d=1}^{D} \mathbf{J}^i_{d,y},\ \mathbf{h}^i_y = \sum_{d=1}^{D} \mathbf{h}^i_{d,y}, \\
\mathbf{J}^i_{d,y} &= (\mathbf{B}^i_{d,y})^H \bar{\mathbf{B}}^i_{d,y} \odot (\bar{\mathbf{S}}^i_{d,K}\bar{\mathbf{S}}^i_{d,K})^*, \\
\mathbf{h}^i_{d,y} &= \left\{\mathrm{diag}[\bar{\mathbf{S}}^i_{d,K}(\bar{\mathbf{C}}_d - (\bar{\mathbf{A}}^i_{d,K} + \mathbf{B}^{i+1}_{d,x}\bar{\boldsymbol{\Delta}}^{i+1}_x)\bar{\mathbf{S}}^i_{d,K})^H \bar{\mathbf{B}}^i_{d,y}]\right\}^T.
\end{aligned} \tag{5.48}$$

Note that, the non-coherent DOA estimation results still suffer from the global phase ambiguity, that is

$$\begin{aligned}
\bar{\mathbf{C}} &= \mathbf{Z} \odot e^{j\arg(\tilde{\mathbf{A}}\tilde{S}_e)} \approx \mathbf{A}_r \mathbf{S}_r e^{j\phi}, \\
\bar{\mathbf{S}}_K &= (\bar{\boldsymbol{A}}^i_K)^\dagger \bar{\mathbf{C}} \approx \mathbf{S}_r e^{j\phi},
\end{aligned} \tag{5.49}$$

where $\mathbf{S}_r$ and $\mathbf{A}_r$ represent the real signal and its corresponding real steering matrix, respectively, and ϕ is a global phase factor. It can be seen that, when substituting (5.49) into (5.46) and (5.48), the global phase factor cancels, which means that the global phase ambiguity will not affect bias estimation in this step.

With $\bar{\boldsymbol{\beta}}^i_x$ and $\bar{\boldsymbol{\beta}}^i_y$, the steering matrix $\mathbf{A}_{d,K}$ is updated as

$$x^{i+1}_{d,k} = x^i_{d,k} + \beta^i_{k,x},\ y^{i+1}_{d,k} = y^i_{d,k} + \beta^i_{k,y}, \tag{5.50}$$

where $\beta_{k,x}$ and $\beta_{k,y}$ represent the bias of the k-th source, $x^0_{d,k}$ and $y^0_{d,k}$ are the initial locations obtained from the first step, i.e corresponding locations of $\tilde{\boldsymbol{S}}_e$. Finally, the estimated locations of the k-th source can be obtained after I iterations.

The full algorithm is summarized in the Algorithm Summary table.

Algorithm Summary (Two-Step Off-Grid)
Input: $\tilde{\mathbf{A}}$, $\mathbf{Z}$,
Initializtion: $\bar{\boldsymbol{\beta}}_x^0 = \mathbf{0}$, $\bar{\boldsymbol{\beta}}_y^0 = \mathbf{0}$.
Step 1: Estimate $\tilde{\mathbf{S}}_e$ via existing group sparse phase retrieval algorithms. Obtain $\bar{\boldsymbol{A}}_K^0$, $\mathbf{x}^0$ and $\mathbf{y}^0$. Calculate $\bar{\mathbf{C}} = \mathbf{Z} \odot e^{j\arg(\tilde{\mathbf{A}}\tilde{\mathbf{S}}_e)}$.
Step 2: for i=1, ..., I
1) Calculate $\bar{\mathbf{S}}_K^i = (\bar{\boldsymbol{A}}_K^i)^\dagger \bar{\mathbf{C}}$.
2) Calculate $\bar{\boldsymbol{\beta}}_x^i = \mathrm{Re}\{(\mathbf{J}_x^i)^{-1}\mathbf{h}^i\}$ from (5.46),
3) Restrict elements of $\bar{\boldsymbol{\beta}}_x^i$ within range $[-\frac{v_x}{2}, \frac{v_x}{2}]$.
4) Calculate $\bar{\boldsymbol{\beta}}_y^i = \mathrm{Re}\{(\mathbf{J}_y^i)^{-1}\mathbf{h}^i\}$ from (5.48),
5) Restrict elements of $\bar{\boldsymbol{\beta}}_y^i$ within range $[-\frac{v_y}{2}, \frac{v_y}{2}]$.
6) Calculate $\mathbf{x}^{i+1} = \boldsymbol{x}^i + \boldsymbol{\beta}_x^i$, $\mathbf{y}^{i+1} = \boldsymbol{y}^i + \boldsymbol{\beta}_y^i$,
7) $\bar{\mathbf{A}}_{d,K}^{i+1} = \bar{\mathbf{A}}_K(\boldsymbol{\theta}_d^{i+1})$.
Output localization results: $\mathbf{x}^i$, $\mathbf{y}^i$.

5.2.3 Grid refinement

Instead of off-grid methods, the estimation results can be updated by refining the grid size, where a coarse grid is firstly made; based on the localization results, a denser steering matrix is then built around the estimated locations of incident sources, and the algorithm is employed again to find a more accurate result.

5.2.4 Cramér-Rao Bound

In this part, we derive the Cramér-Rao bound (CRB).

From (5.25), the probability density function is expressed as

$$p(\mathbf{Z};\boldsymbol{\Phi}) = \prod_{p=1}^{P}\prod_{m=1}^{M} \frac{1}{2\pi\sigma^2} e^{(z_m[p]-|\mathbf{a}_m\mathbf{s}[p]|)^2/2\sigma^2}, \tag{5.51}$$

where $M = \sum_{d=1}^{D} M_d$, $\mathbf{a}_m$ is the m-th row of $\mathbf{A}$, $z_m[p]$ represent the m-th entry of $\mathbf{Z}$ at the p-th snapshot.

Since the reconstructed signals are up to a global phase factor, for complex signal $\mathbf{s}$, the Fisher information matrix (FIM) would be singular [67]. Thus, similar to [49], instead of estimating the phase information of signals, only phase differences between signals are considered. Assuming the noise level at all distributed sensor arrays are identical, the unknown parameter vector of arriving angles, magnitude, phase difference and noise level can be represented as

$$\begin{aligned}
\boldsymbol{\Phi} &= [\boldsymbol{L}_x^T, \boldsymbol{L}_y^T, |\boldsymbol{s}[p]|, \boldsymbol{\Delta\gamma}[p], \sigma^2]^T \\
\boldsymbol{L}_x &= [x_1, ..., x_K]^T,\ \boldsymbol{L}_y = [y_1, ..., y_K]^T, \\
|\boldsymbol{s}[p]| &= [|\boldsymbol{s}_1^T[p]|, ..., |\boldsymbol{s}_D^T[p]|]^T, \\
\boldsymbol{\Delta\gamma}[p] &= [\boldsymbol{\Delta\gamma}_1^T[p], ..., \boldsymbol{\Delta\gamma}_D^T[p]]^T, \\
\boldsymbol{\Delta\gamma}_d[p] &= [\Delta\gamma_{12,d}[p], \Delta\gamma_{13,d}[p], ..., \Delta\gamma_{(K-1)K,d}[p]]^T,
\end{aligned} \tag{5.52}$$

where $\boldsymbol{\Delta\gamma_d}[p]$ contains $(K^2-K)/2$ entries, $\Delta\gamma_{kk',d}[p] = \gamma_{k,d}[p] - \gamma_{k',d}[p]$, $\gamma_{k,d}[p]$ is the phase of the k-th signals of the d-th sensor array at the p-th snapshot and σ^2 is noise power.

For deterministic model, the Fisher Information Matrix (FIM) $\mathbf{F}$ is defined as

$$\mathbf{F} = \mathbb{E}\{\frac{\partial \ln^2 p(\mathbf{Z};\boldsymbol{\Phi})}{\partial\boldsymbol{\Phi}\partial\boldsymbol{\Phi}^T}\} \tag{5.53}$$

The $\{i,j\}$-th entry of the FIM $\mathbf{F}$ is given by [70]

$$\begin{aligned}
\mathbf{F}_{i,j} = &\Big[\frac{\partial\boldsymbol{\mu}(\boldsymbol{\Phi})}{\partial\Phi_i}\Big]^T\boldsymbol{\Gamma}^{-1}(\boldsymbol{\Phi})\Big[\frac{\partial\boldsymbol{\mu}(\boldsymbol{\Phi})}{\partial\Phi_j}\Big] \\
&+\frac{1}{2}\Big[\boldsymbol{\Gamma}^{-1}(\boldsymbol{\beta})\frac{\partial\boldsymbol{\Gamma}^{-1}(\boldsymbol{\Phi})}{\partial\Phi_i}\boldsymbol{\Gamma}^{-1}(\boldsymbol{\Phi})\frac{\partial\boldsymbol{\Gamma}^{-1}(\boldsymbol{\Phi})}{\partial\Phi_j}\Big],
\end{aligned} \tag{5.54}$$

where $\boldsymbol{\Gamma}^{-1}(\boldsymbol{\Phi}) = \frac{1}{\sigma^2}\mathbf{I}_M$, $\mathbf{I}_M$ is the identity matrix, $(\cdot)^{-1}$ is the matrix inverse operator, and $\boldsymbol{\mu}(\boldsymbol{\Phi}) = |\mathbf{AS}|$. Since $\boldsymbol{\mu(\Phi)}$ is independent with the noise level, we have

$$\mathbf{F} = \begin{bmatrix}\tilde{\mathbf{F}} & \mathbf{0}\\ \mathbf{0} & \mathbf{0}\end{bmatrix} + \begin{bmatrix}\mathbf{0} & \mathbf{0}\\ \mathbf{0} & \mathbf{F}_\sigma\end{bmatrix}, \tag{5.55}$$

As the FIM is block diagonal, $\mathbf{F}_\sigma$ has no effect on the Cramér-Rao bound (CRB) result of DOAs. Thus, CRB of DOAs can be determined by the inverse of $\tilde{\mathbf{F}}$. Computing the derivatives of $\boldsymbol{\mu}(\boldsymbol{\Phi})$ with respect to $\boldsymbol{\Phi}$, we have

$$\mathbf{D} = \frac{\partial \boldsymbol{\mu}(\boldsymbol{\Phi})}{\partial \boldsymbol{\Phi}^T} = [\mathbf{G}, \mathbf{H}, \boldsymbol{\Delta}, \mathbf{0}], \tag{5.56}$$

Denotes $|\mathbf{a}_m \mathbf{s}| = (\mathbf{s}^H \mathbf{a}_m^H \mathbf{a}_m \mathbf{s})^{\frac{1}{2}} = (\mathbf{s}^H \mathbf{A}_m \mathbf{s})^{\frac{1}{2}}$ and drop index p for convenience, the first block of $\mathbf{C}$ is

$$\begin{aligned}
\mathbf{G} &= [\mathbf{G}_{1,x}^T, ..., \mathbf{G}_{D,x}^T, \mathbf{G}_{1,y}^T, ..., \mathbf{G}_{D,y}^T]^T, \\
\mathbf{G}_{d,x} &= [\mathbf{g}_{d,1,x}^T, ..., \mathbf{g}_{d,M_d,x}^T]^T, \\
\mathbf{G}_{d,y} &= [\mathbf{g}_{d,1,y}^T, ..., \mathbf{g}_{d,M_d,y}^T]^T, \\
\mathbf{g}_{d,m,x} &= [\frac{\partial |\mathbf{a}_{m,d} \mathbf{s}_d|}{\partial x_1}, ..., \frac{\partial |\mathbf{a}_{m,d} \mathbf{s}_d|}{\partial x_K}], \\
\mathbf{g}_{d,m,y} &= [\frac{\partial |\mathbf{a}_{m,d} \mathbf{s}_d|}{\partial y_1}, ..., \frac{\partial |\mathbf{a}_{m,d} \mathbf{s}_d|}{\partial y_K}],
\end{aligned} \tag{5.57}$$

with

$$\begin{aligned}
\frac{\partial |\mathbf{a}_{m,d} \mathbf{s}_d|}{\partial x_k} &= \alpha_{d,k} \mathrm{Im}\Big(\xi \sin(\theta_{d,k} - \gamma_m) s_{d,k}^* \mathbf{A}_{m,d}(k,:)\mathbf{s}\Big), \\
\alpha_{d,k} &= (\mathbf{s}^H \mathbf{A}_{m,d} \mathbf{s})^{-\frac{1}{2}} \frac{-\Delta y_{d,k}}{\Delta x_{d,k}^2 + \Delta y_{d,k}^2}, \xi = 2\pi r/\lambda, \\
\frac{\partial |\mathbf{a}_{m,d} \mathbf{s}_d|}{\partial y_k} &= \beta_{d,k} \mathrm{Im}\Big(\xi \sin(\theta_{d,k} - \gamma_m) s_{d,k}^* \mathbf{A}_{m,d}(k,:)\mathbf{s}\Big), \\
\beta_{d,k} &= (\mathbf{s}^H \mathbf{A}_{m,d} \mathbf{s})^{-\frac{1}{2}} \frac{\Delta x_{d,k}}{\Delta x_{d,k}^2 + \Delta y_{d,k}^2},
\end{aligned} \tag{5.58}$$

where $(\cdot)^*$ is the complex conjugate operator, $\mathbf{A}_{m,d}(k,:)$ is the k-th row of $\mathbf{A}_{m,d}$ and $\mathbf{A}_{m,d}(:,k)$ is the k-th column of $\mathbf{A}_{m,d}$. The second block is expressed by

$$\begin{aligned}
\mathbf{H} &= \frac{\partial |\mathbf{A}\mathbf{s}|}{\partial |\mathbf{s}^T|} = \mathrm{blkdiag}\{\mathbf{H}_1, ..., \mathbf{H}_D\}, \\
\mathbf{H}_d^T &= \mathrm{Re}\Big(\mathrm{diag}(e^{-j\boldsymbol{\gamma}_d}) \mathbf{A}_d^H \mathrm{diag}(\mathbf{A}_d \mathbf{s}_d)]\Big) \tilde{\mathbf{z}}_d, \\
\tilde{\mathbf{z}}_d &= \mathrm{diag}\{|\mathbf{A}_d \mathbf{s}_d|\}^{-\frac{1}{2}}.
\end{aligned} \tag{5.59}$$

Then, the third block is given by

$$
\begin{aligned}
\boldsymbol{\Delta} &= \frac{\partial|\mathbf{A}\mathbf{s}|}{\partial|\Delta\boldsymbol{\gamma}^T|} = \text{blkdiag}\{\boldsymbol{\Delta}_1, ..., \boldsymbol{\Delta}_D\}, \\
\boldsymbol{\Delta}_d^T &= -\text{Im}\Big(\text{diag}\{\dot{\mathbf{s}}_d\}\dot{\mathbf{A}}_d \odot \text{diag}\{\ddot{\mathbf{s}}_d\}\ddot{\mathbf{A}}_d\Big)\tilde{\mathbf{z}}_d, \\
\dot{\mathbf{s}}_d &= \big[\overbrace{s_{d,1}, ..., s_{d,1}}^{K-1}, \overbrace{s_{d,2} ..., s_{d,2}}^{K-2}, ..., s_{d,K-1}\big], \\
\dot{\mathbf{A}}_d &= [\overbrace{\mathbf{A}(:,1)_d^T, ..., \mathbf{A}(:,1)_d^T}^{K-1}, ..., \mathbf{A}(:,K-1)_d^T], \\
\ddot{\mathbf{s}} &= \big[s_{d,2}^*, ..., s_{d,K}^*, s_{d,3}^*, ..., s_{d,K}^*, ..., s_{d,K}^*\big], \\
\ddot{\mathbf{A}} &= [\mathbf{A}(:,2)_d^H, ..., \mathbf{A}(:,K)_d^H, ..., \mathbf{A}(:,K)_d^H],
\end{aligned}
\tag{5.60}
$$

where $\odot$ stands for the Hadamard product.

Then, $\tilde{\mathbf{F}}$ can be given by

$$
\tilde{\mathbf{F}} = \sum_{p=1}^{P} \frac{1}{\sigma^2} \mathbf{D}[p]^H \mathbf{D}[p]. \tag{5.61}
$$

The CRB associated with locations of signals can be obtained by the inverse FIM $\tilde{\mathbf{F}}$.

5.2.5 Simulation Results

In this section, simulation results are provided to show the performance of the proposed on-grid and off-grid non-coherent source localization methods in comparison with the existing sparsity based on-grid method with coherent measurements [86]. For on-grid methods, when grid refinement is employed, it is referred to as the refinement method, while for the off-grid method, the iteration number for the second step is 20. ToyBar is applied in the non-coherent scenario, and the number of iterations before stop is set to 300, with 30 random initialisations used in order to find the global minimum of the phase retrieval problem.

The area of interest is set as $[-20, 20]$m (metres) along both x-axis and y-axis. In the initial step for both on-grid and off-grid methods, 2m is used as the stepsize for constructing the overcomplete steering matrix $\tilde{\mathbf{A}}$. In the refinement step, a new grid with stepsize 0.2m is formed around a distance of 1m to either side of the estimated location from the initial step. There are $D = 4$ distributed sensor arrays placed at $C_1 = (10, 40)$m, $C_2 = (30, 10)$m, $C_3 = (-80, 90)$m and $C_4 = (-20, 40)$m, while the off-grid locations for $K = 2$ sources are

$L_1 = (-10.5, -9.5)$m and $L_2 = (0.5, 12.5)$m. The number of sensors at each distributed sensor array M_d is set as 20, while the radius r of the UCAs is set as $r = \frac{M_d \frac{\lambda}{2}}{2\pi}$, and $P = 100$ snapshots are collected unless specified otherwise.

For the first set of simulations, the signal to noise ratio (SNR) is 20 dB. The spatial spectrum of the proposed non-coherent localization results as shown in Fig. 5.5 provides the result of the on-grid step, while Fig. 5.6 is for the extra off-grid step. It can be seen that the two sources have been identified successfully, but the off-grid step significantly increases the accuracy.

Next, performances of the three methods are evaluated with different SNR values ranging from 0 dB to 20 dB in terms of the root mean square error (RMSE) in the absence of phase error. The results are shown in Fig. 5.7, with each point obtained by averaging over 100 trials. It can be observed that, although all methods achieve more accurate results with increasing SNR, the method with full coherent measurements consistently outperforms those with magnitude-only measurements, especially when the noise level is high. This is not surprising since only magnitude information is used in the non-coherent scenario with magnitude-only measurements. In addition, under the non-coherent scenario, the proposed off-grid method has a better performance than the grid-refinement method and the one-step on-grid method.

Then, we examine the performance of both non-coherent and coherent methods in the presence of sensor phase errors. The array measurements with phase error is modelled as $\mathbf{Z}_d = |\mathbf{E}_d \mathbf{A}_d \mathbf{S}_d| + \mathbf{N}_d$, where $\mathbf{E}_d$ is an $M_d \times M_d$ diagonal matrix with each entry being unit complex variable with a random phase term generated independently from the Gaussian distribution with standard derivation σ, representing the phase errors at the d-th array. RMSE results are obtained with an average of 100 trials and the SNR is fixed at 20 dB. As shown in the Fig. 5.8, the proposed non-coherent method is not affected by phase errors, with a steady performance, while the performance of the coherent method declines as the intensity of phase errors increases.

To evaluate the performance for different number of snapshots, the RMSE results of off-grid non-coherent method and coherent refinement method with phase error $\sigma = 0$ and $\sigma = 0.2$ is presented in Fig. 5.9. The SNR is set to be 20 dB, while the number of snapshots

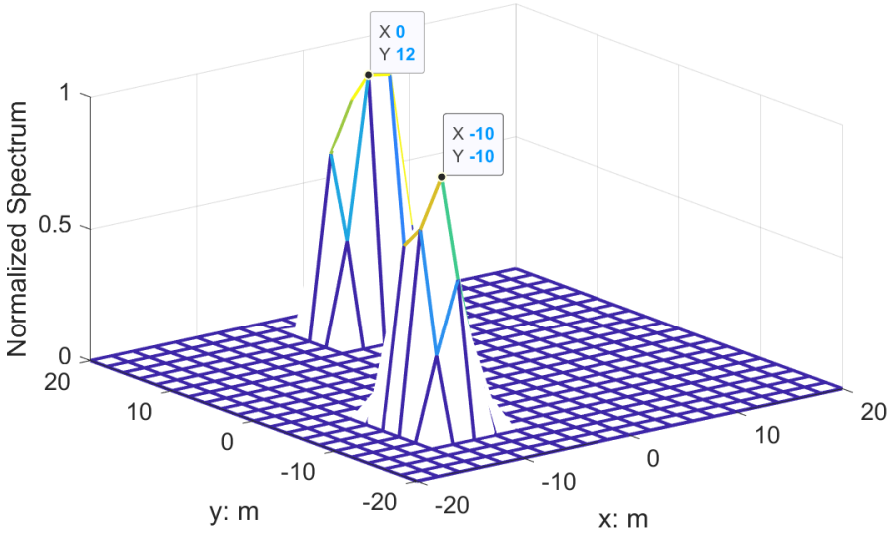

Fig. 5.5 Results by off-grid model.

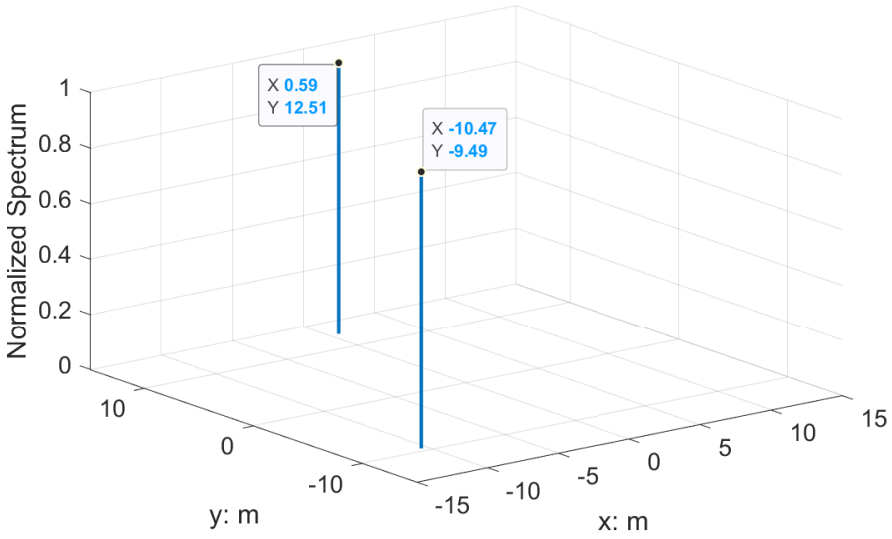

Fig. 5.6 Results by on-grid model.

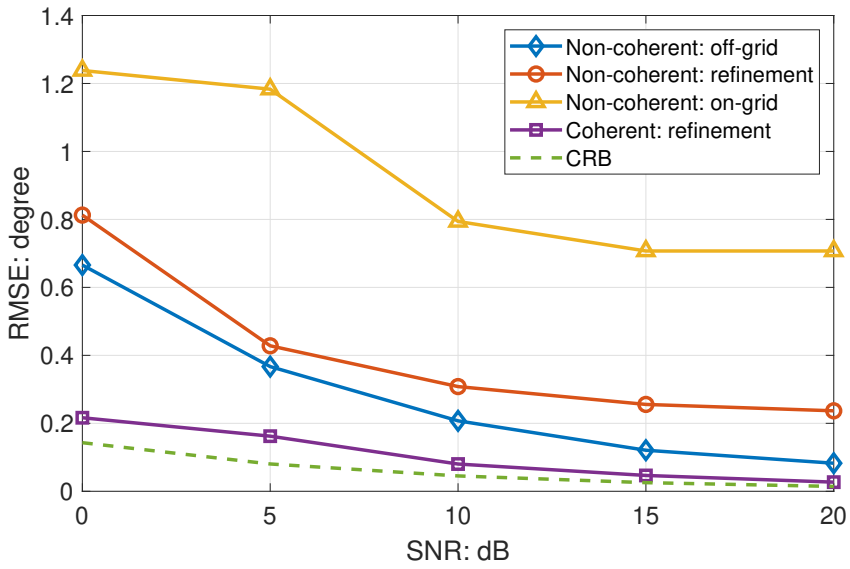

Fig. 5.7 RMSEs versus SNRs.

ranges from 100 to 200. Clearly, a larger number of snapshots yield more accurate results and the coherent method consistently outperforms the non-coherent one in the absence of phase errors. However, in the presence of phase errors, the coherent method suffers from a much larger RMSE.

Finally, the computational complexity of both on-grid and off-grid models with non-coherent measurements is compared in terms of running time, and the results are shown in Table 1, based on a computer with 4.2GHz CPU i7-7700K and 16GB RAM. We can see that although the computational time of off-grid method is higher than the on-grid method, the computational time cost by the second step of the off-grid model is minimal, especially compared with the refinement method.

Table 5.3 Running time of different non-coherent methods.

Snapshots	On-grid (s)	Off-grid (s)	Refinement (s)
100	226.11	226.22	395.84

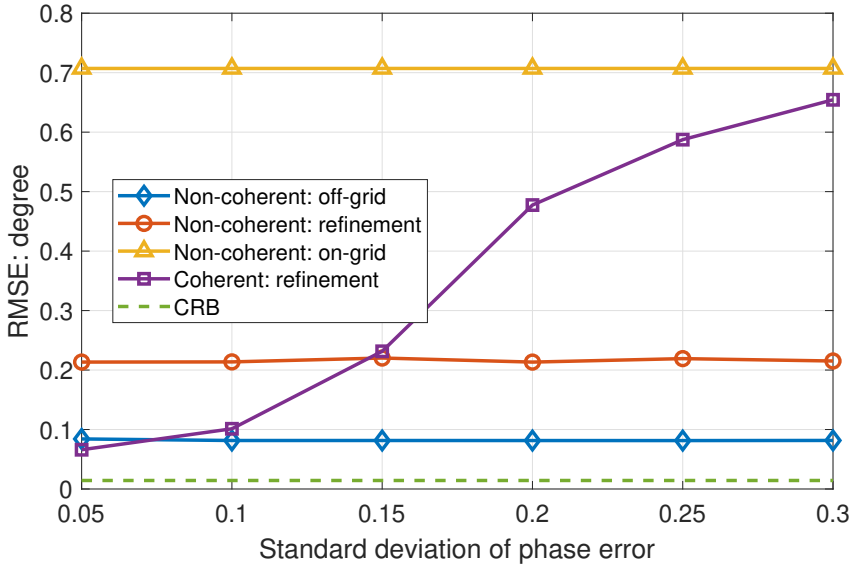

Fig. 5.8 RMSEs versus sensor phase error.

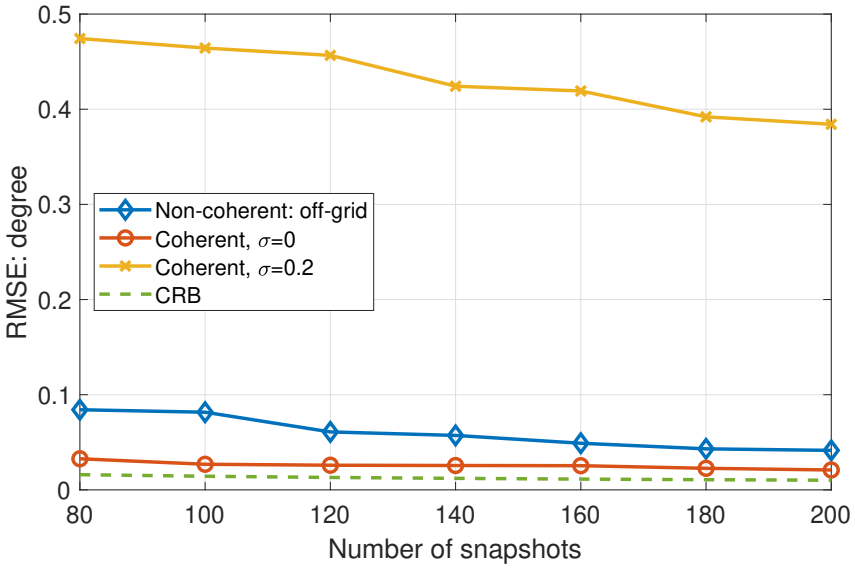

Fig. 5.9 RMSEs versus number of snapshots.

5.3 Summary

In this chapter, non-coherent DOA estimation and source localization of off-grid signals has been studied and an efficient two-step approach was proposed. In the first step, dictionary bias is assumed to be zero and the off-grid problem is considered as a normal group sparse phase retrieval problem, while in the second step, dictionary bias is estimated through an iterative process. Simulation results indicates that, for the same grid, the proposed off-grid non-coherent estimation method has given more accurate results than the on-grid model with very marginal extra time consumption. In addition, although the off-grid model with a larger stepsize requires less CPU time than the on-grid model with a smaller stepszie, the DOA estimation accuracy of the off-grid model is still better than the on-grid one. Unlike those existing AOA based methods, phase error at sensor arrays has no effect on the proposed non-coherent one, which means that phase calibration is no longer required. Simulation results shows that the proposed method outperforms the traditional method in terms of RMSE when the phase error occurs at the sensors, but at a cost of worse performance in the absence of phase errors.

Chapter 6

Non-Coherent DOA Estimation of Wideband Signals

For the narrowband case, some methods have been proposed based on the uniform linear array (ULA) [16–19, 89], dual array [49] or uniform circular arrays [88], where the key issue is to overcome the inherent ambiguities problem associated with magnitude-only measurements. Moreover, some general algorithms have also been proposed to exploit the multiple snapshots available in the array measurement, such as the modified GESPAR [16] and the ToyBar[49].

However, to our best knowledge, the wideband case has not been studied yet when only magnitude information of the received signals is available at the array. For wideband signals, those narrowband methods developed for DOA estimation cannot be applied directly, since the array output for wideband signals is obtained through a convolution process [20, 90]. For such a wideband DOA estimation problem, a common approach is applying discrete Fourier transform (DFT) to those measurements, and decomposing wideband signals into different frequency bins, where each bin provides a similar model as the narrowband one, when the number of DFT points is sufficiently large [91]. Under such a framework, many subspace based methods for wideband DOA estimation have been proposed, such as incoherent subspace method (ISM) [92, 93], coherent subspace method (CSM) [94], and test of orthogonality of projected subspaces (TOPS) [95]. Additionally, compressive sensing (CS) has been exploited for narrowband DOA estimation as the signal is sparse in the spatial

domain [14, 31, 35]. These CS based algorithms can be extended to wideband by applying it to each frequency bin separately. As the spatial support of incident signals over all frequency bins is identical, joint group sparsity has been introduced for the wideband signal model [43], which performs more effectively.

This DFT based approach only works for the traditional scenario when full measurements of the received array signals are available, and when only the magnitude information is available, we will not be able to apply the DFT operation to decompose the signals into different frequency bands, and therefore the DFT based approach will not work for the magnitude-only case. In this chapter, based on the idea of convolutional sparse coding (CSC) [96–98], a novel wideband signal model is first proposed for direct time-domain (TD) DOA estimation, and a group sparsity based minimization problem is formulated [99]. The traditional DFT based subspace methods, which require the number of DFT points to be large enough, will not work properly with a limited number of temporal snapshots; on the contrary, the propsoed TD-CSC wideband DOA estimation method still works effectively for a small number of snapshots. Based on the TD-CSC based wideband signal model, a non-coherent wideband DOA estimation method is further proposed in this chapter.

The remaining part is structured as follows. The wideband signal moldel with the CSC framework is described in Sec. 6.1. The proposed wideband DOA estimation method and its CRB are presented in Sec. 6.2 and simulation results are provided in Sec. 6.3. Conclusions are drawn in Sec. 6.4.

6.1 Wideband Signal Model in the Time Domain

With a sampling frequency f_s, the received wideband signal at the m-th sensor is given in (2.50). If $d = \lambda_{min}/2$, where λ_{min} is the wavelength corresponding to the maximum frequency of the signal and we sample the signal at the Nyquist rate, i.e. the sampling period $T_s = \frac{\lambda_{min}}{2c}$, the delay between the m-th sensor and the 0-th sensor is

$$\frac{\tau_{m,\theta_k}}{T_s} = m\sin\theta_k, \;\; a_{i,m,\theta_k} = \mathrm{sinc}(i - m\sin\theta_k), \tag{6.1}$$

For convenience of modelling in the following steps, the infinite impulse response in (2.50) is truncated to the range from $-I$ to I, where I is a large enough number. Then, (2.50) can be approximated with a small error, as

$$x_m[p] \approx \sum_{k=1}^{K} \Big(\sum_{i=-I}^{I} a_{i,m,\theta_k} s_k[p-i] \Big) + n_m[p]. \tag{6.2}$$

Considering P snapshots for the received signal $x_m[p],\ p \in \{0,...,P-1\}$, the required snapshots range of source signal $s_k[p]$ for $x_m[0]$ is $-I < p < I$, while for $x_m[P-1]$, the required snapshots range of source signal $s_k[p]$ is $P-1-I < p < P-1+I$. As a result, to calculate all values of $x_m[p]$ for all $0 \leq p \leq P-1$, the required range of $s_k[p]$ is $-I < p < P-1+I$, and the total number of required different snapshots for $s_k[p]$ is $P+2I$.

Therefore, constructing source signal vectors

$$\mathbf{s}_k = [s_k[-I],...,s_k[P-1+I]]^T, \tag{6.3}$$

and the measurements vector at the m-th sensor $\mathbf{x}_m$

$$\mathbf{x}_m = [x_m[0],...,x_m[P-1]]^T, \tag{6.4}$$

which can be written in a convolutional sparse coding (CSC) form [96–98], as

$$\mathbf{x}_m = \sum_{k=1}^{K} \mathbf{C}_{m,\theta_k} \mathbf{s}_k + \mathbf{n}_m, \tag{6.5}$$

where $\mathbf{C}_{m,\theta_k}$ is a $P \times (P+2I)$ banded and circulant matrix, given by

$$\mathbf{C}_{m,\theta_k} = \begin{bmatrix} a_{I,m,\theta_k} & \cdots & a_{-I,m,\theta_k} & \cdots & 0 \\ & \ddots & & \ddots & \vdots \\ 0 & \cdots & a_{I,m,\theta_k} & \cdots & a_{-I,m,\theta_k} \end{bmatrix} \tag{6.6}$$

and $\mathbf{n}_m = [n_m[0],...,n_m[P-1]]^T$ is the noise vector at the m-th sensor.

Furthermore, (6.5) can be reformulated in a more compact form as

$$\mathbf{x}_m = \mathbf{C}_m \mathbf{s} + \mathbf{n}_m, \tag{6.7}$$

where

$$\begin{aligned} \mathbf{s} &= [\mathbf{s}_1^T, ..., \mathbf{s}_K^T]^T, \\ \mathbf{C}_m &= [\mathbf{C}_{m,\theta_1}, ..., \mathbf{C}_{m,\theta_K}]. \end{aligned} \tag{6.8}$$

6.2 Time Domain Based Wideband DOA Estimation

6.2.1 Coherent DOA Estimation of Wideband Signals

Unlike those traditional CSC model, the signal vector $\mathbf{s}_k$ in DOA estimation is not sparse in the time-domain, and correspondingly, $\mathbf{s}$ is not sparse either. However, the signals are indeed sparse in the spatial domain, i.e., they only come from a rather limited number different directions [31]. Based on this spatial sparsity concept, to construct a spatially sparse source vector, we divide the whole admissible DOA range into G grid points with $G \gg K$, and for each direction $\theta_g,\ g \in \{1,2,...G\}$, we can construct the corresponding matrix $\mathbf{C}_{m,\theta_g}$, and form an overcomplete matrix

$$\tilde{\mathbf{C}}_m = [\mathbf{C}_{m,\theta_1}, ..., \mathbf{C}_{m,\theta_G}]. \tag{6.9}$$

Then, the signal vector $\mathbf{s}$ is extended to its corresponding $G(P+2I) \times 1$ sparse vector

$$\tilde{\mathbf{s}} = [\mathbf{s}_1^T, ..., \mathbf{s}_G^T]^T, \tag{6.10}$$

where only K groups out of its G groups corresponding to the true incident angles are supposed to be non-zero. Finally, the array output at the m-th sensor is given by

$$\mathbf{x}_m = \tilde{\mathbf{C}}_m \tilde{\mathbf{s}} + \mathbf{n}_m. \tag{6.11}$$

For M sensors in total, we have

$$\begin{aligned}\mathbf{x} &= [\mathbf{x}_0^T, ..., \mathbf{x}_{M-1}^T]^T = \tilde{\mathbf{C}}\tilde{\mathbf{s}} + \mathbf{n}, \\ \tilde{\mathbf{C}} &= [\tilde{\mathbf{C}}_0^T, ..., \tilde{\mathbf{C}}_{M-1}^T]^T, \\ \mathbf{n} &= [\mathbf{n}_0^T, ..., \mathbf{n}_{M-1}^T]^T.\end{aligned} \tag{6.12}$$

Now, since signal $\tilde{\mathbf{s}}$ is sparse, the wideband time-domain based DOA estimation problem can be formulated as a LASSO problem [100],

$$\min_{\tilde{\mathbf{s}}} \|\tilde{\mathbf{C}}\tilde{\mathbf{s}} - \mathbf{x}|_2^2 + \gamma\|\tilde{\mathbf{s}}\|_1, \tag{6.13}$$

where $\|\cdot\|_1$ represents l_1 norm of its variables to enforce its sparsity and γ is the penalty term.

In addition, the signals $\tilde{\mathbf{s}}$ has a group sparsity structure, where all the entries within a group are all zeros if there is no signal coming from that direction. Thus, the DOA estimation problem can be further formulated as a group LASSO problem [54], represented by the $l_{2,1}$ norm, given by

$$\min_{\tilde{\mathbf{s}}} \|\tilde{\mathbf{C}}\tilde{\mathbf{s}} - \mathbf{x}\|_2^2 + \gamma\|\tilde{\mathbf{s}}\|_{2,1}, \tag{6.14}$$

and the $l_{2,1}$ norm $\|\cdot\|_{2,1}$ is defined as

$$\|\tilde{\mathbf{s}}\|_{2,1} := \sum_{g=1}^{G} \|\mathbf{s}_g\|_2, \tag{6.15}$$

where $\mathbf{s}_g$ has been defined in (6.10).

Thus, the wideband DOA estimation problem can be formulated as

$$\min_{\tilde{\mathbf{s}}} \gamma \sum_{g=1}^{G} \|\mathbf{s}_g\|_2 + \|\tilde{\mathbf{C}}\tilde{\mathbf{s}} - \mathbf{x}\|_2^2, \tag{6.16}$$

This problem is convex and can be solved by convex optimization methods directly, such as the FISTA algorithm, which is an accelerated version of the proximal gradient method

[36, 55, 101, 102]. A summary of FISTA can be found in the following Algorithm Summary part.

Table 6.1 Algorithm Summary (FISTA)

Input: $\tilde{\mathbf{C}}$, $\mathbf{x}$, ρ, λ,
Output: $\tilde{\mathbf{s}}$ (reconstructed signal).
Initialization: Set $\tilde{\mathbf{s}}^0$ as a zero vector, $\tilde{\mathbf{b}}^0 = \tilde{\mathbf{s}}^0$.
$\beta^0 = 1$. Defining G groups of $\tilde{\mathbf{s}}$,
General steps: for q=0, ..., Q
1) Calculate gradient as
Gradient:$f(\tilde{\mathbf{b}}) = \nabla F(\tilde{\mathbf{b}}^q) = 2\tilde{\mathbf{C}}^H(\tilde{\mathbf{C}}\tilde{\mathbf{b}}^q - \mathbf{x})$,
2)For $i = 1, ..., G$,
Find $\tilde{\mathbf{s}}_i^{q+1}$ as
$\tilde{\mathbf{s}}_i^{q+1} = (\mathbf{b}_i^q - \lambda f(\mathbf{b}_i^q))\max(1 - \frac{\rho\lambda}{\|\mathbf{b}_i^q - \lambda\nabla f(\mathbf{b}_i^q)\|_2}, 0)$,
where $\mathbf{s}_i$ is subvector of $\tilde{\mathbf{s}}$ indexed by i.
3) **Update**: $\beta^{q+1} = \frac{1+\sqrt{1+4(\beta^q)^2}}{2}$.
$\mathbf{b}^{q+1} = \tilde{\mathbf{s}}^{q+1} + \frac{\beta^q - 1}{\beta^{q+1}}(\tilde{\mathbf{s}}^{q+1} - \tilde{\mathbf{s}}^q)$.

6.2.2 Cramér-Rao Bound

Based on the new model, the CRB for time-domain wideband DOA estimation is derived. From (6.12), the probability density function is expressed as

$$p(\mathbf{x};\mathbf{\Phi}) = \prod_{n=0}^{MP-1} \frac{1}{2\pi\sigma^2} e^{(x_n - \mathbf{C}_n\mathbf{s}_n)^2/2\sigma^2}, \tag{6.17}$$

where $\mathbf{C}_n$ and x_n represent the n-th row of $\mathbf{C}$ and $\mathbf{x}$, separately. The unknown parameter vector of arriving angles, magnitude, phase difference and noise level can be represented as

$$\mathbf{\Phi} = [\theta_1, ..., \theta_K, \boldsymbol{s}^T, \sigma^2]. \tag{6.18}$$

For deterministic but unknown $\mathbf{Cs}$, the Fisher information matrix (FIM) $\mathbf{F}$ is defined as

$$\mathbf{F}(\mathbf{\Phi}) = \mathbb{E}\{\frac{\partial \ln^2 p(\mathbf{x};\mathbf{\Phi})}{\partial\mathbf{\Phi}\partial\mathbf{\Phi}^T}\}. \tag{6.19}$$

The $\{i,j\}$-th entry of $\mathbf{F}$ is given by [70]

$$\begin{aligned}\mathbf{F}_{i,j} = &\Big[\frac{\partial \boldsymbol{\mu}(\boldsymbol{\Phi})}{\partial \Phi_i}\Big]^T \boldsymbol{\Gamma}^{-1}(\boldsymbol{\Phi})\Big[\frac{\partial \boldsymbol{\mu}(\boldsymbol{\Phi})}{\partial \Phi_j}\Big] \\ &+\frac{1}{2}\Big[\boldsymbol{\Gamma}^{-1}(\boldsymbol{\beta})\frac{\partial \boldsymbol{\Gamma}^{-1}(\boldsymbol{\Phi})}{\partial \Phi_i}\boldsymbol{\Gamma}^{-1}(\boldsymbol{\Phi})\frac{\partial \boldsymbol{\Gamma}^{-1}(\boldsymbol{\Phi})}{\partial \Phi_j}\Big],\end{aligned} \tag{6.20}$$

where $\boldsymbol{\Gamma}^{-1}(\boldsymbol{\Phi}) = \frac{1}{\sigma^2}\mathbf{I}_{MP}$, $\mathbf{I}_{MP}$ is the identity matrix, $(\cdot)^{-1}$ is the matrix inverse operator, and $\boldsymbol{\mu}(\boldsymbol{\Phi}) = \mathbf{C}\mathbf{s}$. Since $\boldsymbol{\mu}(\boldsymbol{\Phi})$ is independent of the noise level, we have

$$\mathbf{F} = \begin{bmatrix}\tilde{\mathbf{F}} & \mathbf{0} \\ \mathbf{0} & \mathbf{0}\end{bmatrix} + \begin{bmatrix}\mathbf{0} & \mathbf{0} \\ \mathbf{0} & \mathbf{F}_\sigma\end{bmatrix}, \tag{6.21}$$

where the DOA related block is in $\tilde{\mathbf{F}}$ and its $\{i,j\}$-th entry is expressed as

$$\tilde{\mathbf{F}}_{i,j} = \Big[\frac{\partial \boldsymbol{\mu}(\boldsymbol{\Phi})}{\partial \Phi_i}\Big]^T \boldsymbol{\Gamma}^{-1}(\boldsymbol{\Phi})\Big[\frac{\partial \boldsymbol{\mu}(\boldsymbol{\Phi})}{\partial \boldsymbol{\Phi_j}}\Big], \tag{6.22}$$

with $(\cdot)^{-1}$ being the matrix inverse operator. As the FIM is block diagonal, $\mathbf{F}_\sigma$ has no effect on the CRB result of DOAs. Thus, CRB of DOAs can be determined by the inverse of $\tilde{\mathbf{F}}$. Computing the derivatives of $\boldsymbol{\mu}(\boldsymbol{\Phi})$ with respect to $\boldsymbol{\Phi}$, we have

$$\begin{aligned}\mathbf{D} &= \frac{\partial \boldsymbol{\mu}(\boldsymbol{\Phi})}{\partial \boldsymbol{\Phi}} = [\mathbf{G}, \Delta, \mathbf{0}], \\ \mathbf{G} &= [\mathbf{c}_{\theta_1}\mathbf{s}_1, ..., \mathbf{c}_{\theta_k}\mathbf{s}_K],\ \mathbf{c}_{\theta_K} = \frac{\partial \mathbf{C}_{\theta_k}}{\partial \theta_k}, \\ \frac{\partial \mathrm{sinc}(i - m\sin\theta_k)}{\partial \theta_k} &= \frac{m\sin(\pi(i-m\sin\theta_k))\cos\theta_k}{\pi(i-m\sin\theta_k)^2} \\ &\quad - \frac{m\cos(\pi(i-m\sin\theta_k))\cos\theta_k}{i-m\sin\theta_k}, \\ \mathbf{C}_{\theta_k} &= [\mathbf{C}^T_{0,\theta_k}, ..., \mathbf{C}^T_{M-1,\theta_k}]^T, \\ \Delta &= \frac{\partial \boldsymbol{\mu}(\boldsymbol{\Phi})}{\partial \mathbf{s}} = \mathbf{C}.\end{aligned} \tag{6.23}$$

Then, $\tilde{\mathbf{F}}$ can be given by

$$\tilde{\mathbf{F}} = \frac{1}{\sigma^2}\mathbf{D}^H\mathbf{D}, \tag{6.24}$$

The CRB associated with the DOA of signals can be obtained by the diagonal elements of the inverse $\tilde{\mathbf{F}}$. However, in the proposed signal model, it is assumed that $I >> P$ and $K(P+2I) > MP$, which leads to a singular and uninvertible FIM [103]. Thus, CRB is approximated by the Moore–Penrose pseudoinverse of FIM instead of its inverse [104].

6.2.3 Non-Coherent DOA Estimation of Wideband Signal

The wideband signal model under CSC framework has been shown in Section 6.1. For non-coherent measurements, we have

$$\mathbf{y} = |\tilde{\mathbf{C}}\tilde{\mathbf{s}}| + \mathbf{n}, \tag{6.25}$$

where $\tilde{\mathbf{C}}$ and $\tilde{\mathbf{s}}$ have been defined in (6.12). Similar to (6.14), the non-coherent wideband DOA estimation problem can be formulated as an $l_{2,1}$ norm based phase retrieval problem, given by

$$\min_{\tilde{\mathbf{s}}} \||\tilde{\mathbf{C}}\tilde{\mathbf{s}}| - \mathbf{y}\|_2^2 + \gamma\|\tilde{\mathbf{s}}\|_{2,1}, \tag{6.26}$$

which can be solved by the proposed ToyBar, which is derived based on the PRIME [48] and proximal gradient methods [36], as introduced in Chapter 3.

6.3 Simulations

6.3.1 Coherent Wideband DOA Estimation

In this section, performance of the proposed time-domain CSC based method (TD-CSC) is studied and compared with the traditional frequency-domain method in [43] for wideband DOA estimation. A ULA of $M = 7$ sensors is used with $d = \lambda_{min}/2$ and sampling frequency $T_s = \lambda_{min}/(2c)$. The steering matrix is formed based on a step size of 0.5°, and the truncated convolution filter for generating wideband signals has a value of $I = 100$. The normalized

frequency of wideband signals ranges from 0.5π to π, and for the traditional method, P-point DFT is applied and the normalized frequency range of impinging signals covers the frequency bin range of $U = [P/4+1, P/2-1]$ (the same settings as in [43]). Note that with P time-domain snapshots and a P-point DFT, for the traditional method, there is only one data sample for each frequency bin. Both methods are run with FISTA [55]. The FISTA setting for both the proposed and the traditional methods are the same, with the number of iterations fixed at $R = 300$, and stepsize set as $1/(2\lambda_{max}(\tilde{\mathbf{C}}^H\tilde{\mathbf{C}}))$, where $\lambda_{max}(\cdot)$ is the maximum eigenvalue of its variable and $\tilde{\mathbf{C}}$ represents the overcomplete dictionary of sparse signals.

First, performances of the two methods are evaluated with different SNR values ranging from 0 dB to 20 dB in terms of the RMSE. $P = 32$ temporal measurements are collected, with two signals located at -10° and 10° with equal signal power, and the value I to construct time-domain steering matrix $\mathbf{C}$ in the algorithm is set as 50. The results are shown in Fig. 6.1, with each point obtained by averaging over 100 trials. It can be observed that, although both methods have achieved more accurate results with increasing SNR, the proposed method consistently outperforms the traditional one.

Next, the impact of the number of snapshots P is considered. The SNR is fixed at 20 dB while the number of snapshots ranges from 8 to 112. As shown in Fig. 6.2, the performance of the proposed time-domain method is acceptable even with only 8 snapshots, while the traditional frequency-domain method leads to a rather high RMSE initially. Moreover, increasing the number of snapshots can enhance the estimation performance of both methods, and with around 90 snapshots, the traditional method has outperformed the proposed one a little.

Now we examine the case with only 8 snapshots in a bit more detail. An example of estimated spatial spectrum in one run is given in Figs. (6.3) and (6.4), which show that although the proposed method maintains some error with only 8 snapshots, the traditional method has effectively failed. Note that the spacing between the two sources is 20 degrees, while the RMSE has been about 11 degrees for each source according to the figures.

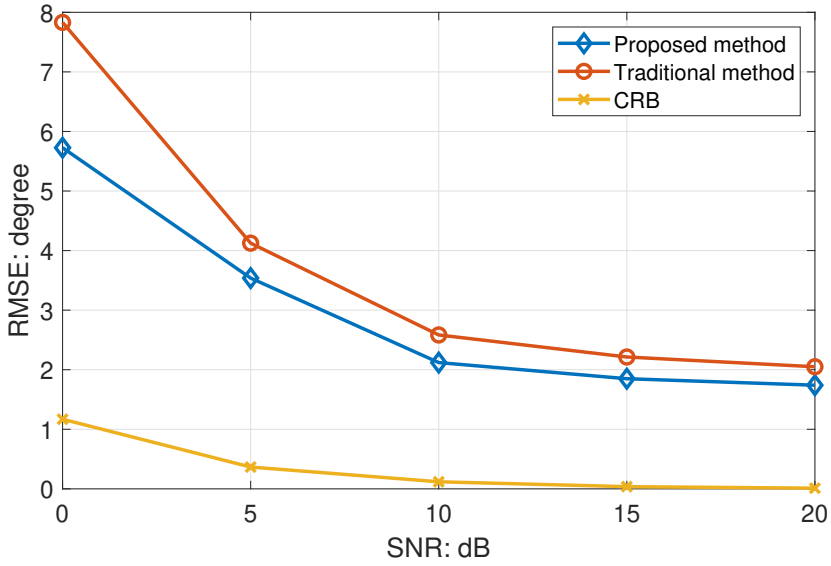

Fig. 6.1 RMSE vs. SNR.

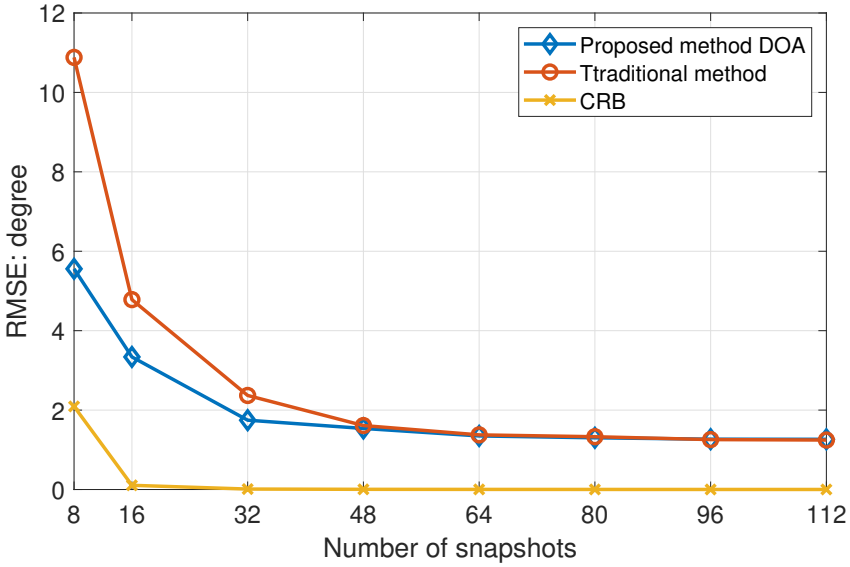

Fig. 6.2 RMSE vs. snapshots.

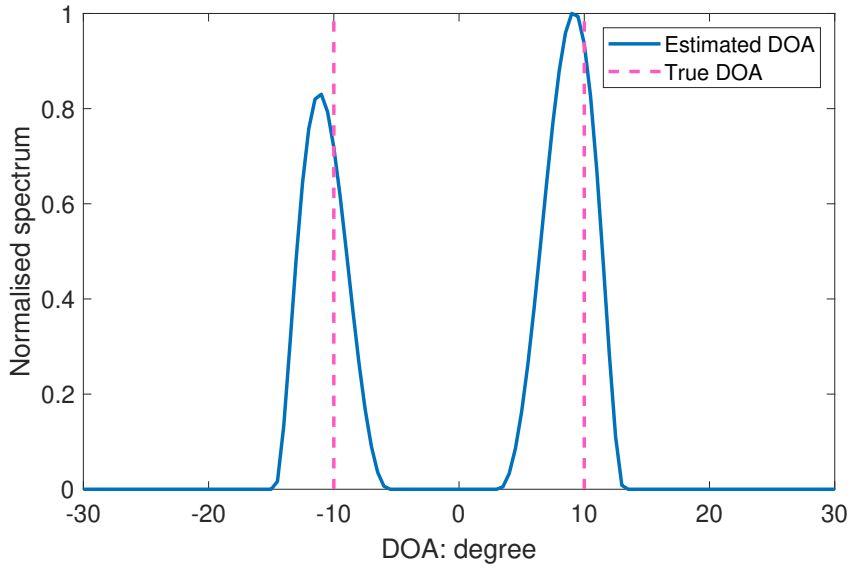

Fig. 6.3 The proposed method.

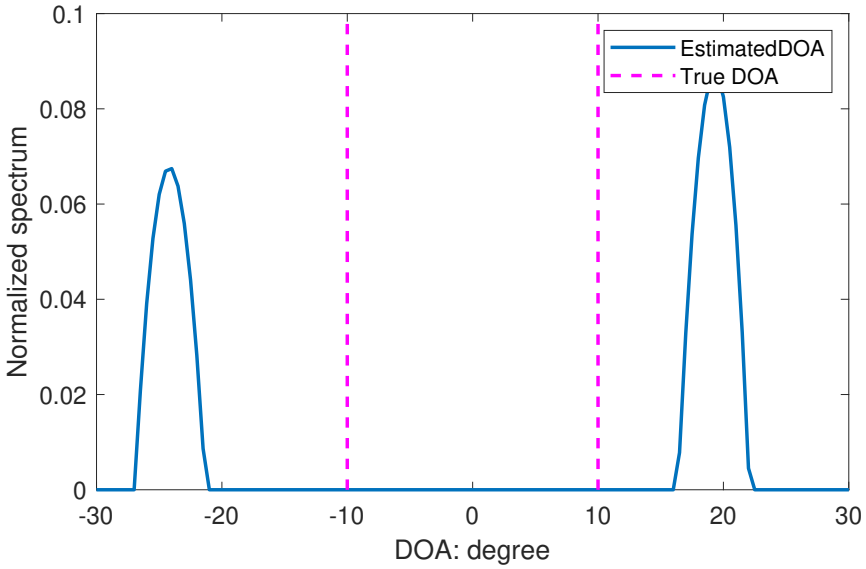

Fig. 6.4 The traditional method.

Table 6.2 Running time of the proposed method and the traditional method.

Computational time (sec)		
Snapshots	The proposed method	The traditional method
112	53.52	19.35
64	25.36	4.66
16	4.64	0.64
Number of parameters to be estimated		
The proposed method		The traditional method
G(2I+P)		GU

Since wideband DOA estimation in both proposed time-domain based and traditional frequency-domain based methods are formulated into a sparsity framework, the FISTA can be applied to both methods, which only requires simple matrix operations. Under the general sparse setting, their complexity depends on the number of parameters involved in the formulation. Thus, for M sensor measurements, the complexity for the proposed method is $O(MG(2I+P))$, while for the traditional method is $O(MGU)$. Since U depends on the number of available frequency bins, it contains at most P different bins. As a result, the proposed method is more complex than the traditional method. As listed in Table 1, the number of parameters to be estimated for the proposed method is much more than that for the traditional method since $U \approx P/4$ in this set of simulations. The running time of the proposed method is much longer. In addition, it is clear that the number of parameters to be estimated for the time-domain method is not only related to the number of snapshots, but also the value of I to construct the circulant matrix $\mathbf{C}$.

The performance of the proposed method with respect to the value of I for constructing $\mathbf{C}$ in the solution is presented in Fig. 6.5. All settings are the same as in the first simulation except for I and SNR is 20 dB. As shown, although the RMSE decreases with the value of I, the effect of I on RMSE can be ignored for a value larger than about 80.

Finally, we examine whether the proposed method can deal with the underdetermined case or not. In the first set of simulations, a ULA of $M = 4$ sensors is employed where the number of incident signals is $K = 4$ and $K = 5$, separately, and the results are shown in Figs. 6.6 and 6.7 with $P = 64$ snapshots. It can be seen that with a ULA, the proposed method

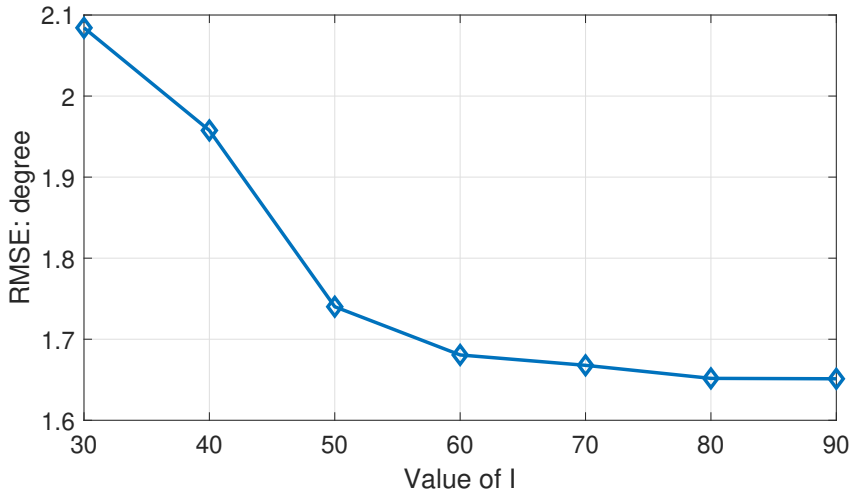

Fig. 6.5 RMSEs versus I.

cannot solve the underdetermined problem, which is consistent with our understanding about the degrees of freedom of a ULA. For underdetermined estimation, sparse array structures are normally employed by exploiting the co-array concept [31]. Thus, in the second set of simulations, we employ a minimum redundancy array (MRA) with $M = 4$ sensors and their positions are given by (0,1,4,6) [5]. The results are shown in Figs. 6.8 and 6.9 with $P = 64$ snapshots. It can be seen that although there are only 4 sensors, the proposed method can identify all the five sources successfully. This is an interesting result, as no co-array operation is employed in the process, which is different from the frequency-domain method in [31].

6.3.2 Non-Coherent Wideband DOA Estimation

In this section, performance of the proposed time-domain CSC based method with magnitude-only measurements is studied and compared with full measurements as proposed in [99] for wideband DOA estimation. A ULA of $M = 30$ sensors is used with $d = \lambda_{min}/2$ and sampling frequency $T_s = \lambda_{min}/(2c)$, while the number of snapshots is $P = 64$. A grid refinement approach is employed and the steering matrix is formed based on a step size of 3° for the initial step and 0.3° for the refinement step, and the value I to construct the time-domain steering matrix $\mathbf{C}$ in the algorithm is set as 50. The truncated convolution filter for generating wideband signals has a value of $I = 50$. For ToyBar settings for the proposed

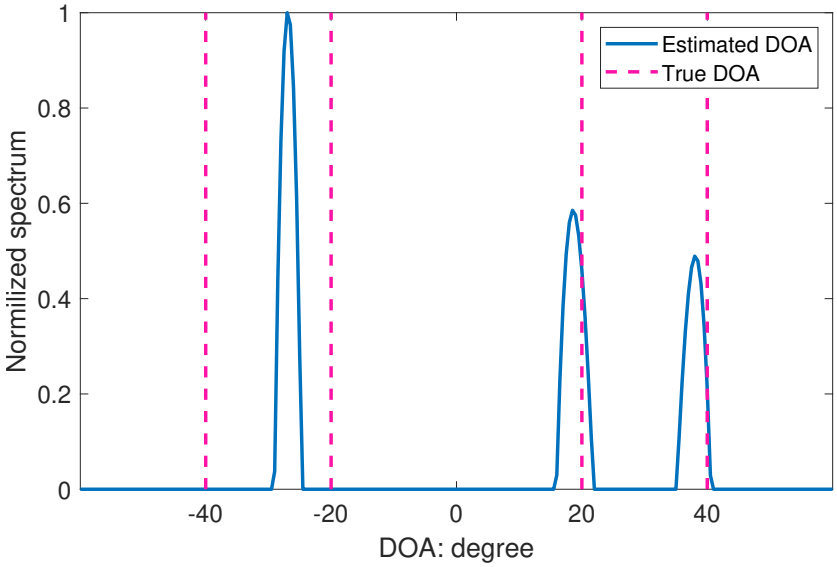

Fig. 6.6 Four incident signals with $M = 4$ sensors ULA.

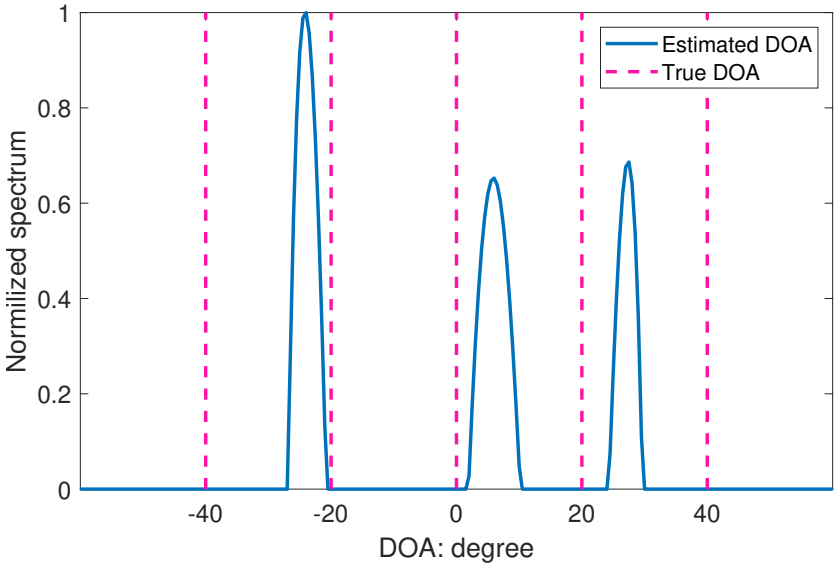

Fig. 6.7 Five incident signals with $M = 4$ sensors ULA.

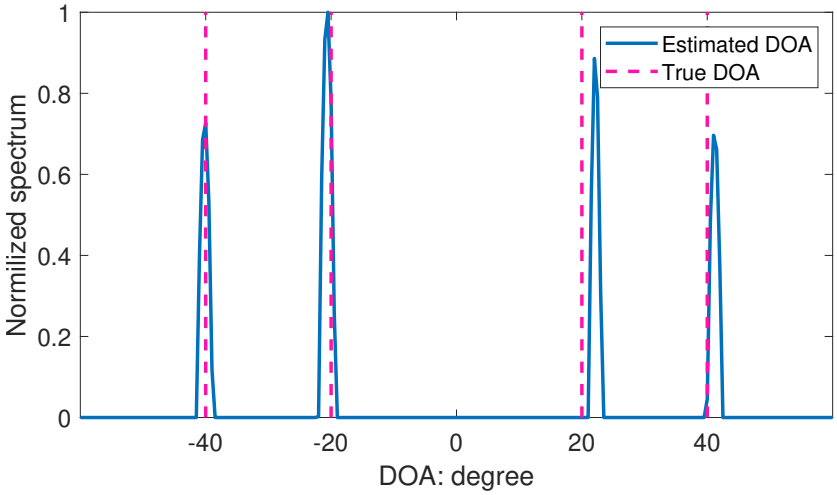

Fig. 6.8 Four incident signals with $M = 4$ sensors MRA.

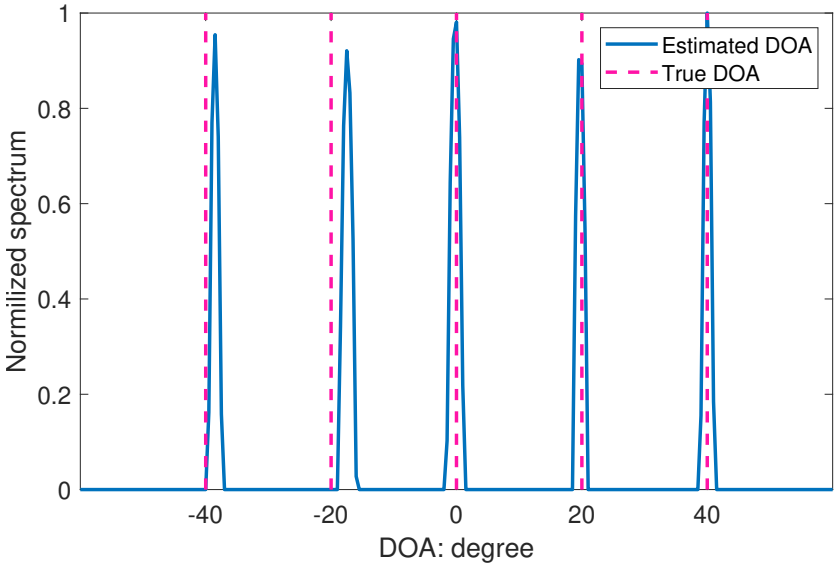

Fig. 6.9 Five incident signals with $M = 4$ sensors MRA.

method, the number of iterations is fixed at $R = 300$, and stepsize is set as $1/(2\lambda_{max}(\tilde{\mathbf{C}}^H\tilde{\mathbf{C}}))$, where $\lambda_{max}(\cdot)$ is the maximum eigenvalue of its variable and $\tilde{\mathbf{C}}$ represents the overcomplete dictionary of sparse signals.

For the first set of simulations, the SNR is 20 dB and there are $K = 2$ signals impinging on the array, with incident angles -30°, and 42°. The spectrum of estimation results is shown in Figs. 6.10 and 6.11, where the dotted lines represents the true incident angles. It can be seen that all 2 signals have been identified by both methods.

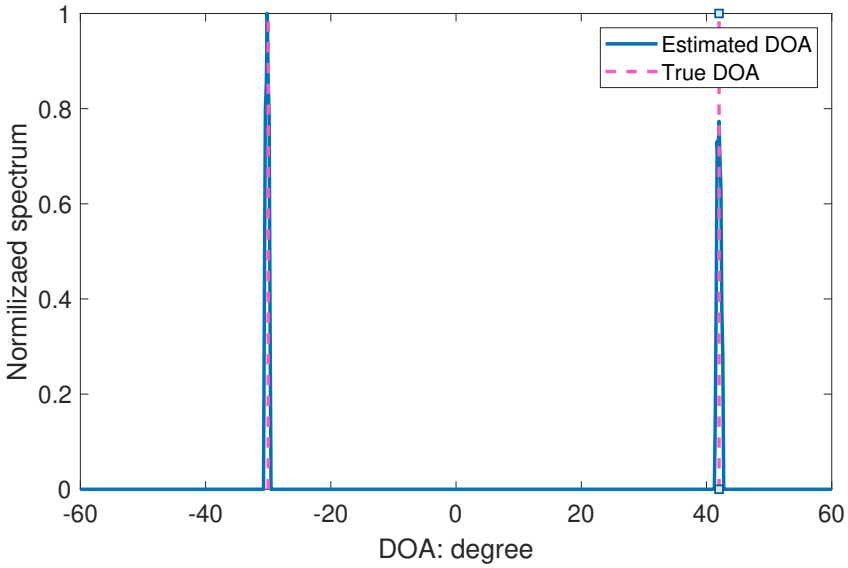

Fig. 6.10 Results with magnitude-only measurements.

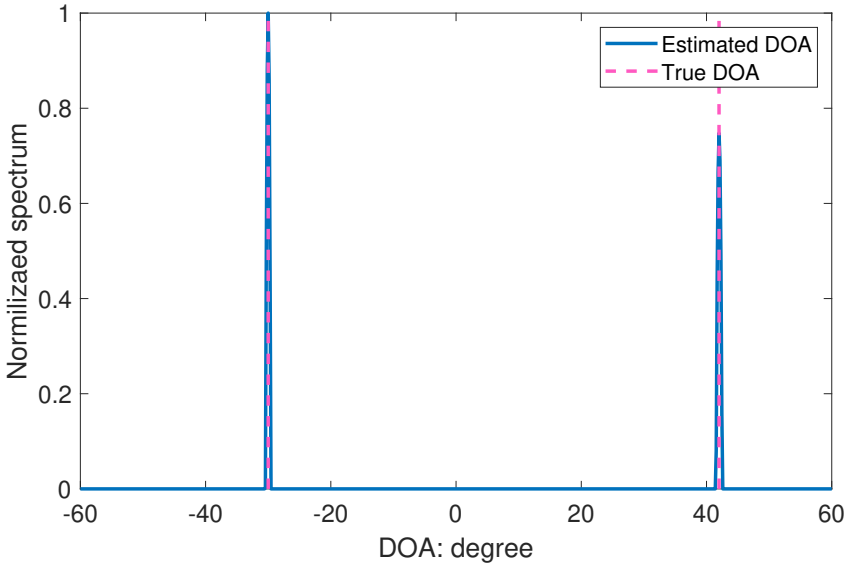

Fig. 6.11 Results with full measurements.

Next, performances of the two methods are evaluated with different SNR values ranging from 5 dB to 25 dB in terms of the RMSE. $P = 64$ temporal measurements are collected, with two signals located at -30° and 42°. The results are shown in Fig. 6.12, with each point obtained by averaging over 100 trials. It can be observed that, although both methods have achieved more accurate results with increasing SNR, the traditional coherent solution consistently outperforms the proposed one.

Finally, performances of the two methods with different snapshots are measured, while SNR is fixed at 25 dB and the results are shown in Fig. 6.13. According to the figure, it can be seen that although the performance of the non-coherent method increase significantly with the increasing number of snapshots, the gap between both method is still large, since the non-coherent method use only magnitude information.

6.4 Summary

A wideband DOA estimation method with both coherent and non-coherent measurements based on time-domain formulation has been proposed. The wideband DOA estimation problem was formulated in a CSC form, and $l_{2,1}$ norm is employed to enforce spatial sparsity. Unlike those existing frequency-domain based methods, no additional Fourier transform operation is needed by the proposed method, which means that even a small number of temporal snapshots are sufficient for DOA estimation.

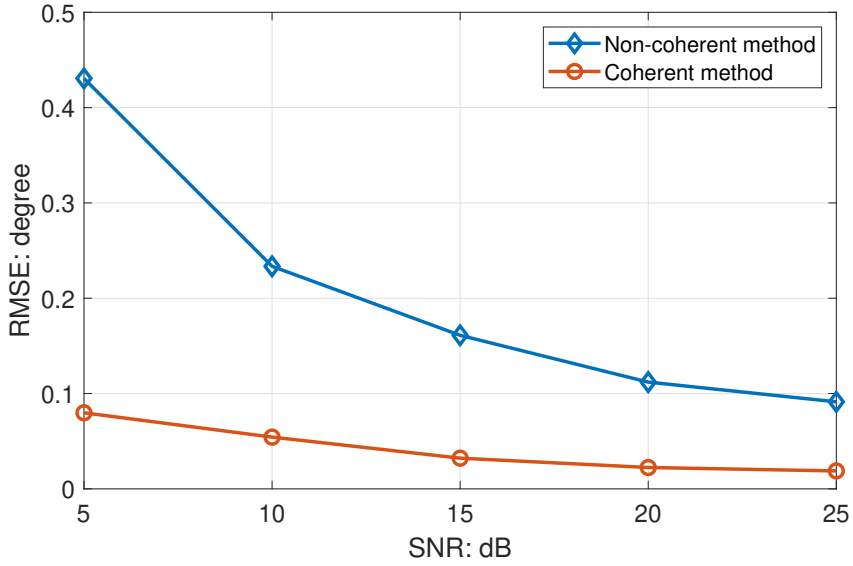

Fig. 6.12 RMSEs versus SNR.

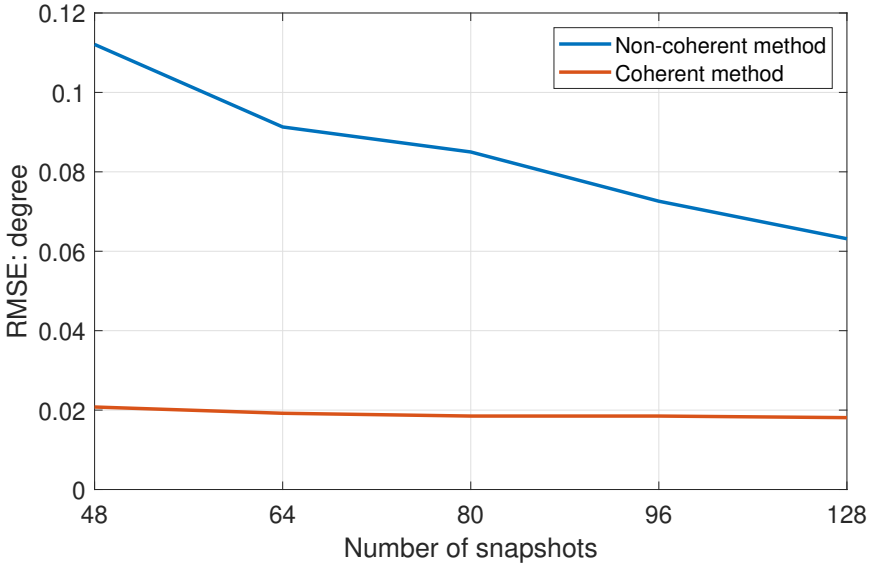

Fig. 6.13 RMSE vs number of snapshots.

Chapter 7

Conclusion and Future Plan

7.1 Conclusion

Non-coherent DOA estimation works effectively in the presence of phase errors while maintaining a good estimation accuracy. The problem was formulated as sparse phase retrieval problem, which traditionally only considers a single snapshot. For the non-coherent DOA estimation problem, multiple snapshots are normally available and the existing sparse phase retrieval algorithms fail to exploit multiple snapshots simultaneously. To solve this problem, a new algorithm named ToyBar was proposed, where the problem is transformed into its convex surrogate via the majorization-minimization technique, which can be solved by the well-known proximal gradient method. In addition to the well known mirroring and spatial shift ambiguity, a new ambiguity called spatial order ambiguity was also identified based on a detailed analysis. This ambiguity cannot be avoided by employing reference signals and one solution is to limit the inter-senor spacing d of ULAs to be less then $\lambda/4$ for a normal DOA range $[-90^\circ, 90^\circ]$.

Another issue of the non-coherent methods is the requirement of reference signals with precisely known DOAs to resolve inherent ambiguities. To deal with this challenge, two array structures were suggested. The first is a specific dual-array structure, which exploits spatial sparsity and formulates the non-coherent DOA estimation problem into an joint group sparsity based phase retrieval problem. The second array structure is the uniform circular

array, which can be applied to solve the ambiguity issue associated with the non-coherent problem directly as analysed. Simulations demonstrate that no reference signal is required while there are more than two impinging signals with these two array structures.

Since one disadvantage of the sparsity based method is the DOAs of signals are assumed to lie on the pre-defiend grids, which cannot be guaranteed in practice, the non-coherent DOA estimation of off-grid signals was then investigated and an efficient two-step off-grid method was presented. In the first step, dictionary bias is assumed to be zero and the off-grid problem is considered as a normal group sparse phase retrieval problem, while in the second step, dictionary bias is estimated through an iterative process. Through comparison, the proposed off-grid non-coherent DOA estimation method has provided more accurate results than the on-grid model with very marginal extra time consumption. This off-grid concept has also been extended to the non-coherent source localization problem, where the problem is formulated into a joint sparse phase retrieval form with distributed sensor arrays, and the $l_{2,1}$ norm is employed to enforce spatial sparsity.

Although the non-coherent DOA estimation problem has been studied by some researchers in recent years, the wideband non-coherent DOA estimation problem has not been addressed yet. Traditionally, DFT is applied to sensor measurements to transform the received wideband signals into narrowband signals with different frequencies. However, for non-coherent measurements, DFT cannot be applied to make such a transformation. In order to solve the wideband non-coherent DOA estimation problem, a time-domain wideband DOA estimation method based on CSC was proposed first, where no DFT operation is required. Then, the signal model was extended to the non-coherent scenario. As demonstrated by computer simulations, that the proposed time-domain method has outperformed the frequency-domain based one when the number of snapshots is limited, and the CSC based wideband method can be extended to non-coherent measurements effectively.

7.2 Future Work

In our research, non-coherent DOA estimation is formulated as a multi-snapshot sparse phase retrieval problem. Alhough the proposed ToyBar is more efficient than existing methods, its computational complexity is still high. It the future, low complexity version of the proposed ToyBar might be developed. In addition to improving the existing method, other low complexity methods might also be studied (i.e. atomic norm). Besides, compared to traditional coherent DOA estimation methods, the number of sensors required in non-coherent scenario is higher. Sparse arrays may be considered to increases the number of degrees of freedom.

For non-coherent wideband DOA estimation, the ambiguities issue should be further analysed mathematically although simulation results have indicated that no ambiguities appear in the wideband scenario. In addition, the off-grid approach for narrowband methods cannot be extended to the wideband case directly, and further research on off-grid wideband model is needed to achieve a better performance.

However, while testing the performance of proposed DOA estimation methods via simulations, the radiation pattern of sensors are assumed to be ideal, which is impractical in practice due to mutual coupling, circuit errors or other issues. Therefore, in order to examine its performance in real world scenarios, EM CST simulations can be involved to calculate more practical array responses in the future, or robust methods need to be developed to tackle possible model errors. In addition, since the thesis assumes there is no multi-path effect, the non-coherent DOA estimation with multi-path effect can be another topic of future research.

References

[1] H. L. V. Trees, *Detection, Estimation, and Modulation Theory: Part I*. NJ, USA: John Wiley & Sons, 2001.

[2] B. Van Veen and K. Buckley, "Beamforming: a versatile approach to spatial filtering," *IEEE ASSP Magazine*, vol. 5, no. 2, pp. 4–24, April 1988.

[3] L. C. Godara, "Application of antenna arrays to mobile communications part II. beamforming and direction-of-arrival considerations," *Proceedings of the IEEE*, vol. 85, no. 8, pp. 1195–1245, 1997.

[4] H. Krim and M. Viberg, "Two decades of array signal processing research: the parametric approach," *IEEE ASSP Magazine*, vol. 13, no. 4, pp. 67–94, 1996.

[5] H. L. V. Trees, *Optimum Array Processing: Part IV of Detection, Estimation, and Modulation Theory*. NJ, USA: John Wiley & Sons, 2002.

[6] K. T. Wong and M. D. Zoltowski, "Closed-form underwater acoustic direction-finding with arbitrarily spaced vector hydrophones at unknown locations," *IEEE Journal of Oceanic Engineering*, vol. 22, no. 3, pp. 566–575, July 1997.

[7] B. V., A. Finez, B. S., F. F., M. J. I., and B. Nicolas, "Hydrophone array optimization, conception, and validation for localization of acoustic sources in deep-sea mining," *IEEE Journal of Oceanic Engineering*, vol. 42, no. 2, pp. 555–563, April 2021.

[8] F. Vignon and M. R. Burcher, "Capon beamforming in medical ultrasound imaging with focused beams," *IEEE Transactions on Ultrasonics, Ferroelectrics, and Frequency Control*, vol. 55, no. 3, pp. 619–628, March 2008.

[9] C. Nilsen and I. Hafizovic, "Beamspace adaptive beamforming for ultrasound imaging," *IEEE Transactions on Ultrasonics, Ferroelectrics, and Frequency Control*, vol. 56, no. 10, pp. 2187–2197, October 2009.

[10] A. J. Duncan and A. N. Gavrilov, "The CMST airgun array model— a simpleapproach to modeling the underwater sound output from seismic airgun arrays," *IEEE Journal of Oceanic Engineering*, vol. 44, no. 3, pp. 589–597, July 2019.

[11] J. Capon, "High-resolution frequency-wavenumber spectrum analysis," *Proceedings of the IEEE*, vol. 57, no. 8, pp. 1408–1418, August 1969.

[12] R. Schmidt, "Multiple emitter location and signal parameter estimation," *IEEE Transactions on Antennas and Propagation*, vol. 34, no. 3, pp. 276–280, March 1986.

[13] R. Roy and T. Kailath, "ESPRIT, estimation of signal parameters via rotation invariance techniques," *IEEE Transactions on Acoustics, Speech, and Signal Processing*, vol. 37, no. 7, pp. 984–995, July 1989.

[14] D. Malioutov, M. Cetin, and S. Willsky, "A sparse signal reconstruction perspective for source localization with sensor arrays," *IEEE Transactions on Signal Processing*, vol. 53, no. 8, pp. 3010–3022, August 2005.

[15] P. Stoica, P.and Babu and J. Li, "Spice: A sparse covariance-based estimation method for array processing," *IEEE Transactions on Signal Processing*, vol. 59, no. 2, pp. 629–638, November 2011.

[16] H. Kim, A. M. Haimovich, and Y. C. Eldar, "Non-coherent direction of arrival estimation from magnitude only measurements," *IEEE Signal Processing Letters*, vol. 22, no. 7, pp. 925–929, July 2015.

[17] C. R. Karanam, B. Korany, and Y. Mostofi, "Magnitude-based angle-of-arrival estimation, localization, and target tracking," in *Proc. ACM/IEEE Information Processing in Sensor Networks*, Porto, Portugal, April 2018, pp. 254–265.

[18] H. Zayyani and M. Korki, "Non-coherent direction of arrival estimation via frequency estimation," 2016, doi:arXiv:1606.06423.

[19] Y. Tian, J. Shi, Y. Wang, and Q. Lian, "Non-coherent direction of arrival estimation utilizing linear model approximation," *Signal Processing*, vol. 157, pp. 261–265, December 2019.

[20] W. Liu, *Wideband Beamforming: Concepts and Techniques*. NJ, USA: John Wiley & Sons, 2010.

[21] D. Johnson, "The application of spectral estimation methods to bearing estimation problems," *Proceedings of the IEEE*, vol. 70, no. 9, pp. 1018–1028, September 1982.

[22] M. S. Bartlett, *An Introduction to Stochastic Processing*. Cambridge: Cambridge University, 1956.

[23] A. Barabell, "Improving the resolution performance of eigenstructure-based direction-finding algorithms," in *Proc. IEEE International Conference on Acoustics, Speech and Signal Processing.*, vol. 8, April 1983, pp. 336–339.

[24] R. DeGroat, E. Dowling, and D. Linebarger, "The constrained music problem," *IEEE Transactions on Signal Processing*, vol. 41, no. 3, pp. 1445–1449, March 1993.

[25] K. V. Rangarao and S. Venkatanarasimhan, "Gold-music: a variation on MUSIC to accurately determine peaks of the spectrum," *IEEE Transactions on Antennas and Propagation*, vol. 61, no. 4, pp. 2263–2268, April 2013.

[26] D. Donoho, "Compressed sensing," *IEEE Transactions on Information Theory*, vol. 52, no. 4, pp. 1289–1306, April 2006.

[27] Z. Liu, Z. Huang, and Y. Zhou, "Direction-of-arrival estimation of wideband signals via covariance matrix sparse representation," *IEEE Transactions on Signal Processing*, vol. 59, no. 9, pp. 4256–4270, September 2011.

[28] ——, "Sparsity inducing direction finding for narrowband and wideband signals based on array covariance vectors," *IEEE Transactions on Wireless Communications*, vol. 12, no. 8, pp. 1–12, August 2013.

[29] Y. D. Zhang, M. Amin, and B. Himed, "Sparsity-based DOA estimation using co-prime arrays," in *Proc. IEEE International Conference on Acoustics, Speech and Signal Processing.*, Vancouver, BC, Canada, May 2013, pp. 3967–3971.

[30] G. Jiang, M. Wang, X. Mao, C. Qian, Y. Liu, and A. Nehorai, "Underdetermined direction-of-arrival estimation using difference coarray in the presence of unknown nonuniform noise," *IEEE Access*, vol. 7, pp. 157 643–157 654, October 2019.

[31] Q. Shen, W. Liu, W. Cui, and S. Wu, "Underdetermined DOA estimation under the compressive sensing framework: a review," *IEEE Access*, vol. 4, pp. 8865–8878, November 2016.

[32] S. Mallat and Z. Zhang, "Matching pursuits with time frequency dictionaries," *IEEE Transactions on Signal Processing*, vol. 41, no. 12, pp. 3397–3415, December 1993.

[33] Y. Pati, R. Rezaiifar, and P. Krishnaprasad, "Orthogonal matching pursuit: recursive function approximation with applications to wavelet decomposition," in *Proc. Asilomar Conference on Signals, Systems and Computers*, Pacific Grove, CA, USA, August 1993, pp. 40–44.

[34] Y. Hu, C. Li, K. Meng, J. Qing, and X. Yang, "Group sparse optimization via $l_{p,q}$ regularization," *Journal of Machine Learning Research*, vol. 18, no. 30, pp. 1–52, 2016.

[35] J. Yin and T. Chen, "Direction-of-arrival estimation using a sparse representation of array covariance vectors," *IEEE Transactions on Signal Processing*, vol. 59, no. 9, pp. 4489–4493, June 2011.

[36] N. Parikh and S. Boyd, "Proximal algorithms," *Foundations and Trends in Optimization*, vol. 1, no. 3, p. 123–231, 2014.

[37] M. Grant and S. Boyd, "CVX: Matlab software for disciplined convex programming, version 2.1," http://cvxr.com/cvx, March 2014.

[38] L. C. Godara, "The effect of phase-shifter errors on the performance of an antenna-array beamformer," *IEEE Journal of Oceanic Engineering*, vol. 10, no. 3, pp. 278–284, July 1985.

[39] A. Swindlehurst and T. Kailath, "A performance analysis of subspace-based methods in the presence of model errors. i. the music algorithm," *IEEE Transactions on Signal Processing*, vol. 40, no. 7, pp. 1758–1774, July 1992.

[40] Y. Shechtman, A. Beck, and Y. C. Eldar, "Gespar: Efficient phase retrieval of sparse signals," *IEEE Transactions on Signal Processing*, vol. 62, no. 4, pp. 928–938, January 2014.

[41] C. H. Papadimitriou and K. Steiglitz, *Combinatorial Optimization: ALgorithms and Complexity*. New York: Dover Publications, INC, 1998.

[42] B. D. P., *Nonlinear Programming*. Nashua, NH, USA: Athena Scientific, 1999.

[43] Q. Shen, W. Liu, W. Cui, S. Wu, Y. D. Zhang, and M. G. Amin, "Low-complexity direction-of-arrival estimation based on wideband co-prime arrays," *IEEE Transactions on Speech and Audio Processing*, vol. 23, no. 9, pp. 1445–1456, May 2015.

[44] Y. Shechtman, Y. C. Eldar, O. Cohen, H. N. Chapman, J. Miao, and M. Segev, "Phase retrieval with application to optical imaging: a contemporary overview," *IEEE Signal Processing Magazine*, vol. 32, no. 3, pp. 87–109, April 2015.

[45] A. Walther, "The question of phase retrieval in optics," *Optica Acta: International Journal of Optics*, vol. 10, no. 1, pp. 41–49, 1963.

[46] R. W. Harrison, "Phase problem in crystallography," *Journal of the Optical Society of America*, vol. 10, no. 5, pp. 1046–1055, May 1993.

[47] F. J. R., "Phase retrieval algorithms: a comparison," *Applied Optics*, vol. 21, no. 15, pp. 2758–2769, August 1982.

[48] T. Qiu, P. Babu, and D. P. Palomar, "Prime: Phase retrieval via majorization-minimization," *IEEE Transactions on Signal Processing*, vol. 64, no. 19, pp. 5174–5186, June 2016.

[49] Z. Wan and W. Liu, "Non-coherent DOA estimation via proximal gradient based on a dual-array structure," *IEEE Access*, vol. 9, pp. 26 792–26 801, February 2012.

[50] S. Chen, D. L. Donoho, and M. A. Saunders, "Atomic decomposition by basis pursuit," *SIAM Journal on Scientific Computing*, vol. 20, no. 1, pp. 33–61, 1998.

[51] E. J. Candès, X. Li, and M. Soltanolkotabi, "Phase retrieval via Wirtinger flow: theory and algorithms," *IEEE Transactions on Information Theory*, vol. 61, no. 4, pp. 1985–2007, February 2015.

[52] Y. Sun, P. Babu, and D. P. Palomar, "Majorization-minimization algorithms in signal processing, communications, and machine learning," *IEEE Transactions on Signal Processing*, vol. 65, no. 3, pp. 794–816, August 2017.

[53] Q. Li, W. Liu, L. Huang, W. Sun, and P. Zhang, "An undersampled phase retrieval algorithm via gradient iteration," in *Proc. Sensor Array and Multichannel Signal Processing Workshop*, Sheffield, UK, July 2018, pp. 228–231.

[54] S. V. Effendi and X. Vilhjálmsson, "Group sparse optimization by alternating direction method," Rice University, Houston, TX, USA, Tech. Rep. Technical Report TR11-06, 2011.

[55] A. Beck and M. Teboulle, "A fast iterative shrinkage-thresholding algorithm for linear inverse problems," *SIAM Journal on Imaging Sciences*, vol. 2, no. 1, pp. 183–202, March 2009.

[56] M. V. W. Zibetti, E. Helou, R. Regatte, and G. Herman, "Monotone FISTA with variable acceleration for compressed sensing magnetic resonance imaging," *IEEE Transactions on Computational Imaging*, vol. 5, no. 1, pp. 109–119, November 2019.

[57] Y. E. Nesterov, "A method for solving the convex programming problem with convergence rate $o(1/k^2)$," *Soviet Mathematics Doklady*, vol. 27, no. 2, pp. 372–376, 1983.

[58] R. Balan, P. Casazza, and D. Edidin, "On signal reconstruction without phase," *Applied and Computational Harmonic Analysis*, vol. 20, no. 3, pp. 345–356, May 2006.

[59] A. S. Bandeira, J. Cahill, D. G. Mixon, and A. A. Nelson, "Saving phase: Injectivity and stability for phase retrieval," *Applied and Computational Harmonic Analysis*, vol. 37, no. 1, pp. 106–125, July 2014.

[60] A. Conca, D. Edidin, M. Hering, and C. Vinzant, "An algebraic characterization of injectivity in phase retrieval," *IEEE Transactions on Signal Processing*, vol. 38, no. 2, pp. 346–356, March 2015.

[61] X. Li and V. Voroninski, "Sparse signal recovery from quadratic measurements via convex programming," *SIAM Journal on Mathematical Analysis*, vol. 45, no. 5, pp. 3019–3033, September 2013.

[62] H. Ohlsson and Y. C. Eldar, "On conditions for uniqueness in sparse phase retrieval," in *Proc. IEEE International Conference on Acoustics, Speech and Signal Processing.*, Florence, Italy, May 2014, pp. 1841–1845.

[63] W. Jiang and A. M. Haimovich, "Cramer-Rao bound and approximate maximum likelihood estimation for non-coherent direction of arrival problem," in *Proc. Annual Conference on Information Science and Systems*, Princeton, NJ, USA, March 2016, pp. 506–510.

[64] ——, "Cramer–Rao bound for noncoherent direction of arrival estimation in the presence of sensor location errors," *IEEE Signal Processing Letters*, vol. 24, no. 9, pp. 1303–1307, June 2017.

[65] W. Wang, R. Wu, J. Liang, and H. C. So, "Phase retrieval approach for DOA estimation with array errors," *IEEE Transactions on Aerospace and Electronic Systems*, vol. 53, no. 5, pp. 2610–2620, May 2017.

[66] A. Liu, G. Liao, C. Zeng, Z. Yang, and Q. Xu, "An eigenstructure method for estimating doa and sensor gain-phase errors," *IEEE Transactions on Signal Processing*, vol. 59, no. 12, pp. 5944–5956, August 2011.

[67] Q. Chen, N. D. Sidiropoulos, K. Huang, L. Huang, and S. H. C., "Phase retrieval using feasible point pursuit: algorithms and Cramer–Rao bound," *Applied and Computational Harmonic Analysis*, vol. 64, no. 20, pp. 5282–5296, October 2016.

[68] R. Balan, "Reconstruction of signals from magnitudes of redundant representations: the complex case." *Foundations of Computational Mathematics*, vol. 16, pp. 677–721, May 2016.

[69] S. Basu and Y. Bresler, "The stability of nonlinear least squares problems and the cramer-Rao bound," *IEEE Transactions on Signal Processing*, vol. 48, no. 12, pp. 3426–3436, December 2000.

[70] K. S. M., *Fundamentals of Statistical Signal Processing: Estimation Theory*. NJ: Upper Saddle River, 1993.

[71] W. Liu, "Blind adaptive wideband beamforming for circular arrays based on phase mode transformation," *Digital Signal Processing*, vol. 21, no. 2, pp. 239–247, March 2011.

[72] H. Zhu, G. Leus, and G. B. Giannakis, "Sparsity-cognizant total least-squares for perturbed compressive sampling," *IEEE Transactions on Signal Processing*, vol. 59, no. 5, pp. 2002–2016, February 2011.

[73] Z. Yang, L. Xie, and C. Zhang, "Off-grid direction of arrival estimation using sparse Bayesian inference," *IEEE Transactions on Signal Processing*, vol. 61, no. 1, pp. 38–43, October 2013.

[74] Z. Tan, P. Yang, and A. Nehorai, "Joint sparse recovery method for compressed sensing with structured dictionary mismatches," *IEEE Transactions on Signal Processing*, vol. 62, no. 19, pp. 4997–5008, July 2014.

[75] Q. Shen, W. Cui, W. Liu, S. Wu, Y. D. Zhang, and M. G. Amin, "Underdetermined wideband doa estimation of off-grid sources employing the difference co-array concept," *Signal Processing*, vol. 130, pp. 299–304, July 2016.

[76] W. Cui, Q. Shen, W. Liu, and S. Wu, "Low complexity DOA estimation for wideband off-grid sources based on re-focused compressive sensing with dynamic dictionary," *IEEE Journal of Selected Topics in Signal Processing*, vol. 13, no. 5, pp. 918–930, August 2019.

[77] X. Wu, W. Zhu, J. Yan, and Z. Zhang, "Two sparse-based methods for off-grid direction-of-arrival estimation," *Signal Processing*, vol. 142, pp. 87–95, January 2018.

[78] C. Liu, D. Fang, Z. Yang, H. Jiang, X. Chen, W. Wang, T. Xing, and L. Cai, "RSS distribution-based passive localization and its application in sensor networks," *IEEE Transactions on Wireless Communications*, vol. 15, no. 4, pp. 2883–2895, April 2016.

[79] D. Dardari, C. Chong, and M. Win, "Threshold-based time-of-arrival estimators in UWB dense multipath channels," *IEEE Transactions on Communications*, vol. 56, no. 8, pp. 1366–1378, August 2008.

[80] R. Amiri, F. Behnia, and A. Noroozi, "An efficient estimator for TDOA-based source localization with minimum number of sensors," *IEEE Communications Letters*, vol. 22, no. 12, pp. 2499–2502, December 2018.

[81] Y. Zou, Q. Wan, and H. Liu, "Semidefinite programming for TDOA localization with locally synchronized anchor nodes," in *Proc. IEEE International Conference on Acoustics, Speech and Signal Processing.*, Calgary, Canada, April 2016, pp. 3524–3528.

[82] A. J. Weiss, "Direct position determination of narrowband radio frequency transmitters," *IEEE Signal Processing Letters*, vol. 11, no. 5, pp. 513–516, May 2004.

[83] N. Garcia, H. Wymeersch, E. G. Larsson, A. M. Haimovich, and M. Coulon, "Direct localization for massive MIMO," *IEEE Transactions on Signal Processing*, vol. 65, no. 10, pp. 2475–2487, May 2017.

[84] K. Dogancay, "Bearings-only target localization using total least squares," *Signal Processing*, vol. 85, no. 9, pp. 1695–1710, April 2005.

[85] Z. Wang, J. Luo, and X. Zhang, "A novel location-penalized maximum likelihood estimator for bearing-only target localization," *IEEE Transactions on Signal Processing*, vol. 60, no. 12, pp. 6166–6181, December 2012.

[86] Q. Shen, W. Liu, L. Wang, and Y. Liu, "Group sparsity based localization for far-field and near-field sources based on distributed sensor array networks," *IEEE Transactions on Signal Processing*, vol. 68, pp. 6493–6508, November 2020.

[87] H. Wu, Q. Shen, W. Liu, and Y. Liang, "Underdetermined two-dimensional localization for wideband sources based on distributed sensor array networks," in *Proc. IEEE International Conference on Acoustics, Speech and Signal Processing.*, 2022, pp. 5133–5137.

[88] Z. Wan and W. Liu, "Non-coherent DOA estimation of off-grid signals with uniform circular arrays," in *Proc. IEEE International Conference on Acoustics, Speech and Signal Processing.*, Toronto, Canada, April 2021, pp. 4370–4374.

[89] M. Delbari, A. Javaheri, H. Zayyani, and F. Marvasti, "Non-coherent DOA estimation via majorization-minimization using sign information," *IEEE Signal Processing Letters*, vol. 29, pp. 892–896, Mar. 2022.

[90] W. Liu, "Wideband beamforming for multipath signals based on frequency invariant transformation," *International Journal of Automation and Computing*, vol. 9, no. 4, pp. 420–428, 2012.

[91] Y. Liang, W. Cui, Q. Shen, W. Liu, and S. Wu, "Cramér-Rao bound analysis of underdetermined wideband DOA estimation under the subband model via frequency decomposition," *IEEE Transactions on Signal Processing*, vol. 69, pp. 4132–4148, June 2021.

[92] G. Su and M. Morf, "The signal subspace approach for multiple wide-band emitter location," *IEEE Transactions on Acoustics, Speech, and Signal Processing*, vol. 31, no. 6, pp. 1502–1522, December 1983.

[93] M. Wax, S. T. J., and T. Kailath, "Spatio-temporal spectral analysis by eigenstructure methods," *IEEE Transactions on Acoustics, Speech, and Signal Processing*, vol. 32, no. 4, pp. 817–827, August 1984.

[94] H. Wang and M. Kaveh, "Coherent signal-subspace processing for the detection and estimation of angles of arrival of multiple wide-band sources," *IEEE Transactions on Acoustics, Speech, and Signal Processing*, vol. 33, no. 4, pp. 823–831, August 1985.

[95] Y. S. Yoon, L. Kaplan, and J. McClellan, "Tops: new doa estimator for wideband signals," *IEEE Transactions on Signal Processing*, vol. 54, no. 6, pp. 1977–1989, 2006.

[96] V. Papyan, J. Sulam, and M. Elad, "Working locally thinking globally: theoretical guarantees for convolutional sparse coding," *IEEE Transactions on Signal Processing*, vol. 65, no. 21, pp. 5687–5701, July 2017.

[97] R. Grosse, R. Raina, H. Kwong, and A. Y. Ng, "Shift-invariant sparse coding for audio classification," in *Uncertainty in Artificial Intelligence*, July 2007, pp. 149–158.

[98] M. D. Zeiler, D. Krishnan, G. W. Taylor, and R. Fergus, "Deconvolutional networks," in *Proc. Computer Society Conference on Computer Vision and Pattern Recognition*, San Francisco, CA, USA, June 2010, pp. 2528–2535.

[99] Z. Wan and W. Liu, "Time-domain wideband doa estimation under the convolutional sparse coding framework," *IEEE Signal Processing Letters*, vol. 29, pp. 274–278, December 2021.

[100] R. Tibshirani, "Regression shrinkage and selection via the lasso: A retrospective," *Journal of the Royal Statistical Society*, vol. 73, pp. 273–282, June 2017.

[101] R. Chalasani, J. C. Principe, and N. Ramakrishnan, "A fast proximal method for convolutional sparse coding," in *Proc. International Joint Conference on Neural Networks*, Dallas, TX, USA, August 2013, pp. 1–5.

[102] B. Wohlberg, "Convolutional sparse representation of color images," in *Proc. Southwest Symposium on Image Analysis and Interpretation*, Santa Fe, NM, USA, March 2016, pp. 57–60.

[103] A. Koochakzadeh and P. Pal, "Cramér–Rao bounds for underdetermined source localization," *IEEE Signal Processing Letters*, vol. 23, no. 7, pp. 919–923, May 2016.

[104] P. Stoica and T. Marzetta, "Parameter estimation problems with singular information matrices," *IEEE Transactions on Signal Processing*, vol. 49, no. 1, pp. 87–90, January 2001.